THE SYNTHESIS AND CHARACTERISATION OF METAL OXIDE THIN FILMS

THIS THESIS IS SUBMITTED IN PARTIAL FULFILLMENT OF THE REQUIREMENTS FOR THE DEGREE OF DOCTOR OF ENGINEERING (CHEMISTRY).

DAVINDER S. BHACHU

2013

DECLARATION

I, Davinder Singh Bhachu, confirm that the work presented in this thesis is my own. Where information has been derived from other sources, I confirm that this has been indicated in the thesis.

ABSTRACT

This thesis details the use of chemical vapour deposition (CVD) to deposit transparent conducting oxide (TCO) thin films for potential use in a wide range of applications ranging from electrodes in photovoltaic devices to low-ε-coatings in architectural glazing. Transparent Conducting Oxide (TCO) materials exhibit optical transparency along with electrical conductivity. The nature of electrical conductivity arises from either excess electrons in the conduction band (n-type) or holes in the valence band (p-type). These materials underpin the photovoltaic industry by providing the transparent electrodes for thin film amorphous silicon solar cells, dye sensitised solar cells (DSSCs) and polymer based solar cells. The current industrial standard is tin-doped indium oxide but due to the cost of indium there has been a switch to alternative materials, mainly fluorine doped tin dioxide (FTO) and doped zinc oxide.

FTO thin films were deposited by use of an aerosol delivery system from methanolic solutions of monobutyltin trichloride. The deposition temperature was varied from 350-550 °C. The as-synthesised films displayed enhanced functional properties compared to commercial standards in terms of film microstructure i.e. pyramidal particle microstructure ideal for enhanced light scattering required for amorphous based silicon solar cells and also sheet resistances comparable to commercial standards.

The natural progression from tin dioxide films was to explore zinc oxide thin films with respect to their opto-electronic properties. Highly conductive and transparent ZnO films were synthesized by the reaction of diethyl zinc (in toluene) with methanol by dual source aerosol assisted chemical vapour deposition.

The scope of this thesis then moves away from TCO materials and concentrates on microporous oxide films produced by combining chemical vapour deposition (CVD) and hydrothermal methods. Dense, adhesive zeolitic films were synthesised from this method by using a CVD process to deposit a dense amorphous silica, titanium doped silica or iron doped silica films which were then converted to a crystalline nanoporous zeolite by a hydrothermal process using an organic structure directing agent. To demonstrate the capa-

bility of the method, silicalite-1 (S-1) and titanium silicalite-1 (TS-1) and iron silicalite-1 (Fe-Silicalite) zeolites were prepared. Both X-ray diffraction (XRD) and scanning electron microscopy (SEM) revealed the presence of crystalline zeolite films with well-defined morphology. Ti and Fe K-edge X-ray absorption spectroscopy (XAS) revealed the presence of the metal ions in the framework of the zeolitic matrix and in isolated, tetrahedral sites both in the amorphous and crystalline zeolite films. With respect to the TS-1 films synthesised, XAS revealed that both the pores and the titanium centres in the films were also shown to be accessible for molecules, by reacting with n-hexene and H_2O_2. In order to assess the generality of this method metal-organic framework (MOF) films of $[Zn_4O(bdc)_3]$ (MOF-5; bdc = 1,4-benzenedicarboxylate) were synthesised by reacting zinc oxide films, deposited by chemical vapour deposition (CVD), with terephthalic acid (H_2-bdc) and dimethylformamide (DMF) in a conventional solvothermal process.

PUBLICATIONS

1. Davinder S. Bhachu, Andrew J. Smith, Ivan P. Parkin and Gopinathan Sankar. Metal Organic Framework Films from Zinc Oxide: A Combined Chemical Vapour Deposition and Solvothermal Synthesis. Submitted to CVD, 2012.

2. Davinder S. Bhachu, Andrew J. Smith, Ivan P. Parkin, Andrew J. Dent and Gopinathan Sankar. Zeolite Films; A New Synthetic Approach. Journal of Materials Chemistry A, 2012.
DOI: 10.1039/c2ta00528j

3. Davinder S. Bhachu and Ivan P. Parkin. Aerosol Assisted Chemical Vapour Deposition of Transparent Conductive Zinc Oxide Films. Chemistry of Materials, 2012. DOI: 10.1021/cm302913b

4. Savio J. A. Moniz, Davinder S. Bhachu, Chris S. Blackman, Alison J. Cross, Sofia Elouali, David Pugh, Raul Quesada Cabrera and Stella Vallejos. A novel route to Pt-Bi_2O_3 composite thin films and their application in photo-reduction of water. Inorganica Chimica Acta, 380 (1), 328-335, 2012.

5. Davinder S. Bhachu, Mathew R. Waugh, Katharina Zeissler, Will R. Branford, Ivan P. Parkin. Textured Fluorine-Doped Tin Dioxide Films formed by Chemical Vapour Deposition. Chemistry - A European Journal, 17 (41), 11613–11621, 2011.

ACKNOWLEDGMENTS

Firstly I would like to thank my supervisor Professor Ivan P. Parkin for his constant support and guidance throughout my project. His desire to produce cutting edge science coupled with being an excellent supervisor and more importantly a friendly person.

I would also like to thank my secondary supervisor Dr Debbie Hammond and previously Dr Tim English for giving their time to expose me to science on an industrial level and their enthusiasm in the project. A special thank you to Professor Gopinathan Sankar for his help and support with certain aspects of my project and for teaching me not to throw away an X-ray amorphous sample as there is always a way to characterise it.

My special thanks goes out to Paolo Melgari for showing me the ropes and getting me started in the Parkin lab. I would also like to thank Dr Mathew Waugh, Dr Caroline Knapp, Dr Geoffrey Hyett, Dr Chris Blackman, Dr Sanjayan Sathasivam, Dr Savio Moniz, Dr Jeremy Cockcroft, Prof. Andrea Sella and Mr Martin Vickers for useful discussions and drinks. I would also like to thank the technical staff at UCL. In particular Mr Kevin Reeves and the guys at the workshop.

A big thank you to my family and friends. Starting with my mum and my brother; the guys at the weightlifting club; Adam O'Shea and James Partis; and Rosamund Kay I couldn't have done it without you.

CONTENTS

LIST OF FIGURES

LIST OF TABLES

ACRONYMS

CVD chemical vapour deposition

DSSCs dye sensitised solar cells

TCO Transparent Conducting Oxide

PV Photovoltaic

PVD Physical Vapour Deposition

HT Hydrothermal

ST Solvothermal

TEOS tetraethylorthosilicate

APCVD atmospheric pressure chemical vapour deposition

LPCVD low pressure chemical vapour deposition

CVS Chemical Vapour Synthesis

AACVD aerosol assisted chemical vapour deposition

ITO tin doped indium oxide

FTO fluorine doped tin dioxide

CBM conduction band minimum

VBM valence band maximum

AZO aluminium doped zinc oxide

BIPV building integrated photovoltaics

MO molecular orbital

AOs atomic orbitals

DOS density of states

BOB block of bands

MPP maximum power point

FF fill factor

CIGS copper indium gallium selenide

HOMO highest occupied molecular orbital

LUMO lowest unoccupied molecular orbital

SBUs secondary building units

XRD X-ray diffraction

SEM scanning electron microscopy

S-1 silicalite-1

TS-1 titanium silicalite-1

Fe-Silicalite iron silicalite-1

XAS X-ray absorption spectroscopy

MOF metal-organic framework

DMF dimethylformamide

FWHM full width half maximum

AFM Atomic force microscopy

XANES X-ray absorption near edge spectroscopy

EXAFS extended X-ray absorption fine structure

u-AACVD ultrasonic-AACVD

c-AACVD Collison-AACVD

MBTC mono-butyl tin chloride

TFA trifluoroacetic acid

IPA isopropyl alcohol

WDX wavelength dispersive X-ray analysis

ECCS electro-chrome coated steel

Chapter I

INTRODUCTION

1

INTRODUCTION

1.1 GENERAL INTRODUCTION AND AIMS

The general aim for the work presented in this thesis was to synthesize coatings by CVD on a variety of substates which could be used as working layers of in DSSCs. This work was mainly focused on TCO thin films. Doped tin dioxide and doped zinc oxide were the main systems explored. The work then looked at synthesising microporous oxide (zeolite/metal-organic framework) thin films using a combination of CVD and hydrothermal/solvothermal (Hydrothermal (HT)/Solvothermal (ST)) methods. Microporous oxide films could have a variety of applications in materials science ranging from electrically insulating coatings to catalytically active coatings.

The fabrication of TCOs and full characterisation of the optoelectronic and structural properties is vital in materials processing. TCOs are materials which combine optical transparency with electrical conductivity. In order for materials to be transparent they must display a band gap greater than the highest frequency of visible light (3.1 eV). Metals for instance are highly conductive but do not transmit visible light and transparent materials such as glasses are insulators. TCOs exhibit intrinsic conductivity due to defect states in the crystal structure. By extrinsic doping with aliovalent (where the ion that is substituting the host ion is of a different oxidation state) elements the conductivity of TCOs can be improved. The introduction of impurities into the crystal structure results in donor states near the conduction band for n-type semiconducors or or acceptor states near the valence band for p-type semiconductors. An important requirement in doping is that these states must be shallow in order to maintain optical transparency. These materials underpin the Photovoltaic (PV) industry by providing the transparent electrodes for thin film amorphous silicon solar cells, dye sensitized solar cells (DSSC) and flat panel displays in polymer light emitting devices.

TCO materials are generally limited to those that exhibit n-type conductivity such as In_2O_3, SnO_2 and ZnO although some p-type

materials are known such as $CuAlO_2$, $SrCu_2O_2$ and NiO. For practical applications in devices ranging from solar cell electrodes to light emitting diodes a TCO must have a resistivity of less than 10^{-3} Ω.cm and over 80% transmittance in the visible region. A key requirement for advances in TCO technology will be to reduce resistivity with no deleterious effects to the optical properties over the visible region. Low resistivity is achieved through very high levels of doping with concentrations in excess of 1×10^{20} cm^{-3}. This can then result in high free carrier absorption and high plasma resonance reflectivity, resulting in poor transmission. This may look bleak but there is the potential for improvements in electrical conduction while maintaining the optical transmission through increasing the carrier mobility. This will be achieved through improving the microstructure of the films, reducing defect concentration/improving charge carrier mobility and reducing impurity scattering centres. The materials challenge for increasing the TCO grain size, while reducing point defect concentration is complicated however by the need for high temperature for the former and low temperature deposition for the latter.

An additional major area for TCO performance improvement for PV applications is in interfacial properties. These physical (e.g. surface roughness/topography), optical (optical scatter) and electronic properties (losses at interfaces) at the TCO borders are critical for optimising performance. For example a controlled degree of scattering is essential for optimising efficiency and this level should vary with wavelength according to PV material employed.

Zeolites are the most important class of crystalline nanoporous solids with a plethora of applications including ion-exchange, gas separation/absorption and catalysis. These crystalline solids are widely used, predominantly in the form of powders, however, over the last twenty years zeolite membranes and films have been studied for applications in gas-separation, gas-sensing, low-$\varkappa$-dielectrics and as corrosion resistant materials. Although the preparation and applications of zeolite films have been reported as early as 1980s, several preparative methods of zeolite films has been developed over the last two decades with the aim to overcome production and mechanical issues, including adhesion and brittleness, which often limit their application as films. The current processes for the preparation of zeolite films are commonly limited to solution processing methods. These processes involve the use of an organic templating agent in a sol-

gel/hydrothermal process, similar to conventional methods to produce crystalline powder zeolites. Further improvements have been made by introducing secondary seeded growth methods to produce films with enhanced physical and mechanical properties. In general the solution processing method involves: formation of a colloidal suspension, followed by deposition on a support and the introduction of seeds. This process leads to mechanically weak films with high inter-particle porosity. To overcome some of these issues and more importantly to enhance the possibility of large-scale membrane and film production capabilities, a new strategy using a chemical vapour deposition (CVD) and hydrothermal (HT) approach was developed and reported here in this thesis.

This thesis has two main focal points: the formation of transparent conducting oxides and formation of microporous oxide films. These two components could be used together in order to create a DSSC PV device, where the zeolite layer acts as the insulating material on metallic substrates and the TCO layer acts as the PV electrode. This introductory chapter details the methods used for thin film synthesis, the theory that underpins TCOs, a brief introduction to photovoltaics devices and finally the fabrication of zeolite films using a combined CVD and HT approach.

1.2 THIN FILM DEPOSITION ROUTES

Thin film deposition has led to many different approaches to the required goal. The different techniques can be put into three distinct groups: wet chemical, Physical Vapour Deposition (PVD) and chemical vapour deposition (CVD). Each methodology has associated pros and cons and careful consideration of the resulting film properties such as crystallinity, microstructure and adhesion must be taken into account.

1.2.1 *Wet Chemical*

Wet chemical routes to thin films include chemical bath and Sol-gel methods which are wet chemical routes to thin films.[1–6] These usually involve the use of chemical precursors which react and form a colloidal solution which forms the basis of the network of the desired material. When the solution is left to age and the solvent is evaporated

a continuous solid network forms.[7–9] Initially this was realised from the hydrolysis of tetraethylorthosilicate (TEOS) in an acidic medium forming a colloidal solution and subsequent drying and aging results in a silica network. Thin films can be formed from these solutions in relatively simple ways. The two most common forms are:

- Dip coating: where a substrate is dipped into a precursor solution and the solvent is driven off by heating forming a solid film. As-deposited films tend to be X-ray amorphous and films usually require annealing to achieve crystallization.
- Spin-coating: the precursor solution is dropped/spread onto a spinning substrate which results in the precursor solution spreading out across the surface of the substrate but also removal of the solvent forming a dry solid layer.

1.2.2 *Physical Vapour Deposition*

PVD techniques inherently involve expensive high vacuum equipment as the the desired material is vaporised and then condenses onto a substrate.[10,11] PVD techniques encapsulate[12–14]:

- Evaporative deposition: The material is heated and condenses onto the substrate where it forms a solid layer.
- Electron beam vapour deposition: Electrons impinge on the desired material which results in vaporisation and film formation is achieved by condensation.
- Sputtering: A plasma is the form of energy used to vaporise the desired material.
- Pulsed laser deposition: A high energy laser pulse impinges on the material to achieve vaporisation.

1.2.3 *Chemical Vapour Deposition*

CVD involves the formation of a thin solid film on a substrate *via* chemical reactions of precursors in the vapour phase. It is the chemical reaction which distinguishes CVD from physical vapour deposition (PVD) processes.[1,2,15,16] The chemical reactions occur homogeneously in the gas phase and/or heterogeneously on the substrate.

The latter is desired in order to obtain high quality films.[4,5,17] CVD requires the delivery of a precursor into a gas stream, transport of the precursor to a substrate and the application of energy to cause a reaction. The key steps of CVD are shown in figure 1, which include:

1. Evaporation and transport of reagents in the bulk gas flow region into the reactor;
2. Mass transport of the reactants to the substrate surface;
3. Adsorption of the reactants on the substrate surface;
4. Surface diffusion to growth sites;
5. Nucleation and surface chemical reactions leading to film growth;
6. Desorption and mass transport of remaining fragments of the decomposition away from the reaction zone.

The film growth rate in thermal CVD is determined by the substrate temperature and the pressure of the reactor as well as the complex gas phase chemistry occurring in the reaction zone. At lower substrate temperatures the film growth rate is determined by the kinetics of the chemical reactions occurring either in the gas phase or on the substrate surface and is generally denoted as surface reaction limited film growth. As the temperature is increased, the film growth rate becomes almost independent of temperature and the growth is determined by the mass transport of the precursors through the boundary layer to the growth surface. This is known as mass transport limited film growth.

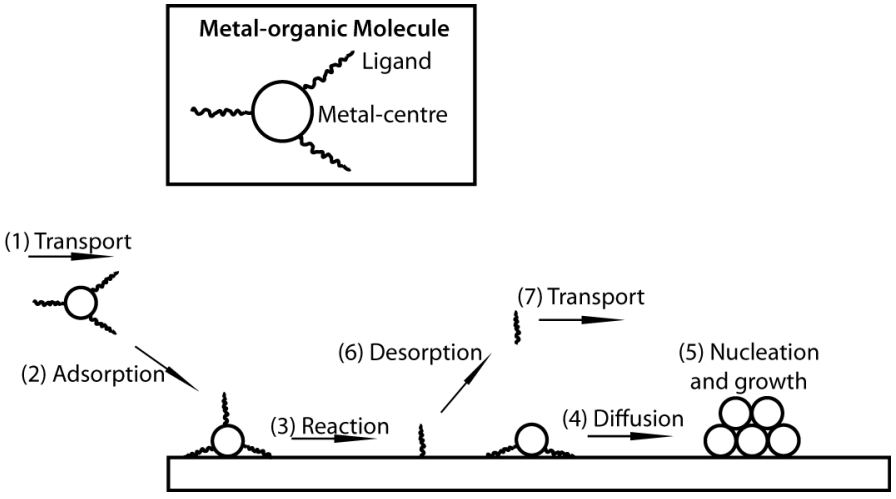

Figure 1: Schematic of the CVD process.

At higher temperatures, the growth rate decreases as the film precursors are desorbed from the film surface and/or depletion of reagents on the reactor walls due to gas-phase side reactions. These gas-phase side reactions become more important at high temperatures and higher partial pressures of the reactants.

There are a wide range of techniques that fall under the CVD category and ultimately differ in one parameter:

- Pressure. CVD can either be carried out at atmospheric pressure chemical vapour deposition (APCVD) or under low pressure chemical vapour deposition (LPCVD).[18–20]
- Precursor decomposition. The energy supplied to initiate the chemical reaction can be delivered in the form of heat, light, RF, plasma or another method.
- Number of precursors. The amount of precursors required for the deposition can either be from a single precursor (single source) which contains a preformed bond of the desired product, or multiple precursors (dual or multiple source) to form the bonds required in the desired film.
- Precursor transport. The precursor can be introduced into the gas phase via heating, liquid injection or through the formation of an aerosol.[21–27]
- Type of reactor. The reaction chamber can either hot walled, cold walled and have a horizontal, vertical or dynamic substrate.

The depositions in this thesis were carried out at atmospheric pressure, using a carbon block equipped with a cartridge heater onto which the substrates were placed with unheated walls (cold wall reactor). A vapour/aerosol was then delivered towards the substrate after going through a baffle to ensure laminar flow. In the case of a cold walled system, the substrate is directly heated which results in a temperature gradient across the substrate and influences the precursor behaviour which will be discussed later in this chapter. A hot walled reactor was also used in some depositions, where the entire reactor is heated leading to more uniform heating and a minimised temperature gradient in comparison to a cold wall system.

A large range of materials can be deposited using CVD and find applications in the following areas of technology:

- microelectronics
- optoelectronics
- protective and decorative coatings
- optical coatings

1.2.3.1 *Layer Morphology*

Layer morphology is crucial in determining the physical characteristics of a thin film. The layer morphology is determined by surface diffusion and nucleation during a deposition which are in turn affected by substrate temperatures, partial pressures of gaseous species and total pressure of the system. The three main types of layers formed by CVD are epitaxial, amorphous and polycrystalline. Epitaxial layers involve the growth of a defect-free single crystal film on a substrate of the same material (homoepitaxy) or on a different material (heteroepitaxy).[1,16] Epitaxial growth is normally carried out in clean-room conditions as it essential that the initial substrate is free from defects and surface contamination. Epitaxial growth is a difficult process and there should be no lattice mismatch between the crystalline spacings of the film and substrate. The growth of epitaxial layers usually occurs at high temperatures and ideally low growth rates such that surface diffusion is fast in relation to the arrival of new growth initiating species on the surface which allows adsorbed species to diffuse to low energy sites and form a layer which mimics the underlying substrate. Growth of amorphous layers however requires low temperatures, high growth rates and surface diffusion is slow relative to the incoming precursor flux. In between the two extremes exists the growth of polycrystalline layers. Polycrystalline layers are grown at intermediate temperatures, in between the two extremes, which results in nucleation at many different sites resulting in islands which coalesce to form a polycrystalline layer.[1,16]

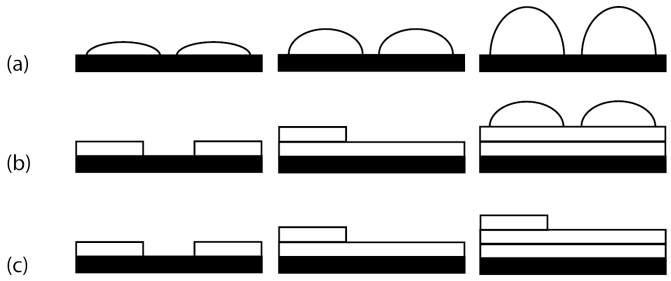

Figure 2: Crystal growth mechanisms: (a) 3-D island growth, Volmer-Webber growth; (b) layer-plus island growth, Stranski-Kastanov growth and (c) layer-by layer growth, Franck-van der Merwe growth.

The growth of films by CVD can be described by three growth models for thin film formation as shown in figure 2. Volmer-Webber type growth (figure 2(a)) involves the nucleation of small clusters at different sites on the substrate which then grow into islands, three-dimensionally and eventually coalesce to form a continuous film. This type of film growth usually occurs when the film atoms are more strongly bound to each other than the forming bonds with the substrate. Franck-van der Merwe (two-dimensional) (figure 2(c)) layer-by-layer growth occur when the film atoms have an affinity to bond to the substrate. Figure 2(b) shows Stranski-Krastanov growth, and this is a combination of layer-by-layer growth and island growth mechanisms. [1,16]

CVD layers have to adhere to the substrate to find any commercial application. The adhesion of layers is not fully understood, but it is thought that to promote good adhesion, the substrates require thorough cleaning before deposition. The rationale behind this school of thought is that impurities on the surface can physically hinder the deposition of a coating which can lead to a discontinuous, loosely bound layer, which can be rubbed off. However, even clean and impurity free surfaces do not result in film formation due to a lack of cohesive/adhesive bonds between the film and substrate.

Particles can also form in a CVD reaction via homogeneous gas phase reactions, although particle formation is generally undesirable in CVD processes and results in a loosely adhered films. Any particles that result in the reactor, serve to consume precursors, thus depleting the amount available for thin film formation. Particles are also potential sources of defects as they can "snow" down onto the thin film, resulting in pin-hole centers. These mainly arise when the

precursors are introduced into the reactor in the form of an aerosol (essentially suspended liquid particles).[1,16] The particles can form as a result of gas-phase reactions or as a result of solvent evaporation yielding solid particle precursor. When the particles form, they are subjected to a number of forces present within the reaction chamber. The most common force encountered is thermophoresis, described as the force acting on particles (also molecules) suspended in a fluid in the presence of a temperature gradient. This phenomenon results from the fact that gas molecules impinging on the particles from a region of higher temperature have a higher average velocity than those impinging on the particle from regions of lower temperature, for particles much smaller in dimension than the mean free path of the gas molecules.[4,17,22] This results in greater momentum transfer from gas molecules to the particle from those on the higher temperature side than those on the lower temperature side. For particles larger than the mean free path of gas molecules, thermophoresis has a greater affect and the success of thermal CVD processes can be attributed to thermophoresis, because in cold-walled CVD reactors, the large temperature gradient results in particles being moved away from the substrate towards the "cold" side of the reactor. Particle formation can also be desired, especially in the formation of powders and is usually termed Chemical Vapour Synthesis (CVS). These usually involve the introduction of liquid droplets into a cold-walled reactor which undergoes evaporation, decomposition and/or reaction in the gas phase forming powders. The depositions carried out in this report have been carried out at atmospheric pressure, using a heated substrate in a cold walled reactor. The precursors were delivered by heating via a bubbler and then transporting to the substrate in an inert gas flow as well as the formation of an aerosol, using dual source methods.[4,17,22]

1.2.3.2 *Fluid Dynamics*

The Knudsen number, Kn, is the ratio of the mean free path, λ, to the characteristic reactor dimension perpendicular to the flow direction, D (the diameter of the tube), which is a key parameter used to describe the CVD process. The mean free path is the average distance travelled by a vapour molecule between collisions with another molecule. We use $Kn = \lambda/D$ in order to determine the mass transport properties of the reactor. The gas flow characteristics change with

decreasing pressure from a viscous flow regime where intermolecular collisions dominate, through to a transition flow and finally to a molecular flow regime, where intermolecular collisions are rare. Kn < 0.01 indicates a viscous flow; 0.01 < Kn < 1 indicates transition flow; Kn > 1 indicates molecular flow. The Reynold's number, Re, is the ratio of forces often used to characterise a fluid flow through a pipe:

$$Re = \frac{U_\infty}{\nu} \tag{1}$$

The kinematic viscosity, ν, is the momentum diffusivity and is usually used to model the fluid dynamics. Kinematic viscosity increases with decreasing pressure. The bulk (mean) velocity, U_∞, is not measured but estimated. The characteristic length for a flow inside a tube, L, is usually the diameter of the tube.

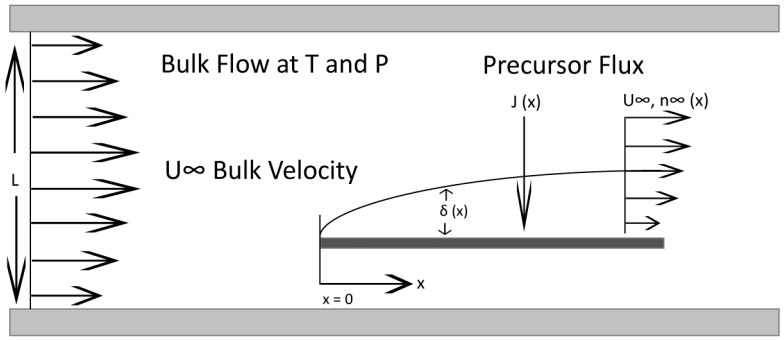

Figure 3: Schematic diagram of the laminar viscous flow through a tube reactor with a horizontal substrate, highlighting the dominance of boundary layers in the deposition model.

The characteristic length for bulk flow over a flat surface is the length of the surface in the flow direction, x as shown in figure 3. In CVD reactors, the Reynolds number is very low, below a few hundred, and the flow is laminar.[4,17,22] In a laminar flow regime the fluid flows in layers parallel to the direction of the flow. Flow towards the substrate (lateral motion) occurs via diffusion. The transition to turbulent flow is in the range of Re = 2100. Turbulent flow is undesirable in CVD because the growth rate needs to be controlled and a turbulent flow can 'trap' precursors causing a high local concentration resulting in homogeneous gas phase decomposition. The bulk flow contains a carrier gas and the reactant species. The reactant species are consumed at the surface of the substrate and therefore the gas

concentration at the surface is assumed to be zero. Mass diffusion of reactant gasses from the high concentration in the bulk flow to the area of zero concentration and generates a concentration boundary layer. Precursor molecules in the bulk flow diffuse to the heated substrate where they are adsorbed and consumed across a boundary layer. The uniformity of the deposition depends on the local diffusion flux to the surface and that flux depends on the local boundary layer thickness.[4,17,22] Figure 3 shows the velocity profile of a gas entering a heated reactor. The gas enters the reactor with a uniform velocity profile. The gas loses momentum however with increasing x, due to collisions with the walls of the reactor, resulting in the velocity of the gas to decrease. The velocity of the gas directly in contact with the walls is assumed to be zero, and is known as the static boundary layer. The velocity profile of the gas becomes more skewed and less uniform. The layers of gas directly above the static boundary layer are also slowed to a point in the reactor where there is no uniform portion of velocity. This is the region where full laminar flow has developed.

As mentioned above, the majority of the coatings mentioned in this thesis were synthesised via a cold-wall CVD reactor. Particle formation is generally undesirable in CVD processes and results in a loosely adhered films. Any particles that result in the reactor, serve to consume precursors, thus depleting the amount available for thin film formation. Particles can "snow" down onto the thin film resulting in pin-hole centers. These mainly arise when the precursors are introduced into the reactor in the form of an aerosol (essentially suspended liquid particles).[28] Particles can form as a result of gas-phase reactions or as a result of solvent evaporation yielding solid particle precursor. When the particles form, they are subjected to a number of forces present within the reaction chamber. The most common force encountered is thermophoresis, described as the force acting on particles (also molecules) suspended in a fluid in the presence of a temperature gradient.[28] This phenomenon results from the fact that gas molecules impinging on the particles from a region of higher temperature have a higher average velocity than those impinging on the particle from regions of lower temperature, for particles much smaller in dimension than the mean free path of the gas molecules.[4,17,22] This results in greater momentum transfer from gas molecules to the particle from those on the higher temperature side than those on the

lower temperature side. For particles larger than the mean free path of gas molecules, thermophoresis has a greater effect and the success of thermal CVD processes can be attributed to thermophoresis, because in cold-walled CVD reactors, the large temperature gradient results in particles being moved away from the substrate towards the "cold" side of the reactor.

Diffusion should also be considered, with respect to cold wall CVD reactors, in addition to thermophoretic forces experienced by particles in the reactor. The movement of particles within a fluid is described by Brownian motion, which is the random movement of particles by the bombardment of other molecules within the fluid. Particle diffusion increases with higher substrate temperatures and smaller particle sizes. Particles close to the substrate surface or walls of the reactor in a hot wall CVD reactor will also experience Van der Waals attraction between the particle and the surface as well as short range or long range attraction or repulsion depending on the charge of the particle and surface.[28] Attractive forces between particles results in a film with an aggregation of particles, whereas repulsive forces between particles results in a film with dispersed particles. With high film coverage however these two effects become negligible. Particles within the reactor are also subjected to gravitational forces. Gravitational settling is an important force acting on particles larger than 1 μm in diameter, but is less of a factor for particles smaller than this in comparison to the forces mentioned above and is very significant for aerosol particles in the reactor. The extent of the forces experienced within the reactor is highly dependent on the size of the particles introduced into the reactor. For nanoparticles in the reactor, diffusion > thermophoresis > gravitational settling. For micron sized particles however gravitational settling >> thermophoresis > diffusion.[28] Nanosized particles or droplets introduced in the reactor experience less thermophoresis than large particles as well as more diffusion towards the substrate surface compared to large particles. Diffusion however is a random process and particles can be directed to the substrate as well as away from it to the walls of the reactor and thermophoresis is a significant force acting on the particles. Whereas gravitational settling is the dominant factor for micron sized particles or droplets in the reactor.[28]

In the case of molecular precursors (APCVD) within the reactor the thermophoretic effect is small and gravitational settling is negligible.

Diffusion of the precursors towards the substrate is the main driving force for film growth.[28]

1.2.3.3 *Reaction Kinetics*

CVD is a kinetic process (i.e. non-equilibrium) that is controlled by the mass transport of precursors in the gas phase which react irreversibly on a surface as opposed to a system which reaches thermodynamic equilbrium over time. A conventional CVD system generally involves three steps: (1) introduction of the precursor, (2) transport of the precursor to the surface of the substrate and (3) surface reaction of the precursor. The slowest step in this series will be the rate limiting step of the overall process. Film growth rates in CVD are determined by the temperature of the substrate, pressure regime of the reactor and gas-phase composition.[16]

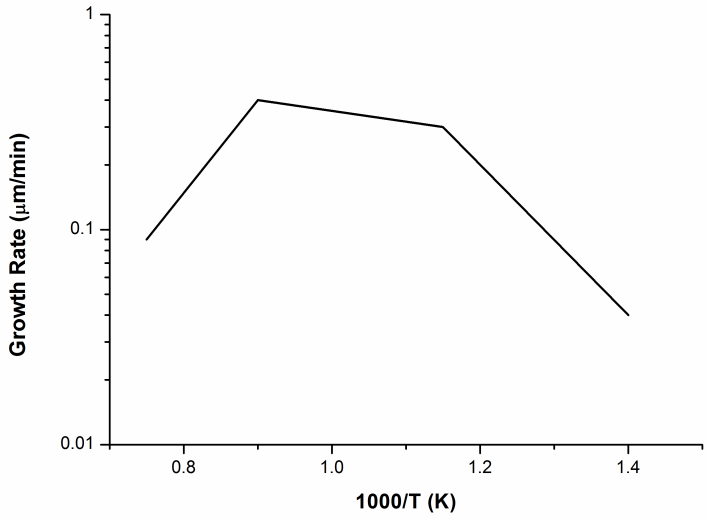

Figure 4: Typical growth rate of CVD film with reciprocal growth temperature.

Figure 4 shows the dependence on film growth on substrate temperature. It is clear from figure 4 that three growth modes are apparent with respect to substrate temperature. At low substrate temperatures, the growth rate is limited by chemical kinetics and increases expo-

nentially with temperature, which can be described by the Arrhenius expression:

$$GR = Aexp(E_A/RT) \tag{2}$$

where GR is the film growth rate, $E_A$is the activation energy, R is the gas constant and T is the temperature. As the temperature increased, there is a region where film growth rate is almost independent of temperature, i.e. mass transport of the precursors controls the film growth rate. This type of growth is advantageous in cold-wall CVD systems, where there is difficulty in achieving uniform substrate heating. Reactant flux to the surface is proportional to the concentration of the limiting precursor, which allows for simple control of the magnitude of the growth rate. If the temperature is increased further, then the film growth rate decreases due to increased desorption rate and depletion of reactants on the walls of the reactor. Higher substrate temperatures may also encourage gas phase reactions, resulting in particle formation instead of film formation.[1,16]

If a CVD process is mass transport limited, then a typical rate limiting step can be the diffusion of the precursor molecules through the boundary layer. The rate of diffusion across a concentration gradient is given by Fick's Law of diffusion:

$$J_A = -D\frac{dC_A}{dx} \tag{3}$$

where $J_A$is the precursor flux of species A, D is the diffusivity constant, $C_A$is the concentration of species A and x is the direction perpendicular to the substrate surface (there exists a concentration boundary layer). The concentration gradient can be approximated as:

$$\frac{dC_A}{dx} \approx \frac{\triangle\, C_A}{\triangle\, x} = \frac{C_{A_S} - C_{A_B}}{\delta} \tag{4}$$

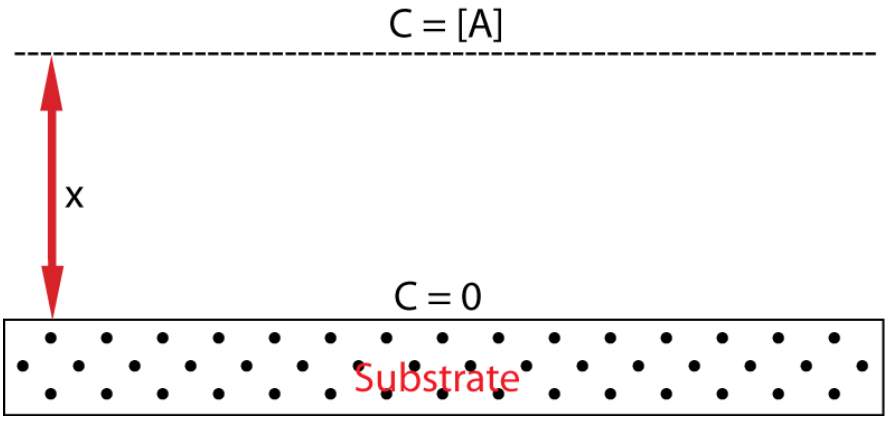

Figure 5: Precursor concentration boundary layer in mass transport limited regime.

where C_{A_B} is the precursor concentration of species A in the bulk flow above and C_{A_s} is the precursor concentration of species A at the surface. Figure 5 shows the situation for mass transport controlled film growth. Therefore equation 4 reduces to:

$$\frac{dC_A}{dx} \approx \frac{\triangle\, C_A}{\triangle\, x} = \frac{C_{A_S}}{\delta} = -\frac{[A]}{\delta} \tag{5}$$

substituting in 3 gives:

$$J_A = \frac{D}{\delta}[A] \tag{6}$$

which is a first order rate equation with respect to [A] and the rate constant is the temperature dependent diffusion constant at reference conditions divided by the thickness of the concentration boundary layer. The rate of diffusion of precursor to the surface is expressed in molecules/cm²s.

1.2.3.4 *APCVD*

APCVD is the most conventional form of CVD where metal-organic precursors are heated within a bubber and then delivered to the reaction chamber by an inert carrier gas. The rate at which the precursor is supplied to the reaction chamber is determined by the temperature at which the bubbler is held (vapour pressure of the precursor) and the rate at which the inert carrier gas is fed into the precursor bubbler, noting that the overall pressure in the system is atmospheric. The re-

quirement for precursors for APCVD is that they have a relatively high vapour pressure such that the liquid to vapour phase change is fairly easily established.

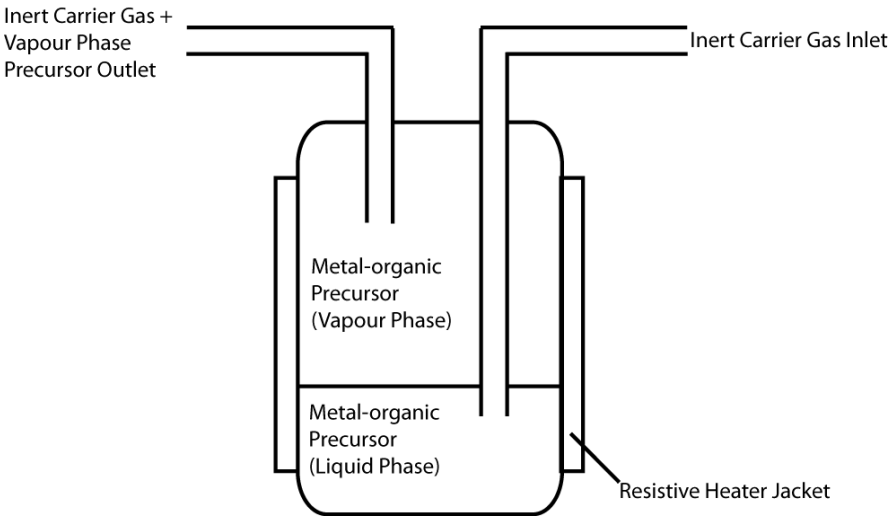

Figure 6: Schematic of bubbler used to generate vapour of metal-organic precursor and transport of precursor *via* an inert carrier gas during APCVD.

A thermodynamic equilibrium can be established assuming ideal mixing of the gases in the bubbler resulting in:

$$\frac{N_p}{N_c} = \frac{P_p}{P_c} \tag{7}$$

Where N_p and N_c are the number of moles of the metal-organic precursor and carrier gas respectively and $P_p$and P_c are the partial pressures of the metal-organic precursor and carrier gas respectively. Assuming the system only contains precursor and carrier gas species then:

$$P_c = (P_{total} - P_p) \tag{8}$$

As the system is operating under ambient pressure (i.e. atmospheric) then we can substitute 760 torr for P_{total} and substituting equation 8 in 7 results in:

$$N_p = \frac{N_c \times P_p}{(760 - P_p)} \tag{9}$$

1 mole of gas at room temperature and pressure occupies 24.4 litres and diving N_c by the molar gas volume allows for the use of flow rates of carrier gas (F_c in l/min) to calculate the flow rate of of precursor species (F_p) in moles/min. Equation 9 therefore transforms to:

$$F_p = \frac{F_c \times P_p}{24.4(760 - P_p)} \tag{10}$$

in order to calculate the molar flow rate of the precursor species based on the vapour pressure and carrier gas flow rate.[1,16]

1.2.3.5 *Aerosol Assisted CVD*

As mentioned earlier, variants to the conventional CVD process exist in terms of the energy supplied to break down reactive precursors, but also in terms of how the precursors are delivered. Conventionally, precursors in the CVD process are delivered by heating within a bubbler to generate a vapour which is then transported to the reaction chamber. A key requirement for this type of CVD technology requires the precursors to have a substantial vapour pressure and the experimental set-up to have heated lines in order to inhibit precursor condensation.[4,17,22]

Variants of the conventional precursor delivery system exist in form of an aerosol of precursors which is known as aerosol assisted chemical vapour deposition (AACVD). The aerosol is generated by nebulising the precursor solution using an ultrasonic generator, electrostatic aerosol generator or high pressure gas stream to generate an aerosol. The precursors are usually mixed in a solvent, nebulised and then delivered to the reaction chamber, where the solvent is evaporated/combusted and the chemical precursors undergo decomposition/chemical reaction ideally on the surface on the substrate. The advantages of AACVD compared to conventional CVD processes is that it negates the need for heated reactor lines, is relatively low cost compared to conventional CVD processes as it can be performed under ambient pressure and does not require complicated vacuum systems. AACVD does require either liquid precursors/readily soluble precursors.[4,17,22]

The droplet size depends greatly on the method used to generate the aerosol. The most common method for aerosol generation is via an ultrasonic device, in which a piezoelectric transducer is placed underneath the liquid precursor solution, which creates standing waves

on the surface of the liquid. The aerosol properties depend on the physical properties of the precursor and solvent as well as the intensity and frequency of the ultrasonic device.[22,29] The aerosol droplet diameter is given by Lang's equation:

$$d = 0.34[2\pi\sigma/\rho f^2]^{1/3} \tag{11}$$

where f is the frequency of the ultrasonic device, ρ and σ are the density and surface tension respectively. The ultrasonic method can produce an aerosol with a narrow droplet size distribution which can lead to better aerosol uniformity and coating quality.

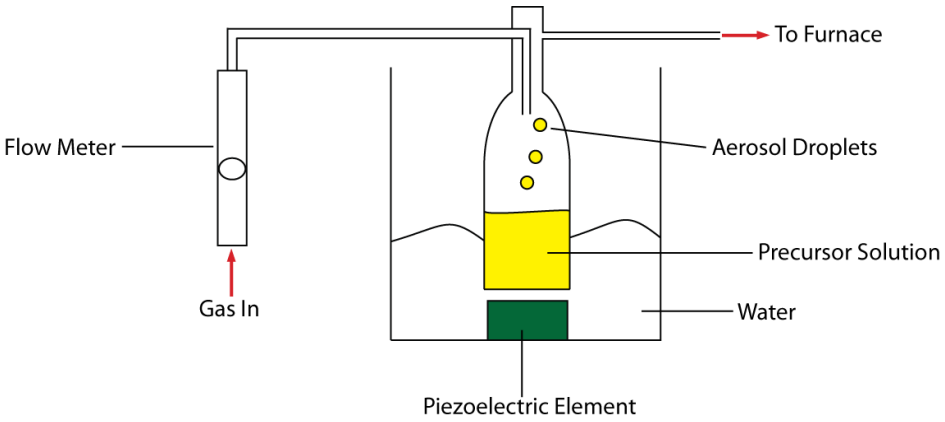

Figure 7: Generation of aerosol droplets via submerged ultrasonic transducer.

An alternative method for aerosol generation is the use of a pressure atomizer. Pressure atomizers work by discharging a liquid through a small orifice under high pressure. A variation of this type of design is the Collison type atomizer. The Collison type atomizer draws a liquid stream into a high velocity gas which atomizes the liquid.[17,22] The droplets formed in this type of atomizer are directed towards a surface, where the smaller aerosol droplets make a sharp bend and are directed towards the reactor, whereas larger aerosol droplets impact on the walls of the atomizer because of their greater inertia. This narrows the aerosol size distribution and the average aerosol droplet size. and produces sub-micron droplets.

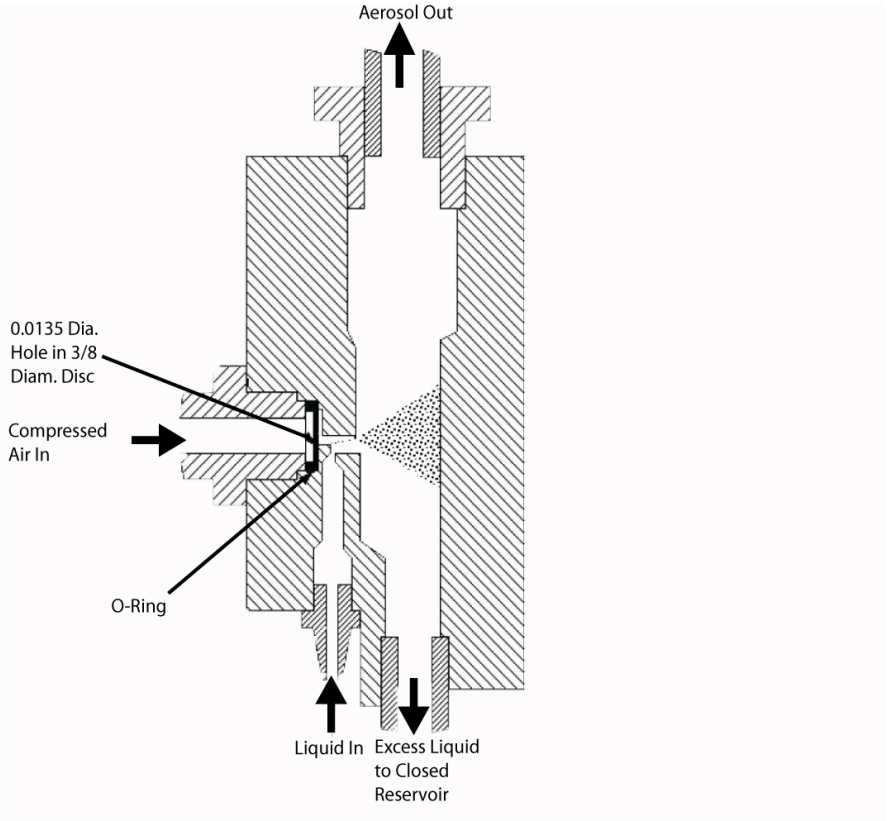

Figure 8: Collison-type aerosol generation to produce sub-micron sized droplets.

As the name suggests AACVD relies on the formation of a vapour to form a film. Somewhat confusingly AACVD and spray pyrolysis are used interchangeably In comparison to conventional CVD, AACVD has not been modelled mathematically. The processes that occur as the droplets enter the reaction chamber have been discussed qualitatively however. The simplest case for AACVD is where the solvent evaporates as the droplet enters the reactor and the precursor molecules also enter the gas phase and film formation occurs on the surface of the substrate. The next scenario is where incomplete solvent evaporation occurs and the precursors do not fully enter the gas phase, resulting in a mixture of gas phase and liquid phase precursors. The final scenario is where complete evaporation of the aerosol droplet occurs and particles are formed within the gas phase as shown in figure 9.

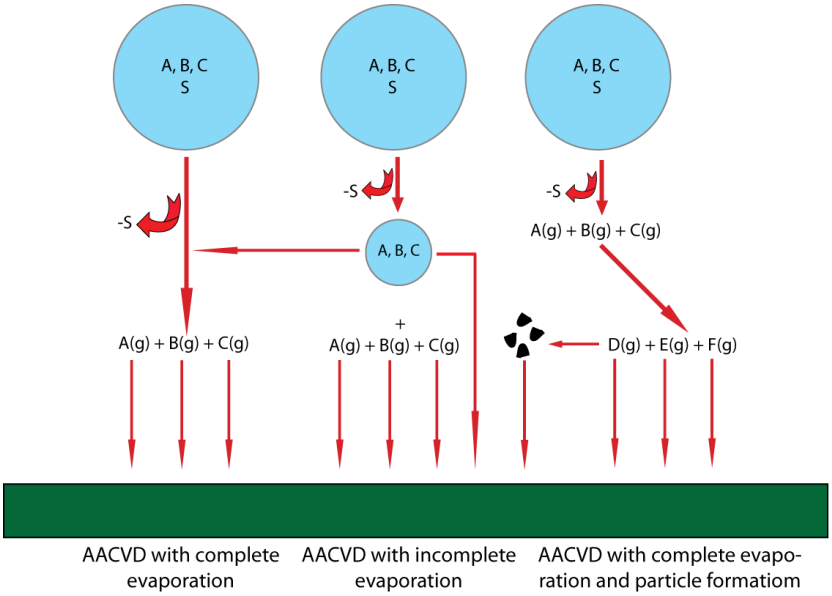

Figure 9: Possible aerosol droplet reaction mechanisms in CVD reactor, where A, B and C are precursors and S is the solvent.

Precursor decomposition in AACVD is not trivial however and several complications arise due to differences between precursor decomposition rates, precursor vapour pressure and gas phase reaction rates. To add to this, particles can also react with gas phase species such as radicals and can also react with the solvent forming adducts. Particles formed within a reactor can also deposit via thermophoresis, sedimentation, impaction, diffusion, interception and electrophoresis. This in most cases leads to poor film properties and is generally undesirable, but can be beneficial if metal/metal oxide composite films are required.

1.3 TRANSPARENT CONDUCTING OXIDES (TCOS)

Energy use, storage and conservation is a major societal concern. New methods and devices that can capture and utilise sunlight as well as coatings that reduce energy losses from buildings have been developed and rapidly commercialised. Transparent conducting oxides (TCOs) play a pivotal role in both energy capture and conservation. These materials combine high optical transparency coupled with electrical conductivity. For a material to exhibit this property it must not absorb light between 380 nm (3.26 eV) to 780 nm (1.59 eV) i.e. must have an optical bandgap > 3.2 eV. Materials which combine high electrical conductivity with optical transparency already form the basis of

many important technologies including flat panel displays, solar energy capture and other opto-electronic devices.[30,31] A number of TCO materials are known, such as In_2O_3, SnO_2, CdO, $CdIn_2O_4$ and ZnO. These all exhibit n-type conductivity and although p-type TCO materials are known their properties remain inferior to TCO's of n-type character.[32–35] The source of the n-type conductivity in tin doped indium oxide (ITO) and FTO is related to the presence of shallow donor states located close to the conduction band, brought about by chemical doping.[36–38] The excess or donor electron undergoes thermal ionization at room temperature into the host conduction band. Upon further doping, a degenerate gas of current carrying electrons ensue, giving rise to high electrical conductivity and far infra-red absorption (Drude-like) but essentially leaving the conduction band intact i.e. the material remains optically transparent in the visisble region.[39,40]

The conduction band minimum (CBM) for most metal oxides is composed of the spatially spread spherical metal s orbital and form a wide band in which the electrons are delocalised resulting in smaller effective masses of the electrons compared to narrow bands. This can lead to high electrical conductivity if high donor doping numbers are achieved. The valence band maximum however is composed of oxygen 2p orbitals, which are not easily oxidized. The dispersion of the valence bands is small rendering hole doping difficult. As a consequence of this p-type TCO's were not discovered until 1997 compared to the first n-type TCO discovered in 1954.[41] There has been some progress in p-type TCO materials based upon $Cu^+(3d^{10})$ as the Cu 3d energy level lies just above the valence band maximum (VBM) and can result in more covalent VBM to make hole doping easier.[30,31,42]

The optical properties of TCO materials are set at short wavelengths by its band gap and at longer wavelengths by its plasma edge, which lies in the near infrared provided that the free electron density, n, does not exceed $2 \times 10^{21} cm^{-3}$. Research interests have mainly focused on the oxides of tin, zinc and indium as well as ternary compounds. A current trend has been to investigate aluminium doped zinc oxide (AZO) and also gallium indium oxide as potential alternatives to ITO and FTO. The main body of work has been looking at FTO coatings on glass and steel. It was discovered quite some time ago that simple binary oxides such as indium oxide and tin oxide could exhibit high conductivity whilst maintaining optical transparency.[43] By doping these simple binary oxides with aliovalent elements the con-

ductivity could be further enhanced.[41,44–47] Tin doped indium oxide (ITO), fluorine doped tin oxide (FTO) and aluminium doped zinc oxide (AZO) have shown to be the best performers as TCOs in terms of chemical stability, resistance to temperature and high conductivity, and have been used in the photovoltaic (PV) industry and in low-ε-window glazing.[33,48–51]

Most applications require a balance between optical and electrical properties of the layer which are linked by the Drude model and relate to the film thickness, carrier concentration and mobility of the layer. Carrier concentration can be tuned by the amount of dopant delivered during the reacion as well as any additives such as alcohols or water which can affect the kinetics of the reaction and the microstructure of the resulting film.[52–54] TCO materials for thin film solar cell applications are required to achieve a low electrical sheet resistance (< 10 Ω/sq). They should also include surface texturing to allow for light scattering and reduction of reflection losses which equate to a pyramidal microstructure and a film haze value of 8-15%. The emerging PV market currently is that of the photo-electrochemical cell, most notably dye-sensitized solar cells (DSSCs).[55–58] DSSCs provide a technically and economically viable alternative to solid state devices. In solid state PV systems, it is the role of the semiconductor to absorb incident light as well as act as the charge transporting medium. With DSSCs these two functions are separated and incident light is absorbed by a dye molecule anchored to the surface of a wide band-gap semiconductor material and charge separation occurs at the interface of the excited dye molecule and conduction band of the semiconductor material.[56,59,60] PV to date has been dominated by solid-state devices, usually made of silicon, but as the cost of these devices is high, there is increasing pressure to move away from these types of device. DSSCs are also cheap per unit area compared to solid-state devices. This is an attractive business opportunity for steel and glass companies to incorporate DSSC technology into steel/glass sheets in order to produce building integrated photovoltaics (BIPV).

1.3.1 *Band Structure of Solids*

Band theory is based on the valence electrons and that the core-electrons are localised and the contribution of core electrons can be largely ignored. The symmetry of the overlap between neighbouring

orbitals is described by the wave vector k, which must satisfy the Blöch relationship, such that the allowed electronic wavefunctions within the solid are corresponding to periodic arrangements of the atomic orbitals in the whole structure.[61] These wavefunctions then provide stationary solutions to the Schrödinger equation with periodic boundary conditions applied for an electron and thus result in no scattering of the electron in the crystal when the Bloch relationship is satisfied. Scattering mechanisms are caused by defects, phonons, the interaction with other electrons within the crystal and boundaries.[62,63] The available energy levels for electrons in the case of free atoms is discrete, in the form of atomic orbitals. In the case of solids however, the available energy states for electrons form bands. In metals, which conduct electricity, the Fermi level cuts through a partially filled band, thus allowing for a portion of electrons to move unoccupiued states as shown in figure 10(a). As the momentum of the electrons is changed, conduction of electricity occurs through the solid, and a net drift velocity can only occur if there are empty states within the band. For this reason solids with full bands do not conduct electricity for small applied fields, but can conduct electricity at higher temperatures as electrons can be excited into conducting states above the band gap.[61] In insulating solids, the electrons are delocalized on the valence band and are separated by a large gap from the conduction band, this is known as the band gap as shown in figure 10(b).

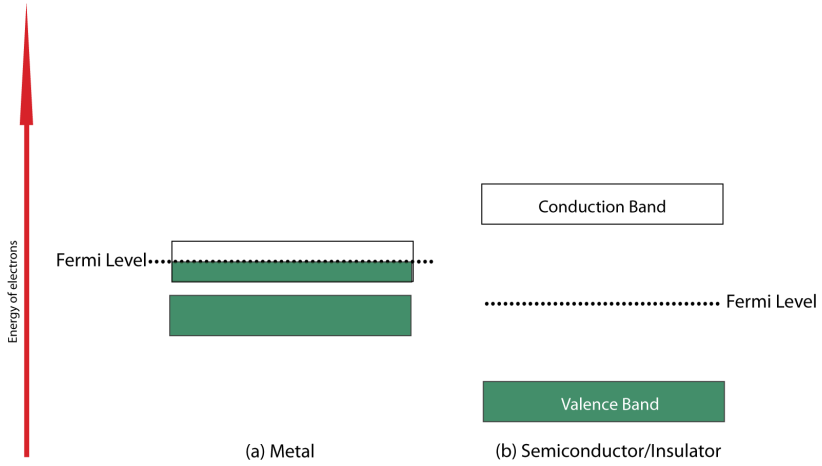

Figure 10: Energy bands for solids

The distinction between semiconductors and insulators depends on the magnitude of the band gap. The band gap is larger for insulators

compared to semiconductors. The Fermi level (E_F) is indicated in figure 10 and this is an important parameter in band theory. The Fermi function ($F(E) = \{1 + exp(\frac{E-E_F}{kT})\}^{-1}$) gives the probability (at thermodynamic equilibrium) of an electron occupying a state at a given energy, E. If the electron energy is equal to the Fermi energy, then the probability that the state is occupied is equal to 1/2. The Fermi position in semiconductors lies within the band gap.

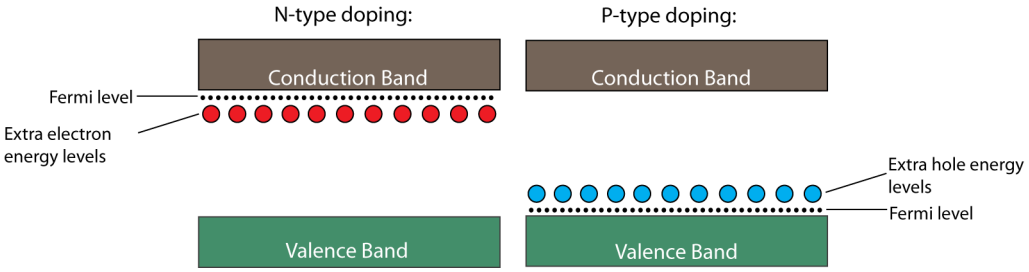

Figure 11: Doping in semiconductors

The position of the Fermi level can be altered by the addition of dopants, which can generate electrons or holes, known as n-type and p-type semiconductors respectively. If a material is doped with impurities which serve to increase the number of electrons within the semiconductor material then the the Fermi level is raised near the top of the band gap, such that extra electrons can easily be excited into the conduction band. If a material is doped with impurities which serve to increase the number of holes (acceptors) just above the valence band, this shifts the Fermi level down to just above the valence band.

The band structure can be thought of as analogous to a molecular orbital (MO). The band structure is crucial to the understanding a wide range of properties of a solid ranging from electronic conductivity, optical properties, magnetism and catalytic activity. The band structure can be represented by what is essentially a MO diagram with translational symmetry taken into account. The plot is E(k) vs. k, where k is the wave vector that describes the phase of the atomic orbitals (AOs) as well as the wavelength of the electron wavefunction (crystal momentum). There are as many lines in the band structure diagram as there are orbitals in the unit cell. Wide bands indicate that there is a large intermolecular overlap and that there is a large degree of electron delocalization. Narrow bands however indicate that there is weak intermolecular overlap and that the electrons are localized. Keeping the chemical perspective clear here, a solid or surface is just

a very large molecule. Taking a single unit cell with n molecular orbitals and then repeating the unit cell over space in three dimensions to yield a macroscopic crystal yields N number of unit cells (where N is close to Avogadro's number) then there are Nn crystal levels. In a discrete single molecule a single orbital or a small subgroup of orbitals can be singled out as being the valence orbitals of the molecule and in determining the geometry and reactivity of the molecule.[39,40,61,64–66] This is not the case for a crystal in that a single level is responsible for directing geometry and reactivity amid the Nn number of oribitals within the crystal. Instead of locating a single level, a bunch of levels however can be located in a similar way to a single level for a discrete molecule. This is done by looking at all the levels in a given energy interval. If the band structure is integrated, then the density of states (DOS) results which shows the number of available levels between E and E + dE. The density of states can be approximated by taking the raw components from the MO diagram. TiO_2 is a semiconductor with a wide range of uses and the rutile structure of TiO_2 also serves as a fairly straightforward example, where TiO_6 octahedra run in one direction in the crystal to form an infinite assembly with no monomer units. There are however identifiable octahedral sites and at each octahedral site, the metal d block can be split into the conventional t_{2g} and e_g type splitting.[40,61]

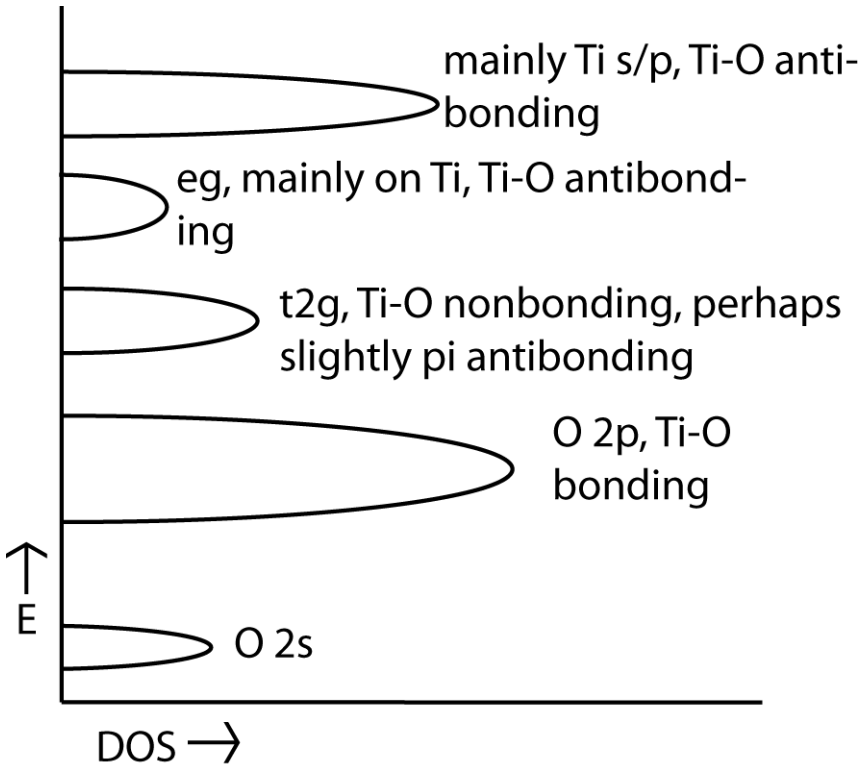

Figure 12: Predicted DOS diagram for rutile TiO_2 based on the MO approach of edge sharing TiO_6 edge-sharing octahedra.

The energy levels of each block of bands (BOB) in the DOS diagrams comes from the MO diagram, based on the interaction of the metal centre with the ligands (electronegativity and bonding interactions). The area of the BOB is proportional to the number of MO's at that approximate energy. The width of each BOB is derived from the overlap between building blocks.

1.3.2 *Electrical Conductivity*

Band theory provides the model upon which phenomena such as electrical conductivity can be explained. The conduction of electricity is well described for metals and it is the drift movement of electrons in response to an electric field. The electric field exerts a force on each electron which then accelerate in a direction defined by the electric field, i.e. its momentum changes. In the absence of an external electric field, the electron gas in a semiconductor is in a state of equilibrium because of the interaction of electrons with lattice defects, such as lattice imperfections, thermal vibrations of the lattice (phonons) and impurity atoms. A simple model, known as the Drude[40,61,67,68] model

of conduction for metals, can be used to describe electron conduction within solids. This model assumes that:

- Each electron is thought of as a solid sphere.
- The metal is formed from a mass of positively charged ions for which there is a corresponding number of delocalised free electrons.
- In the absence of an electric field, the electrons move in a random straight line until a collision with a positive ion. (Electron/electron interactions and electron/defect and impurity interactions are ignored.
- The collisions are instantaneous and change the velocity of the electron.
- The frequency of a collision can be described by a mean free path (the average distance an electron travels before a collision).
- The electrons are modelled as having a kinetic energy of 3/2 kT ($\frac{1}{2}mv_{th}^2 = \frac{3}{2}kT$).

The applied magnetic field can be represented as E = U/L where U is the potential difference applied between the length L of a solid. E is present at each point in the solid which results in acceleration (a) of the electrons in the solid.[39,40,64]

$$a = E(e/m) \tag{12}$$

where, e is the charge on an electron and m is the mass of an electron. As every electron in the solid has thermal velocity in every direction which cancels out to zero, they also have an induced acceleration in the direction of the applied field which is lost after collision with the lattice. A constant electric field will cause the electrons to have an additional velocity given by the drift velocity (v_d) due to the applied electric field:

$$v_d = (\frac{eE}{m})\tau \tag{13}$$

where τ is the relaxation time, which is the average time between scattering events. The root mean square velocity, v_m which Drude

assumed to be due to thermal distribution at temperature T, is larger than the drift velocity (i.e. $v_m >> v_d$) and as such Ohm's Law is not violated. Once an average thermal speed v_m and a relaxation time have been established, a mean free path is gven by:

$$l = v_m \tau \tag{14}$$

And is defined as the average distance travelled by an electron between collisions. With regards to dc conductivity, Ohm's Law can be written independently of shape and length as:

$$J = \sigma E \tag{15}$$

This is a version of Ohm's Law taking out geometric consideration of the experiment, where J is the current density, σ is the electrical conductivity and E is the applied electric field. As mentioned the random movement of electrons in all directions results in the vector sum of the velocities to equal zero.[40,63] As there is an additional drift velocity however, due to the external field, the charge that flows is:

$$J = N_e e v_d \tag{16}$$

Substituting the expression for v_d into 16 results in the linear relation for J and E:

$$J = \frac{N_e e^2 E \tau}{m} \tag{17}$$

This also yields the expression for conductivity, σ:

$$\sigma = (N_e e)(\tau \frac{e}{m}) \tag{18}$$

where the mobility of the electron is given by:

$$\mu_e = \tau \frac{e}{m} \tag{19}$$

Current flow is a very small perturbation on the electrons normal behaviour as given by the difference in drift and root mean square velocities and metallic conduction is well described by Ohm's Law in that metals have many low mobility charge carriers in the form of electrons to provide conduction, but this relationship can break down with semiconductor materials in which there are few charge carriers with high mobilities resulting in a large drift velocity term. Equation 18 describes conductivity in an ideal solid and one in which the collision experienced by the charge carrier are only between the lattice and other scattering pathways and quantum mechanical phenomena are not accounted for. In order to account for these forces, the mass of the electron should be replaced with the effective mass, m_e, which can approximate forces hindering the electron mobility such as electron/electron interaction, defects, surfaces and impurities such as dopants. The simplicity of the Drude model allows for us to determine that in order for high conductivity in a transparent conducting oxide for example a large charge carrier density coupled with high charge carrier mobility is required. The Drude model however is a simple model based on the kinetic theory of gases extended to free electrons in a solid, which copes well with DC and AC conductivity in metals and also showing experimental relationships such as Ohm's Law. The Drude model however underestimates the velocities of the electrons as well as overestimates the electronic heat capacity.

Conductivity measurements for semiconductor materials are fairly straightforward, provided that the contact between the probe and material is ohmic and not too low ($< 100\,\Omega$), a two-point probe technique should suffice and reflect the true resistance of the sample. This technique involves pressing two Cd-plated contact probes of a multimeter onto opposite ends of a sample and measure the current passing through the sample on applying a known voltage.[64] This method however does not yield accurate results since the contact resistance for most semiconductors to Cd is high. The Fermi level in semiconductor or metal is essentially a measure of the chemical potential of the electrons. If two conductors are placed in electrical contact with each other, charge flows from one to the other until the Fermi levels equilibrate. The charge flow results in a potential difference between the two conducting materials which is known as the contact potential. For a metal/metal contact, the contact potential is located at the point of contact and there is little hindrance to electron tunneling. For

a semiconductor/metal junction, the small number of carriers in the semiconductor material inhibits the development of a large potential gradient due to the charge and potential relationship. As the semiconductor and metal are placed in contact, the electrons flow from the surface of the region of the semiconductor and into the metal which gives rise to a depleted region. The electrons in the conduction band of the semiconductor have to tunnel through this depletion zone to complete the circuit and a large contact resistance may develop as a result. This problem can be avoided if the metallic contact of the probe is considered carefully and results in a junction which is ohmic/non-depleted contact with the semiconductor. A metal with a low work-function is ideally required for the measurement of resistivity of n-type semiconductors. An alternative to the inaccurate two point-probe method is the four probe method. Current is injected into the sample at point I and ejected at point IV in the sample and the potential drop between these points, at II and III, is measured using a high impedance voltmeter and this negates the use for non-ohmic contacts but better results are obtained with ohmic contacts.[64]

The electrical conductivity for thin films is greatly influenced by the thickness of the films. The conduction path for thin films is affected by the surface if they are less than a few hundred nanometres by interrupting carrier transit along their mean free path. The charge carriers can be diffusely scattered in which they emerge from the surface, or specularly reflected resulting in their velocity component perpendicular to the surface being reversed, their energy remaining constant. The conductivity of the films will be affected if the charge carriers are diffusely scattered. Small crystallite size, lattice impurities and the large number of structural defects in the film also affect the overall conductivity.[63,64]

The reciprocal of the electrical conductivity is known as the electrical resistivity ρ. For a rectangular sample, the resistance R is given by[63]:

$$R = \rho(l/bt) \tag{20}$$

where l is the length, b is the width and t is the thickness of the sample. If l = b then:

$$R = \rho/t = R_s \tag{21}$$

R_s is the sheet resistance and is defined as the resistance of one square of film and is independent of the size of the square. The quantity is expressed in Ω/sq. The method used for measuring this quantity is a four point probe technique. When the probes are placed on the sample the resistivity is given by:

$$\rho = \frac{V}{I}\frac{2\pi}{1/d_1 + 1/d_2 - 1/(d_1+d_2) - 1/(d_2+d_3)} \tag{22}$$

where $d_1 = d_2 = d_3 = d$ and is the distance between the probes, then:

$$\rho = \frac{V}{I}2\pi d \tag{23}$$

If the sample is in the form of a thin film with the thickness of the coating less than the spacing of the probes, this reduces to:

$$\rho = \frac{V}{I}\frac{\pi t}{ln2} \tag{24}$$

$$\frac{\rho}{t} = R_s = 4.53\frac{V}{I} \tag{25}$$

An alternative arangement to the simple four probe technique is the van der Pauw[69] configuration:

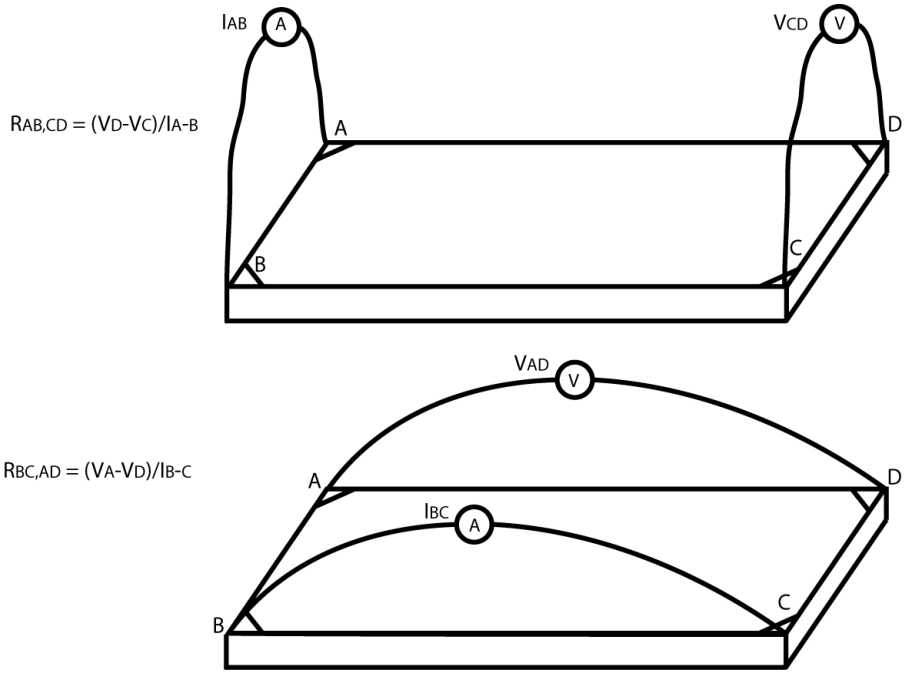

Figure 13: van der Pauw configuration for measuring conductivity of a thin film sample.

The van der Pauw configuration allows for the electrical resistance of a sample of uniform thickness but arbitrary shape to be measured, by placing four probes (A, B, C, D) on the edges of the sample.

$$R_{AB,CD} = \frac{V_D - V_C}{I_{A-B}} \tag{26}$$

$$R_{BC,DA} = \frac{V_A - V_D}{I_{B-C}} \tag{27}$$

where V_D-$V_C$is the potential difference between probes D and C resulting from the injection of current I from probes A to B and follows the same form for the reciprocal configuration which results in:

$$exp(-\pi R_{AB,CD} d\sigma) + exp(-\pi R_{BC,DA} d\sigma) = 1 \tag{28}$$

The equation can then be solved for the conductivity, σ:

$$\sigma = \frac{log_e 2}{\pi d}(\frac{2}{R_{AB,CD} + R_{BC,DA}})f(r) \tag{29}$$

where f(r) depends on the ratio $r = R_{AD,CD}/R_{BC,DA}$. If $R_{AD,CD}$ and $R_{BC,DA}$ are equal within 1%, then f(r) is taken as 1 within 0.001 % and can be ignored.[35,69,70]

This four probe configuration is useful as it is the one used to measure the Hall effect which gives information about the nature of the charge carriers in the semiconductor material, i.e. whether the sample is n-type or p-type. The conductivity measurements alone do not yield this information. To distinguish between the charge carriers (electrons or holes) a Hall effect study can be carried out. Far-infrared (Terahertz) spectroscopy could also be used in order to determine the transport properties of the films. It also determines the density of charge carriers. The Hall effect occurs when a current is passed through a sample in the presence of a transverse magnetic field and a small potential difference, the Hall voltage, is developed between two opposite faces of the sample, in a direction perpendicular to both the current and applied magnetic field. The Hall effect also allows for the charge carrier density and mobility to be determined accurately. The Hall effect is observed due to the Lorentz force which is a combination of the electric and magnetic force.[64] As the electron moves along the electric field, perpendicular to the applied magnetic field, it experiences a magnetic force normal to both directions. The direction of the force experienced can be predicted using the "right hand rule". As a constant current is injected into the sample in the resence of a magnetic field perpendicular to this, the electrons (charge carriers in n-type semiconductors) which are subjected to the Lorentz force drift away from the current direction, which results in excess negative surface electrical charge and a potential drop across the two sides of the sample, known as the Hall voltage, as can be seen from figure 14. V_H is the Hall voltage, B is the applied magnetic field and I is the applied current through the sample. R_H is the Hall coefficient and is related to the carrier density by the following relationship:

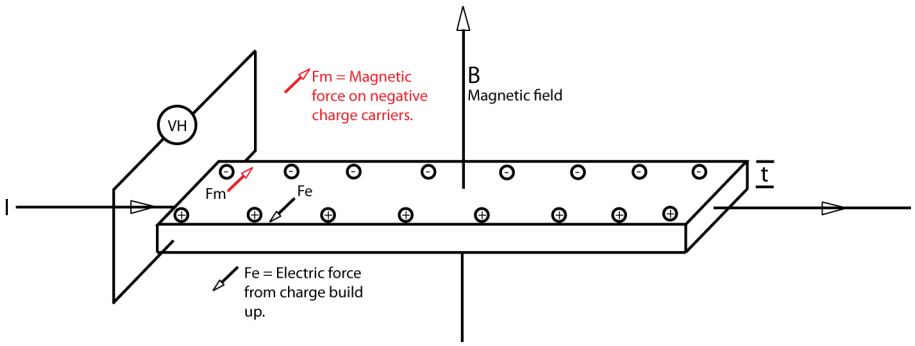

Figure 14: Experimental set-up for Hall effect measurements.

$$V_H = R_H I(B/t) \tag{30}$$

$$R_H = (1/Ne) \tag{31}$$

For single crystalline films, the conductivity is governed by various scattering methods such as lattice scattering, acoustic deformation potential scattering, piezoelectric scattering, optical phonon scattering and neutral/ionized impurity scattering. In polycrystalline thin films however, grain boundary scattering is another important mechanism.

1.3.3 *Optical Properties of TCOs*

The optical properties of TCO thin films depends greatly on the deposition technique, microstructure and defect structure of the material. TCO materials in general are electrically conductive and optically transparent to visible and near-infrared light and reflective to thermal infrared radiation. For long wavelengths, TCO materials are reflective due to free electrons in the conduction band and for very low wavelengths, absorption is observed due to the band gap of the material.[35,67–71]

In the infrared range, the optical properties for TCO materials can be described by Drude's theory for free electrons in metals described previously. Light impinging on a TCO semiconductor leads to polarisation of the material due to the interaction of the free electrons in the TCO material with the electromagnetic field of the light. The electrical properties of the TCO materials, such as the charge carrier

mobility and the charge carrier density of the thin film will determine when the material will display a reflection to longer wavelengths of light, beginning somewhere in the IR. This characteristic absorption is known as the plasma frequency, caused by the free electron plasma in the TCO semiconducting material. The onset of this plasma edge is exploited in insulating glazing materials.[63,67,68,71]

The Drude theory of conduction in metals can be used to explain this phenomenon. As mentioned previously, light impinging on a TCO semiconductor leads to polarisation of the material due to the interaction of the free electrons in the TCO material and as a result influences the relative permitivitty, ε. The Drude model assumes:

- electrons as a gas of free particles
- the crystal causes the electron mass, m, to be replaced with an effective mass, m*, which also provides evidence about the scattering mechanisms within the crystal.
- the mean scattering time is independent of the frequency of light.
- the restoring force, k_f, is modelled using a harmonic oscillator approximation.

Light hitting a TCO material with energy greater than the band gap results in absorption of a photon in a band transition. TCOs are transparent at wavelengths corresponding to visible light, but the transparency drops at wavelengths corresponding to the IR region (> 1500 nm). The transition from a transparent material to a reflective material corresponds to a maximum in absorption and is referred to as the plasma wavelength, where the frequency of the light corresponds to the frequency of the collective oscillation of the electrons in the material.[72] When the electrons oscillate in phase with the electric field component of light, absorption occurs.[72] At frequencies above the plasma frequency, the inertial mass of the charge carriers for such a rapid acceleration inhibits motion and the electrons cannot respond fast enough to screen the electric field of the incoming light, resulting in transmission of light. When light at a frequency lower than the plasma frequency impinges on the sample the electrons within the material respond quickly enough to screen the electric field component of light resulting in reflection of light.[73] The plasma frequency can

be modelled by assuming the charge carriers as displaced an average distance x, which induces polarisation, P:

$$P = N_e e x \tag{32}$$

where N_e is the free carrier density, e is the charge on the free carrier and x is the average displacement. The induced field by the polarisation acts as a negative restoring force to the charge carrier. The force is given by the field multiplied by the charge of the carrier:

$$\frac{-P}{\varepsilon} e = \frac{m d^2 x}{dt^2} = \frac{-N_e e x}{\varepsilon} . e \tag{33}$$

This equation is in the form of a harmonic oscillator and solving for the average displacement:

$$x = A exp\{(\frac{N_e e^2}{m_e \varepsilon})t\} = A.exp.i(\omega_p^2 t) \tag{34}$$

and

$$\omega_p = (\frac{N_e e^2}{m_e \varepsilon})^{1/2} \tag{35}$$

The Drude model showed that conductivity is:

$$\sigma = (N_e e)(\tau \frac{e}{m_e}) \tag{36}$$

where the effective mass of an electron is now used to accommodate any retarding forces acting upon the charge carrier and therefore:

$$\omega_p^2 = \frac{\sigma}{\varepsilon \tau} = (\frac{N_e e^2}{m_e \varepsilon}) \tag{37}$$

These equations relate the electrical properties of the material, such as N and μ to the optical constants n and k. The effect of the charge carrier density, N, is two fold in that N determines the plasma wavelength as determined by the relationship given above. As the the carrier concentration increases, the plasma wavelength will be reduced to the

visible. N also governs the maximum achievable reflectivity in the IR region. The effect of mobility on the IR reflectivity of TCOs is similar, however the plasma wavelength is not directly influenced by the change in the value of mobility.

1.3.4 *Applications of TCOs*

TCO materials find applications in areas ranging from heat mirrors in architectural glazing, conducting screens in touch displays, photocatalytic and gas sensing materials to forming the electrodes in photovoltaic devices.[21,25,29,63,74–78]

The two main applications of the TCOs presented in this thesis have been limited to heat mirror glazing and PV electrodes.

1.3.4.1 *Heat Mirror Glazing*

The interaction of light with free charge carriers in TCO materials has been discussed in the previous section. In the UV region it has been shown that TCO materials show an absorption edge due to the promotion of charge carriers from the valence band to the conduction band. As the frequency of light impinging on the TCO material is increased, reflection of light is observed above a critical wavelength (the plasma frequency). This frequency is directly related to the number of charge carriers within the semiconducting material and indirectly related to the mobility of the charge carriers. A quirk of TCO materials is the maintenance of optical transparency whilst exhibiting a reflection of light in the IR regime, whereas for metals this transparency is obviously not observed in the visible. As a result, careful tuning of the materials crystal structure, with respect to charge carrier number and mobility at the synthesis stage can result in control of thermal IR radiation across a coated glass substrate.

Double and triple glazing can significantly reduce heat loss through conduction and convection. By applying a TCO coating in addition to double/triple glazing, allows for a significant reduction in radiative heat loss from a room in cold climates. The near IR portion of the sun's energy is allowed to enter the room, whereas re-radiated longer wavelength radiation is reflected back into the building.

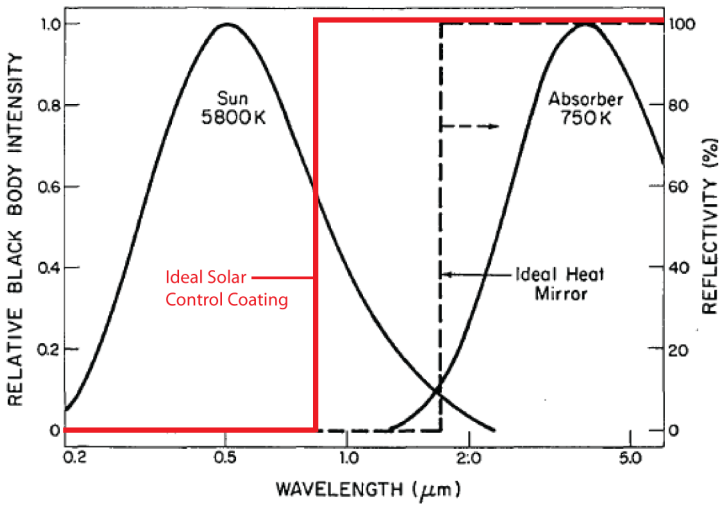

Figure 15: Solar spectrum showing irradiance at the earth's surface and typical blackbody radiation together with typical solar control and low emissivity coating spectra.[63]

As can be seen from figure 15 about half of the energy hitting the earth's surface occurs in the near IR region of the solar spectrum from 0.8 μm to 2.5 μm. The near IR region of the sun is responsible for heating. The radiation is absorbed and re-radiated as blackbody radiation from 3 to 50 μm. Blackbody radiation is essentially radiation that is emitted from any hot object, which includes people in buildings and radiators. Figure 15 also shows typical transmittance spectra for two types of coatings applied to windows depending on the climate. The first coating is known as a solar control coating, as shown by the red line, which is usually a thin film of sputtered metal. In the visible regime, it can be seen that the transmittance is high, primarily due to film being thin enough that appreciable levels of reflection cannot occur at the permitivitty values of visible light. As the wavelength increases however towards the near IR, the permitivitty decreases such that larger levels of reflection occur, allowing for near IR heat energy from the sun being reflected away, rather than entering the building. This type of coating is typically used in 'hot climates'.[25,78]

The second type of coating widely used in the glazing industry is known as a low-emissivity coating, represented by the dashed line in figure 15. Low-emissivity coatings are typically applied to glazing for use in 'colder climates' as this type of coating allows for visible light and near IR heat energy through the window, but reflects blackbody radiation so that more heat is retained within the building. Low-

emissivity coatings are carefully related to the electrical properties of the semiconducting material chosen, namely the charge carrier density and the mobility of the charge carriers, which relates to a critical resonance frequency, known as the plasma frequency at which the light is reflected. This frequency approximately begins at around 2 μm and extends out to longer wavelengths (i.e. the blackbody).[42,74,79]

Heat losses through windows is essential in determning the energy balance of buildings, even when double glazing is used. In keeping with increasing demand for lower energy consumption there is scope for improvement upon double glazing by introducing such solar control/low-emissivity coatings as an added barrier to heat loss within buildings. In fact, European legislation now requires that all new windows in 'cold' climates have TCO low- emissivity, which can potentially reduce energy losses from buildings by 15%.

The materials research challenge lies in optimising the microstructural properties of TCO materials and more importantly the electronic properties of TCO materials to tune the plasma reflection in the correct part of the electromagnetic spectrum for the desired application.

1.3.4.2 *TCO Electrodes for Solar Cell Applications*

TCO materials play an integral part of the photovoltaic industry as they serve as the transparent electrode for thin film solar cells such as amorphous silicon solar cells, dye sensistised solar cells (DSSCs) and organic based photovoltaic devices.[55–58] TCO materials are particularly useful in that they are transparent to visible light and TCO layers are easily fabricated on a large scale via online processes. There are certain requirements however when choosing a TCO to serve as the electrode for a photovoltaic device. Matching photovoltaic performance to the TCO is vital and it should be noted that:

- as the TCO layer thickness increases the short circuit current decreases;
- the open circuit voltage varies linearly with the electron affinity of the TCO;
- the charge carrier density of the TCO decreases the short circuit current in the PV device; and
- band gap matching of the TCO with the solar spectrum can result in high conversion efficiencies.

In addition to the requirements mentioned above the TCO layer must have high durability, high adhesion and show resilience to high processing temperatures often required for thin film solar cell fabrication.[80] Another important criterion for TCOs to serve as electrodes in PV devices is that the refractive index of the TCO material has to be chosen such that reflective losses of incident light are minimised and light trapping using scattering centres at the film interface are maximised. In order to achieve the latter, a pyramidal microstructure of the crystallites is ideal for TCO layers serving as PV electrodes, which often equates to a haze value of around 8-15%.

1.3.5 *Tin Dioxide*

Transparent conducting oxide materials underpin the PV industry by providing the transparent electrodes for thin film amorphous silicon solar cells, dye sensitized solar cells (DSSCs) and polymer based solar cells as well as in polymer light emitting devices.[60,81–83] The commercial demand for TCO materials has led to a large body of research into optimising the properties required for the given application as well as reducing the production cost.[42,48,84–88] Due to the increasing scarcity of indium along with the low resistance of ITO to high temperatures the cost benefits and properties of FTO as an alternative TCO are becoming evident. However, optimisation of the optical and electronic properties of TCO for the required application are a key commercial challenge and CVD could potentially be used to tailor the films for the desired application.[85,89,90]

Tin dioxide (SnO_2) is a wide bandgap semiconductor, with a theoretically calculated value at 3.6 eV. Tin oxide has a tetragonal rutile structure with space group D^{14} ($P4_2/mnm$).[63] The unit cells consists of two tin atoms and four oxygen atoms. Each tin atom is surrounded by six oxygen atoms, roughly arranged in a regular octahedron and each oxygen atom is engulfed by three tin atoms, approximately forming an equilateral triangle. The lattice parameters are $a = b = 4.737$ Å and $c = 3.185$ Å. The ionic radii for O^{2-} and Sn^{4+} are 1.40 and 0.71 Å respectively.

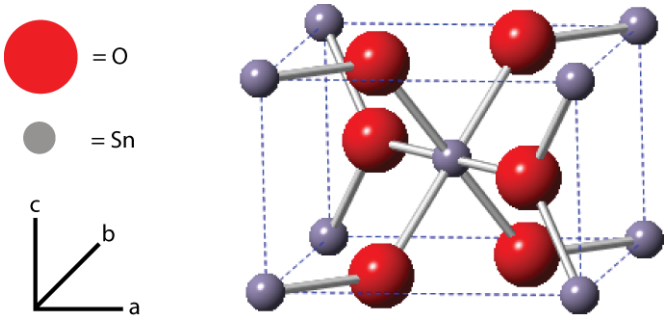

Figure 16: Unit cell of the crystal structure of SnO_2.

Stoichiometric tin dioxide is an insulator, due to the large band gap, however the electrical conductivity can be greatly improved by the addition of oxygen vacancies (non-stoichiometric tin dioxide films) as well as the addition of dopant impurities such as antimony and fluorine. Oxygen vacancies in tin oxide thin films results in n-type character due to the generation of electrons via the following process $O_O^x \longleftrightarrow V_O^{\bullet\bullet} + \frac{1}{2}O_2 + 2e^-$ [84,91–93], where oxygen on an oxygen site is removed, resulting in a vacancy on an oxygen site with a doubly positive charge on the framework, represented by two dots and the liberation of oxygen gas plus electrons as described by Kröger-Vink notation. This has been the proposed mechanism for the inherent n-type conductivity without dopant addition, but has been challenged recently by computational studies indicating that oxygen vacancies are very deep donors and that advantageous impurities such as hydrogen could be the source of the conductivity. Substitutional doping of Sn^{4+}cations with Sb^{5+}cations results in the generation of free electrons into the conduction band, such as $Sn_{1-x}^{4+}Sb_x^{5+}O_2^{2-} + xe^-$ whereas fluorine anions replace oxygen anions in the tin oxide lattice resulting in $Sn^{4+}O_{2-x}^{2-}X^- + xe^-$ where X represents fluorine or any other halogen dopant.[94] The electrical properties of FTO have been investigated by many researchers. The sheet resistance R_s decreases as the F/Sn atomic ratio in the solution increases, reaching a minimum. As the ratio increases the sheet resistance increases. These boundaries act as carrier traps for the free electrons from the bulk of the grain and results in a space charge region in the grain boundary. As a direct consequence of this phenomenon, a potential barrier to charge transport results. The type of scatteringis related to the concentration of free carriers in FTO thin films. FTO films with a carrier concentration of 10^{18} cm^{-3} conduction is governed by the grain boundaries, whereas films with a carrier concentration between 10^{18} and 10^{19} cm^{-3} conduc-

tion is governed by both bulk and grain boundary properties. If the carrier concentration is greater than 10^{19} cm^{-3} conduction is solely governed by the bulk.[30,42,89,95]

1.3.6 *Zinc Oxide*

Zinc oxide in its mineral form is known as zincite. Zinc oxide crystallises in the hexagonal wurtzite (B 4-type) lattice. The zinc atoms are almost in the hexagonal close packed position. The oxygen atoms lie within a tetrahedral cluster of four zinc atoms. These tetrahedra point in the same direction along the hexagonal axis, which give the crystal its polar symmetry. The unit cell constants are $a = b = 3.24$ Å and $c = 5.19$ Å.

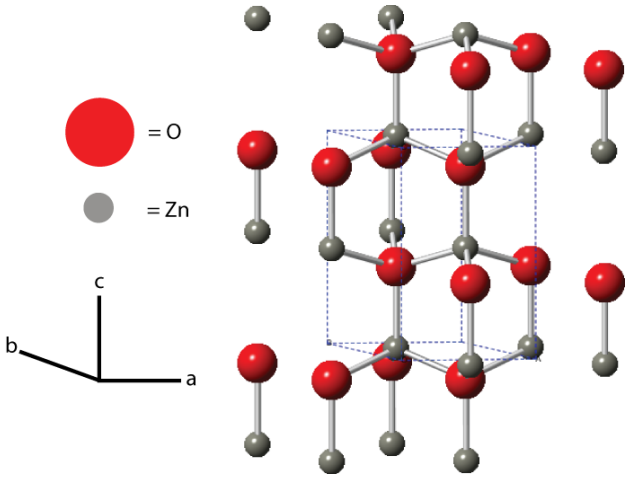

Figure 17: Wurtzite lattice of zinc oxide.

The band structure for ZnO has been calculated by many groups.[34,96,97] The calculated band structure for zinc oxide shows the valence band states consist of two low energy O:2s core-like states and with increasing energy the next six valence band states correspond to O:2p bonding states. The conduction band states are mainly metallic in character, localised on Zn and correspond to unoccupied Zn:3s levels. The conduction band states at higher energy can be described as fairly free-electron in nature.[32,34] Experimental and computational results show that the fundamental band gap for zinc oxide is 3.5 eV.[13,27,98] The current industrial standard for TCOs is tin doped indium oxide (ITO). Due to the scarcity and cost of indium alternatives need to be found. Fluorine doped tin oxide (FTO) is emerging as a replacement to ITO with electrical properties approaching that of ITO with

high transmittance. Zinc oxide films have received much attention to replace ITO as the industrial standard. With consideration of the environment, ZnO is a promising alternative because zinc is relatively inexpensive, abundant, relatively non-toxic and can exhibit electrical properties comparable to ITO.

1.4 PHOTOVOLTAIC CELLS

There is an increasing demand to move away from fossil fuels, like coal, natural gas and oil to provide power for society as this fossil fuel reserve is essentially finite. It has been estimated that there is only a few hundred years of this supply of fossil fuels remaining given the current rate of consumption, which is increasing due to developing nations also competing for their share of the global economy.[80,99] Increasing carbon dioxide concentration in the atmosphere is a sensitive topic but anthropgenic carbon dioxide concentrations have increased. It has been predicted by the United Nations Intergovernmental Panel on Climate Change that global warming over the next 50 years could have serious effects on sea levels, farming, immigration and economic development. There has been an increasing global effort to diversify the current energy portfolio. One way of achieving the move from fossil fuels is to embrace the use of renewable and alternative energy directly to produce fuels and electricity. Converting solar energy for example at 10% efficiency using only 1% of the Earth's land area could potentially meet the worlds energy demands twice over. There has been an intense amount of research over the past several decades to stand up to the materials challenge posed by solar technology and to advance solar technology beyond the realms of nature. One of the most popular technologies uses photovoltaic (PV) solar cells, which convert incoming solar radiation into electrical energy. Solar cell technology is generally thought of being born in the 20th century, but in actual fact dates back to the late 19th century and its birth can be traced back to the principles of photography. It was discovered, around 1839 by Becquerel and others that silver chloride (and other silver halides) resopnd to light.[100] A "wet photoelectrochemical" cell was first developed using copper oxide or silver halide coated metal electrodes immersed in an electrolyte solution and upon irradiation of one electrode resulted in the production of a small voltage. Solar cells as we know them however, are not wet photoelectrochemical

cells but are solid state semiconductor junction devices, first developed in 1954 at Bell Labs.[101–105] For any renewable/alternative energy source reliability, silence, long lifetime, low maintenance, flexibility and low pollution are key requirements for which solar cells meet. Solar energy in general can help give people more control over their own energy supply which therefore allows people to be less dependent on a centralised source of power. There are however drawbacks with PV systems, such as the initial start up cost being more expensive than traditional sources of electricity, but there are government subsidies and incentives in place to reduce costs.[60,80,100,102,105]

1.4.1 *Basic Photovoltaic Cell Operation*

Photovoltaic cells essentially work by utilising the photovoltaic effect. This is where incident sunlight is directly converted into electricity by a p-n (or p-i-n) semiconductor junction device.[103] This phenomenon although being known for almost a century, only advanced in 1954, with the production of a 6% crystalline silicon solar cell by Chapin *et al*.[101] This technology is used for a range of applications, such as supplying power for consumer products e.g. electronic calculators and garden lights. The p-n junction essentially arises when a p-type semiconductor material is brought into contact with a n-type semiconductor material meet. A p-type material for example is silicon/germanium doped with boron (group 13 element). Boron has three valence electrons compared to four valence electrons of silicon. When the dopant is introduced into the silicon crystal lattice, it bonds with the surrounding silicon. One bond however is incomplete due to the position of a missing electron i.e. the hole, which behaves like a positive charge as it can attract an electron from a nearby silicon atom and thus in the process forming another hole. Hence the majority charge carriers causing conduction are positive holes. In an n-type material the majority charge carriers causing conduction are electrons and result from doping silicon with a group 15 element, antimony for example. By "joining" together these types of materials in order to form a p-n junction, the Fermi levels (the average energy of the electron) of each type of material become equal and as a direct consequence of this results in a band bending region. In this junction electrons from the n-type material diffuse into the p-type region, whereas holes diffuse into the n-type region. This leaves the p-side

negatively charged and the n-side positively charged and hence an electric field is established and no mobile carriers exist in this region known as the depletion layer.

The electric field essentially restricts the movement of electrons from the n to p and not the other way around, i.e. acts as a diode. When photons of incident light are absorbed close to or at the p-n junction, providing the energy, given by $E_\lambda = hc/\lambda$, is greater than or equal to the band gap of the semiconductor material, then electron/-hole pairs are created. Electrons are simply excited from the valence band into the conduction band. As a result of this phenomenon, excess electrons accumulate in the conduction band of the p-side and excess holes accumulate in the valence band of the n-side. The electrons on the p-side "roll down the hill" whereas the holes on the n-side "bubble up" and are swept across the junction respectively because of the free energy gradient and not the potential energy of the inbuilt electric field.

As a result of this there will be a potential difference (open circuit voltage), due to the charge separation and if the device is not connected to an external circuit there will also be a current through the diode because of shortage/recombination. By constructing circuit diagrams in which to model a photovoltaic cell some important terms can be discussed.[102]

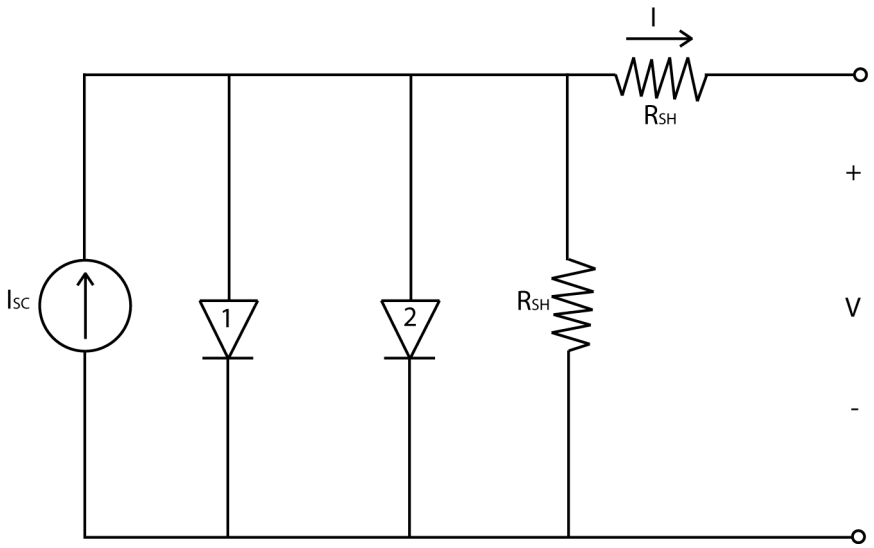

Figure 18: Simple circuit model of a PV cell. Diode 1 represents the recombination in the regions either side of the depletion region (quasi-neutral) and diode 2 represents the recombination in the depletion region.

By considering a photovoltaic cell as a current source, in which the incident number of photons with sufficient energy is directly proportional to the number of electrons generated then we can call this the photocurrent, I_{PH} or I_{SC}. In the circuit above, the ideal current source is connected so that it serves to forward bias the diodes, essentially having current coming out and going into the current source at the same time. So as we have a complete circuit and an external load, the voltage due to charge separation will reduce but there will remain a current through diode 1 and can therefore write an expression for the current flowing through diode 1, not taking into account diode 2. The expression for the diode current is given by the diode equation[102]:

$$I_D = I_0 exp(qV_D/nkT)–1 \tag{38}$$

where I_D = Diode current, I_o = Reverse saturation current, V_D = voltage across the diode (V + $I_L R_S$), q = Electron charge, k = Boltzmann constant, T = Absolute temperature and n = ideality factor of diode. So the current will also flow to the load and on doing so it will encounter a resistance on flowing through the bulk material as well as the resistance encountered by the metal contacts, in series with the load, represented as R_S. Also in the circuit model the shunt resistance, R_{SH}, represents the electron-hole pairs that recombine before being transferred to the load and hence it is represented in parallel to the load. The current through the shunt resistor is given by Ohm's Law, where $I_{SH} = V_D/R_{SH}$. With all these terms we can represent the load current, I_L simply as:

$$I_L = I_{PH} - I_D - I_{SH} \tag{39}$$

Substituting the expression for the diode current results in:

$$I_L = I_{PH}–I_0 exp(qV_D/nkT)–1–V_D/R_{SH} \tag{40}$$

As V_D is equal to V + $I_L R_S$ then the expression above reduces to:

$$I_L = I_{PH} - I_0 exp(q(V_L + I_L R_S)/nkT)–1 - V + I_L R_S/R_{SH} \tag{41}$$

This is the general expression for the current produced by a photovoltaic cell. By solving the equation and obtaining values for I_L at any given voltage, using the Newton Raphson method, results in a current-voltage curve characteristic to photovoltaic cells.[102,103]

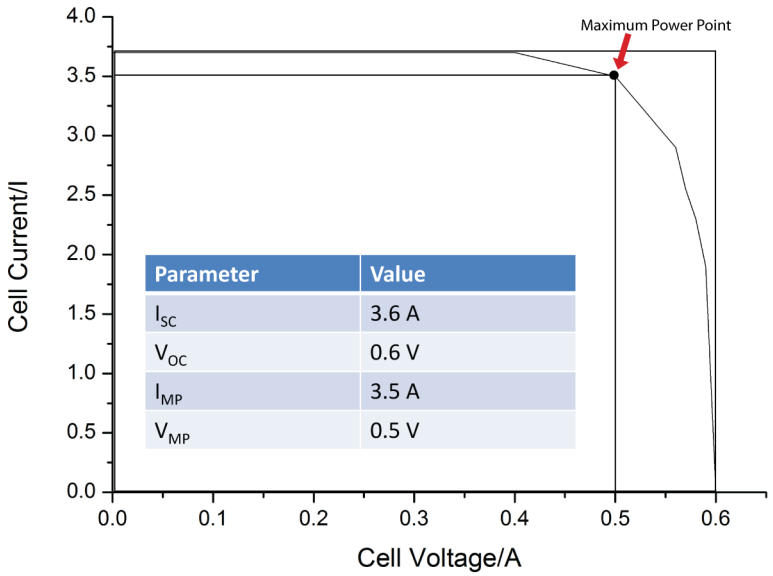

Figure 19: I/V curve for silicon solar cell.

The resulting curve looks as such and is vital in understanding important figures when discussing solar cells such as the short circuit current, open circuit voltage, maximum power point and fill factor. As can be seen from the graph at open circuit voltage, the cell current is zero and hence no power can be extracted. Also at short circuit current point the cell voltage is zero and hence no power can be extracted from the cell. As the load voltage is applied at small increments the diode current is negligible and the output current is or is close to the short circuit current, I_{SC}. When the voltage is applied at a significant value, at open circuit for instance, all the current generated flows through the diode and hence the cell current is zero. There is a point on the curve where there is a relationship between the maximum voltage (V_{MP}) and the maximum current (I_{MP}), giving the largest amount of power, known as the maximum power point (MPP). As can be seen from figure 19, there are two areas defining the maximum power point relating to the V_{MP} and I_{MP} and the area relating to the V_{OC} and I_{SC}. The ratio of these two areas is known as the fill factor (FF)

and is a measure of the performance of the photovoltaic cell.[102,105] It is expressed as:

$$FF = MPP/V_{OC}I_{SC} = V_{MP}I_{MP}/V_{OC}I_{SC} \tag{42}$$

This leads on to the essential value of solar cells, which is the solar cell efficiency, η, defined as:

$$\eta = MPP/P_{in} \tag{43}$$

P_{in} = Intensity of the incident light per unit area It follows that if the value of I_{SC} is large then the energy bandgap of the semiconductor exploited to absorb the incident light is small, as a larger proportion of the spectrum of the solar energy will be absorbed. V_{OC} is also related to the energy bandgap of the semiconductor, such that V_{OC} increases as the energy bandgap of the semiconductor used to absorb the light is increased. Crystalline silicon based solar cells are not used extensively because of their limited flexibility, heavy weight and high cost despite them having a high solar to electric energy conversion efficiency. The indirect bandgap (i.e. shifted conduction band) for silicon is approximately 1.1 eV at ambient temperature. As a result of the indirect bandgap the optical absorption coefficient is low ($\alpha \approx 100\ cm^{-1}$). As a consequence of this, the silicon needs to be several hundred microns thick in order to absorb the incident light. The electron-hole pairs generated by the light should be able to diffuse up to that distance to reach the electric field in the depletion region of the junction if they are to contribute to the photocurrent. The ability of the carriers to diffuse into the junction region is measured by the minority carrier (i.e. holes in N-type semiconductors and electrons in P-type semiconductors) diffusion length, L:

$$L\alpha\sqrt{\mu\tau} \tag{44}$$

where μ is the mobility and τ is the lifetime of minority carriers in the light absorbing region. Both of these parameters are sensitive to material purity and crystallinity. Efficient devices can only be produced if the feedstock is pure enough and crystal defects minimised. As

PV sales have accelerated rapidly over the past 5 years, manufacturers are considering purifying silicon themselves for use in PV solar cells. There are various types of materials that have been explored in photovoltaic cell development, such as:

- Silicon solar cells
- Dye sensitised and organic solar cells
- CdTe and copper indium gallium selenide (CIGS) solar cells
- III-V, quantum well and thermophotovoltaic solar cells

As well established as Si solar cells are, in terms of the technology and performance, the underlying problem is cost. The thin film route provides a very attractive way of reducing the costs associated with bulk silicon solar cells as well as retaining efficiency. Dye sensitised solar cells (DSSCs) are low cost solar cells which belong to the thin film group of solar cells. DSSC technology is remarkable, in that it mimics natural photosynthesis in two respects:

1. it uses an organic dye to absorb photons of light and results in a flow of electrons and
2. multiple layers are used to improve the absorption and collection efficiencies.

The basic working principles behind DSSCs and the rationale for continued research in DSSCs is presented in the next section.

1.4.2 *Dye Sensitized Solar Cells*

Dye-sensitization of semiconductors can be traced back to 1873, when Hermann Wilhelm Vogel accidentally discovered that when a photographic emulsion of silver halide was contaminated with a green dye it made the film much more sensitive to red light. In 1976, Tsubomura *et al.*[106] showed that larger photocurrents could be achieved by dye-sensitization of porous micro-crystalline zinc oxide compared to using a single crystal of zinc oxide (i.e. by increasing the surface area for light harvesting). It was not until 1991, when Michael Gratzel and co workers, sparked interest in photoelectrochemical cells again by using a mesoporous layer of titanium dioxide sensitized via an adsorbed ruthenium dye which showed efficiencies of > 7 %.[58] The fabrication

of DSSCs usually involves the use of a conducting contact and a TCO contact. The conducting plate is coated with a colloidal titanium dioxide paste, with particles ranging from 10-40 nm, usually deposited by screen printing or spray coating. The titanium dioxide layer is then sintered in air at 500°C to produce the mesoporous layer (thickness is roughly 10 μm) with a porosity of about 50 % which is then left to soak in a ruthenium dye (cis-bis(isothiocyanato) bis(2,2'-bipyridyl-4,4'-dicarboxylato)-ruthenium (II) bis-tetrabutylammonium). The second plate is then coated with a thin film of platinum by sputtering or chemical methods. The two plates are then sandwiched together by means of a hot melt polymer such as Surlyn, under pressure and then an electrolyte (iodide/tri-iodide) is added through pre-bored holes in the glass and then finally sealed. They are highly attractive because of the low cost of materials required to assemble one and also because of their high conversion efficiency.[55,56,58,107]

DSSCs differentiate from the silicon design of PV cells in that the photoelectrons are provided by the photosensitive dye and the bulk of the semiconductor is used for charge transport whereas the silicon itself is used to generate the photoelectrons as well as to present the electric field. DSSCs work when sunlight enters the cell through the TCO top contact and photons with enough energy to be absorbed strike the dye. Electrons are then injected into the conduction band of the semiconductor material (e.g. TiO_2) of the cell and move by diffusion until they reach the conducting substrate. The dye is now in its excited state. As the dye has lost an electron (dye^+) it strips an electron from the electrolyte material, normally iodide/triiodide redox couple. The dye oxidises the iodide into triiodide, which has to occur quickly in comparison to the electron/hole recombination process. The triiodide then combines with the electrons (after flowing through the circuit) at the counter electrode and form the iodide ion.[80,108–110]

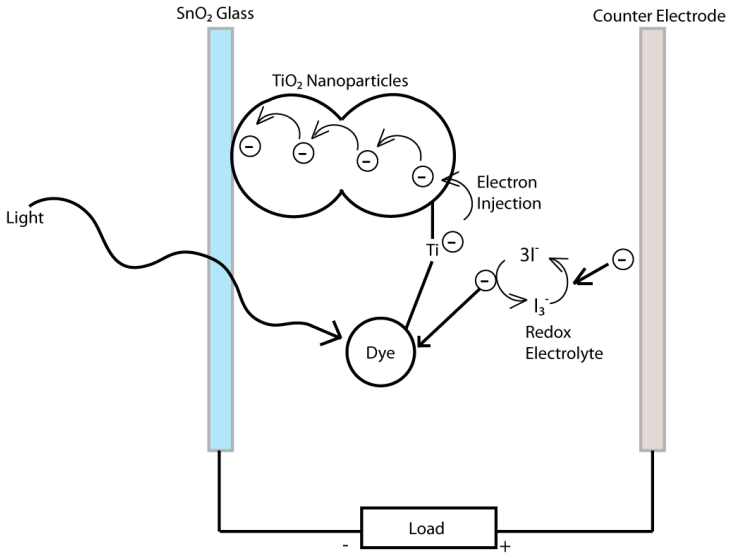

Figure 20: DSSC structure and reactions within the cell.

Figure 20 shows the structure of a DSSC based on TiO_2 and the reactions within the cell. The diagram however does not highlight the potential loss mechanisms such as luminescent emission from the dye, series resistance (the sheet resistance of the substrate electrode, the resistance of the semiconducting material and the resistance of the electrolyte), recombination effects and reaction of the electrolyte with TiO_2. The energetics of DSSCs are brought about by the relative positions of the energies of the TiO_2 conduction band, the highest occupied molecular orbital (HOMO)/lowest unoccupied molecular orbital (LUMO) energies of the of the dye and the redox energy of the electrolyte. The energies must be arranged such that the LUMO of the dye lies above the conduction band of the TiO_2 and the redox energy must be higher in energy than the HOMO in order to regenerate the dye molecule.[57,80,107,108,111,112] The driving force for electron and hole transport in any solar cell is the free energy gradient or electrochemical potential. In a conventional solar cell, only small gradients are required to drive the short circuit current as the mobilities of the electrons and holes are two orders of magnitude higher than that of DSSCs due to the high purity of silicon based solar cells. It has been investigated that the role of in-built fields do not govern the movement of the electrons as an in-built field (depletion layer) only exists at the interface between the conducting electrode and mesoporous titania layer, through which the electrons can tunnel through. Given this problem, larger gradients are required in DSSC to drive typical

solar cell current densities. Electron transport and electron transfer are disipative processes and result in energy losses and ultimately efficiency losses.

Cameron and Peter considered the nature of energy losses in DSSCs by considering the possible routes of electron recombination. Taking a typical three phase contact consisting of FTO/titania/electrolyte, electron recombination can occur via three possible routes.[108,112] The first route is the transfer of electrons from titania to the oxidised dye, the second route is from the the titania to the electrolyte and the third is from the FTO surface to the electrolyte. Some terms must be defined before this is explored more deeply. At open circuit conditions the injection of the electrons from the photoexcited dye molecules must be balanced by the sum of all possible back reaction routes as mentioned above. Under illumination, the electron concentration in the titania increases until it creates a recombination flux equal to the injection flux. The free energy of the titania particles is expressed by the position of the Fermi level in the semiconductor. The measured V_{OC} is the difference between the free energy of the electrons at the "dynamic equilibrium" concentration and and the electrolyte potential. The two main determinants of V_{OC} are the recombination rate constant and more subtley the conduction band offset relative electrolyte potential.[57,108] If the recombination rate constant increases, then the equlibrium concentration of electrons along with the free energy of the electrons and ultimately the V_{OC}. It has been stated that the second determinant has a more subtle effect on the open circuit voltage. If a material with no defects is used, then the injected electrons all occupy the conduction band and the Fermi level lies below the conduction band by a factor that only depends on the electron concentration. A given n will give a particular V_{OC}. By changing the electric field between the TiO_2 and the electrolyte, the states in the TiO_2 are all shifted relative to the electrolyte including the conduction band and the Fermi level. For the same number of states, n, a difference in the V_{OC} will be recorded identical to the change in the electric field at the titania surface, thus assuming electron injection, regeneration and recombination rate constant all stay the same in trap rich TiO_2 used in DSSCs this is the case, except that the charge density for a given Fermi level is determined by the distribution of electron traps. Changing the surface electric field does not change the energy distribution of the trap relative to the conduction band and as a result a change in

V_{OC} is expected and is linked to any change in the conduction band offset.

At short circuit conditions, the available free energy in the charges is used and extracted with maximum quantum efficiency. The efficiency depends on the diffusion constant (mobility) and recombination rate of the electrons in the TiO_2. Durrant and O'Regan stated that the determinants of efficiency are key to cell construction and the material properties i.e. TiO_2 thickness and photocurrent losses due to thickness.[57] As photoinjected electrons enter the conduction band of the TiO_2 the density gradient builds up across the cell until it is large enough to carry it to the FTO sink. Transport in TiO_2 is slow and a large density of charge carriers results. This causes a recombination flux. The magnitude of this recombination flux gives the photocurrent collection efficiency. The diffusion length links the relationship between transport and recombination. In general a diffusion length $>$ 2 times the film thickness is required to ensure most of the charges reach the FTO electrode before recombining. At short circuit illumination the recombination from the FTO to the electrolyte is is negligible and mainly limited to the bulk of the TiO_2 film. At open circuit conditions the back reaction from the FTO surface becomes apparent as the quasi Fermi level in the FTO moves up as a result of the photostationary state achieved by injection and recombination. As a result of the latter, Cameron *et al.* analysed thin "blocking" layers of TiO_2 deposited on the surface of the FTO to inhibit the back reaction of electrons to the electrolyte.[108,112] It was seen that the doping densities, thickness and band alignment are key issues in the performance of the blocking ability of these layers and that under strong illumination at open circuit (or on load), the blocking films no longer inhibit the back reaction due to a build of surface electron density, but under short circuit conditions the films act as blocking layers.[107,108,110,112]

New techniques and synthesis methods show how far DSSCs have evolved with regards to the different substrates that are being utilised as well as dye molecules that are being explored. As well as the obvious physical considerations such as the semiconducting material and the dye molecule, the choice of substrate is also important. DSSCs have usually been built on glass substrates, the disadvantages however are the large-scale industrial manufacturing of the cells. Flexible and light weight metal substrates and plastic foils are low cost alternatives, because the actual cost of the glass is 15-20% of the total

price of the cell. As well as fabrication of the solar cell, the upscale from small-scale laboratory to high throughput industrial production is equally important. The use of TiO_2 films for use as photoanodes in DSSCs has been widely investigated.[82,113–116] ZnO films have recently been explored with regards to their performance as photoanodes in DSSCs. The reason being that the energy level of the conduction band is comparable to that of TiO_2 as well as having higher electronic mobility.[32,96,111,117–119] The mobility is of the order of 100 $cm^2/V.s$ and the direct bandgap is 3.37 eV (300 K).[35,70] The electron transport properties are heavily affected by the material microstructure and the conditions in which it was synthesized. Zinc oxide has the richest family of nanostructures and ZnO tetrapods used in DSSCs have proved successful. The applications of ZnO are vast, for instance being used in gas sensors, transparent electronics, and surface acoustic wave devices. Thin films of ZnO can be prepared by various methods such as electrodeposition, sol-gel routes, CVD, laser ablation, molecular beam epitaxy and chemical bath deposition.[9,93,120] The sol-gel and chemical bath deposition routes are very effective, simple and low cost in comparison to some of the other methods mentioned. However conversion efficiencies of ZnO structured solar cells with Ru dyes, as those in TiO_2 have been lower than that of titanium dioxide based solar cells, and the studies showed that the electron injection process from the dye to the semiconductor material made no real difference when compared against TiO_2.

1.5 MICROPOROUS OXIDE FILMS

1.5.1 *Zeolite Powders*

Zeolites are microporous crystalline aluminosilicates, composed of TO_4 building blocks, linked together by corner sharing oxygen atoms, where T = Si/Al. The incorporation of aluminium into the zeolite framework, gives the framework an overall negative charge which needs to be compensated for by extra-framework cations, usually in the form of Na^+/H^+.[121–124] [122] These tetrahedra then link together to form rings of different sizes. Rings of up to twenty sizes have been prepared but rings usually contain 4 to 12 tetrahedra. The idealised geometry of these rings is planar, but they usually have more complicated shapes and geometries. These are also known as the primary

building units, which can then be linked together to form polyhedra and cubes. The linking of these secondary building units (SBUs) in an infinite repeating latice, give the rise to varied zeolitic framework structures. The rings on the face of polyhedra can be classified as pores and polyhedra with faces no larger than 6 rings are known as cages, since they are too small to accommodate molecules larger than water. Polyhedra with at least one pore larger than 6 rings are classified as cavities. Pores which have more than 6 rings that extend infinitely in one dimension are known as channels and allow the diffusion of molecules through them. If the effective width of the channels is known and the kinetic diameters of different molecules, it is possible to determine framework specific molecules. Currently, there are 20 known frameworks with varying degrees of composition. The general composition of zeolites can be split into three groups: the extra-framework cations, the framework and sorbed species within the pores of the zeolites.[122]

The overall formula for zeolites is: $M^{m+}_{x/m}[Si_{1-x}Al_xO_2]^{x-}.nH_2O$. The Si/Al ratio can range from 1 to ∞ depending on the synthesis conditons. The Si/Al ratio can also be modified post-synthesis. This composition also gives rise to certain properties synonomous with zeolites. The non-framework cations for example result in acidity, when H^+ is the charge compensating cation coupled with the large surface area and pore structure of zeolites, result in ideal acid catalysts. Zeolite Socony Mobil-5 (H-ZSM-5) for example is used as a solid acid catalyst for hydrocarbon alkylation, cracking and isomerisation. Functionality in the form of catalytic sites can be introduced into purely siliceous zeolites by isomorphous substitution with Fe^{3+}, Ga^{3+}, Ti^{4+} and Ge^{4+}, where the metals occupy silicon sites within the framwork. The composition then reduces to $M^{m+}_{(4-n)}.[Si_{1-x}X^{n+}_xO_2]^{(4-n)x-}.nH_2O$. TS-1 for example is a titanosilicate zeolite with a mordenite framework inverted (MFI) structure (figure 21), where titanium ions occupy the silicon sites, with the titanium concentration about 1-2%. TS-1 was patented by EniChem in 1983 and is a useful catalyst for a variety of reactions as shown in figure 22.

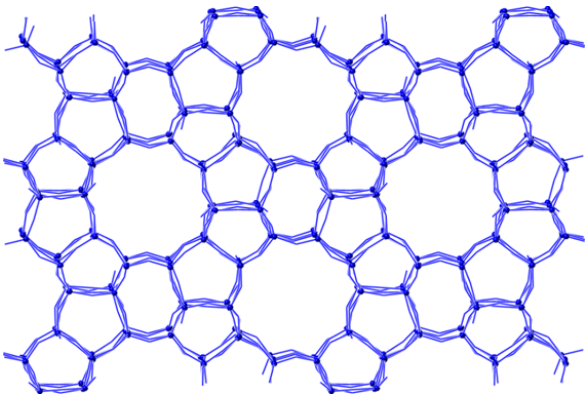

Figure 21: Structure of TS-1 zeolite viewed down the *c*-axis.

The extra-framework cations also allow for selective exchange. The extra-framework cations are loosely bound in channels/cages but usually at well defined sites, but can be exchanged. For example zeolite A and zeolite X are used in detergents as a water softeners due to their high affinity for Ca^{2+} and Mg^{2+} respectively. Zeolites are also vital in the removal of radioactive Cs^{+} and Sr^{+} from radioactive waste. Zeolites also find applications as adsorbants for small polar molecules or are used in bulk molecular separation as molecular sieves. The most common examples include gas separation and petroleum refining.

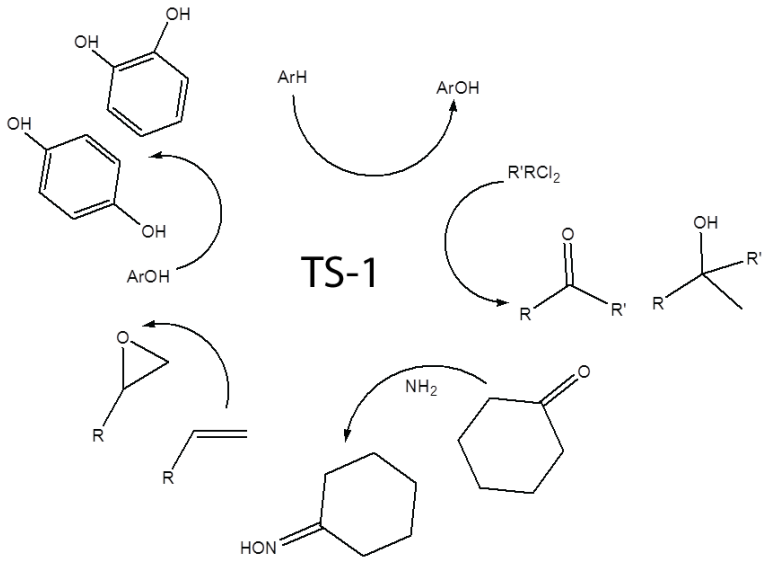

Figure 22: Example of catalytic reactions performed by TS-1 zeolite.

Zeolites in their powder form continue to be used extensively, but given increasing energy considerations, it is more viable to use a zeolite in its film form, as this serves as a long lasting alternative

to a zeolite powder. Given that the film meets certain microstructural requirements then these films can serve as alternatives to zeolite powders. Zeolites in their film form can also have new applications compared to their powder form. For example, zeolite overlayers are used extensively in the gas sensing industry to increase the sensitivity and selectivity to oxidising and reducing gases.[125–129] Zeolite films also find application in electronics industry as purely siliceous zeolites have lower dielectric constants than their dense analogues. There have also been reports of zeolite films for use in corrsion science as well as being used as catalytic membrane reactors.[130]

1.5.2 *Zeolite Films*

The main driving force for zeolites in their film form have been addressed in the previous section. Zeolite films have been known since the 1940s, when they were first synthesized in what can be described as a brute force approach, by pressing zeolite powders into pellets.[127,128] Reactions were also carried out in the surfaces of zeolite single crystals. The performance of these rudimentary zeolitic films was poor and the processing challenge for high performance zeolite membranes became apparent. There has been a large amount of research invested in the last 25 years on zeolitic films in order to optimise the processing challenge as well as controlling particle morphology and microstructure which is key to the overall peformance of the zeolite film for a given application. The first commercially available zeolite films were concentrated to small-scale applications and the films were coated on 10 m^2 substrates. The main issues in commercialisation, despite the intense research, has been the high cost of fabrication, poor performance of the zeolite films compared to powder analogues and major difficulties in reproducibly coating large substrate areas.[131–136] Large area coatings inevitably require reliable processing technologies, while satisfying essential film characteristics such as film continuity, thickness control, crystallite orientation (pore orientation) and pin-hole (defect) free films.[121,137,138] The established laboratory scale routes to zeolite synthesis are *in-situ* crystallisation and secondary seeded growth.[123]

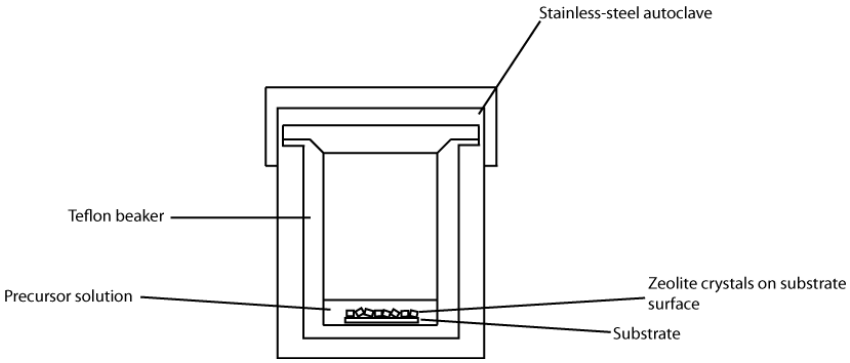

Figure 23: *In-situ* crystallisation process

In-situ crystallisation is where the precursor zeolite solution (sol) is brought into direct contact with the support before hydrothermal treatment. Zeolite film formation proceeds initially through the formation of a gel phase on the support surface. Nucleation and crystal growth then occurs at the boundary between the gel and liquid phase. Crystal growth can then lead to the formation of a continuous zeolite film. Post-processing of the zeolite films is often required to remove organic molecules, often employed as structure directing agents.[123] *In-situ* crystallisation often involves suitable surface functionalisation of the support in order to provide sufficient attachment of the zeolite crystals to the support. This process is also very sensitive to sol composition and synthesis conditions (temperature, reaction time, sol aging and pH). *In-situ* crystallisation often results in polycrystalline zeolite films as a result of crystal growth occuring simultaneously at multiple layers and can also result in films with intercrystalline gaps. Multiple treatments to fill intercrystalline defects can result in sufficiently thick films which can limit the application of the membrane.[123]

The second widely used method to prepare zeolite films is secondary (seeded) growth. This is a better approach to synthesising zeolite films in that it fulfills the requirements for a useful zeolitic film compared to *in-situ* crystallisation, of which the drawbacks have been mentioned. Secondary seeded growth effectively decouples nucleation from the film growth process. The process involves:

- the formation of seed crystals, in which the size and shape of the crystals can be controlled,
- deposition of the seed crystals on the desired support to form an oriented seed layer,

- followed by secondary and tertiary treatment (if required) of the seed crystals to form a monolayer with aligned crystals and pores.

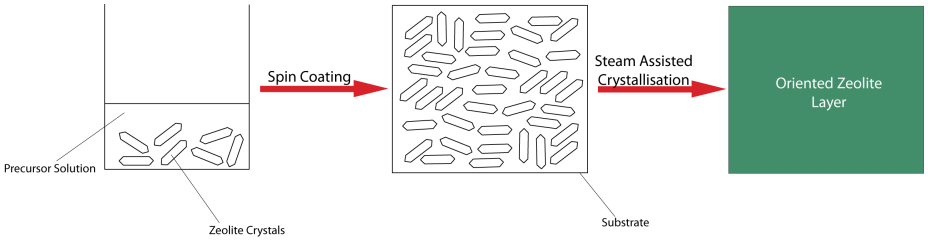

Figure 24: Secondary (seeded) growth process

This approach allows for greater control of crystallite and pore orientation.[129,139–146] The synthesis of the colloidal zeolite suspension of the seeds usually occurs at low temperatures allowing for control over seed size, homogeneity and yield.

1.6 SUMMARY

The introductory chapter has outlined the materials processing techniques and has mainly focussed on chemical vapour deposition and the basic physics crucial to understanding semiconducting thin films. Transparent conducting oxides were looked at in particular due to the wide range of applications for this class of materials as well as novel synthetic routes to microporous oxide materials as films which have potential use in areas ranging from corrosion resistance to microelectronics as dielectric films.

The importance of these materials should not to be overlooked as they play a major part in changing our current habits with respect to fossil fuels consumption and moving towards more reliable renewable sources of energy.

Chapter 2 describes the experimental set-up used to deposit thin films by CVD and hydrothermal/solvothermal synthesis and the theoretical basis behind the techniques used to characterise the films. The main analytical techniques in this thesis have been X-ray diffraction to determine the long range structure and scanning electron microscopy to determine the microstructure of the films. X-ray absorption spectroscopy was also used to determine the short-range order of some of the systems investigated.

Chapter II

EXPERIMENTAL AND CHARACTERISATION METHODS

2

EXPERIMENTAL

2.1 INTRODUCTION

This chapter serves to discuss the experimental methods used to deposit thin films by CVD describing both the set-up used in AACVD, APCVD and hydrothermal methods. The theory behind the analytical techniques and data analysis conducted on the films is discussed. The main analytical techniques this chapter concentrates in is X-ray dffraction (XRD), scanning electron microscopy (SEM) and X-ray absorption spectroscopy (XAS).

2.2 SYNTHESIS TECHNIQUES

2.2.1 *CVD Set-Up*

Atmospheric pressure and Aerosol Assisted Chemical Vapour Deposition (APCVD) and (AACVD) respectively was performed on a horizontal-bed, quartz, cold-walled tubular carbon reactor with a laminar gas flow.

The reactor consists of a cylindrical quartz tube, 60 mm in diameter and 160 mm in length. There is a carbon block contained within the quartz tube which holds a cartridge heater and and two thermocouples. The quartz tube is capped by two stainless steel end plates at both ends. Gas is allowed to enter through one of the stainless steel end plates by use of a brass manifold and allowed to exit the reactor via an exhaust at the opposit end. The desired substrate was cleaned

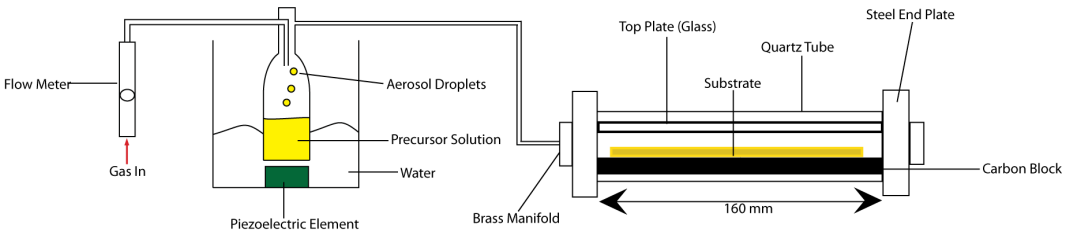

Figure 25: Schematic of the AACVD set-up used to deposit films.

in piranha solution and rinsed with copious amounts of distlled water, dried and then placed ontop of the carbon block and SiO_2 coated float glass supplied by NSG placed 10 mm above to act as a top plate. Once the reactor was loaded with the substrate, top plate and sealed the substrate was then directly heated, hence the overall experimental set-up is cold-walled.

For an aerosol delivery system (AACVD), the precursor was loaded into a glass flask with a thinned base which allows for more power transfer from the piezoelectric element allowing for easier aerosol generation. The application of high frequency sound waves, known as ultrasonic generation, produces droplets where the size is related to the density and surface tension of the solvent as well as the operating frequency of the piezoelectric and are associated by Lang's equation. The average droplet size produced using a standard humidifier (20 kHz) and methanol as the solvent is 45 μm. The aerosol is then carried towards the reaction chamber using a plain flow of nitrogen gas (BOC). The aerosol passes through a brass manifold, engineered such that laminar flow is achieved across the width of the reactor. Once the reaction has ceased, the substrate was cooled under a flow of nitrogen to room temperature and the films handled in air.

For a vapour delivery system (APCVD), the precursor was loaded into bubblers in this manner. The temperature of the bubbler was set by the vapour pressure of the precursor and the desired flow rate. The desired substrate was cleaned in piranha solution and rinsed with copious amounts of distlled water, dried and then placed ontop of the carbon block and SiO_2 coated float glass supplied by NSG placed 10 mm above to act as a top plate. Once the reactor was loaded with the substrate, top plate and sealed the substrate was then directly heated as mentioned before. Nitrogen was then passed through the bubblers containing the precursors and the bypass valve closed so that the flow could stabilise through the exhaust. Once the flow had stabilised for approximately 30 s the three-way valve was turned to allow the precursors to enter the mixing chamber and then to enter the reaction chamber. Once the reaction had ceased the precursor flow was diverted to the exhaust and the flow through the bubbler was diverted to the bypass. The reactor was turned off and the substrate was cooled in a flow of nitrogen to room temperature. All samples were handled in air and stored in plastic bags.

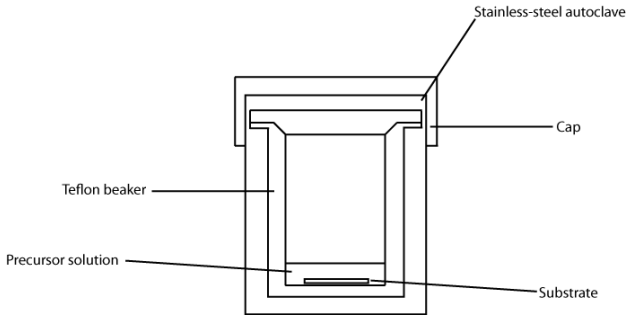

Figure 26: Schematic of apparatus used in a typical hydrothermal synthesis.[122]

2.2.2 *Hydrothermal Synthesis*

Hydrothermal synthesis involves crystallising materials from high temperature aqueous solutions under autogenous pressure. HT synthesis was typically carried out in a steel pressure vessel known as an autoclave. Within the autoclave a temperature gradient is established and maintained at the opposite eneds of the growth chamber such that the hotter end aids dissolution and the cooler end aids crystal growth. Figure 26 shows a schematic of the apparatus used in a typical hydrothermal synthesis starting from a dry gel and water. The crystal growth mechanism for hydrothermal synthesis is a contentious issue, but is deemed to proceed via a solid/solid transformation.[122,147,148]

2.3 CHARACTERISATION TECHNIQUES

2.3.1 *Powder X-ray Diffraction (PXRD)*

All diffraction work was performed on polycrystalline thin films, which can be thought of as analagous to powders. X-rays are diffracted from a set of periodic planes (in actual fact by the electron cloud of atoms) according to the Bragg equation. The separation between these planes of atoms, known as Miller planes is of the order of planes 10^{-10} m, therefore the wavelength of light which is diffracted from these planes corresponds to X-rays. The information gleaned from PXRD is very rich and as it tells us the phase of the material, lattice parameters of the the unit cell and atomic positions as well as crystallite size and crystallite strain. Before moving on however, the distinction between single crystals and powders should be discussed.[149,150]

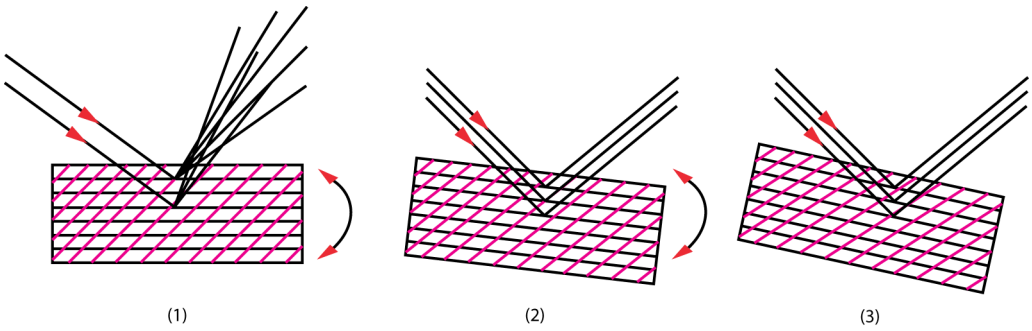

Figure 27: The interaction of a crystallite with incoming X-ray.

A crystal is developed by adding the unit cell (identical building block) up in all dimensions. Crystals observed in every day life (e.g. diamond, quartz, silicon) typically contain about 10^{18} unit cells. These are more typically single crystals, but powders are also composed of very small crystals known as "crystallites". Powders viewed under an electron microscope easily show crystallites. Powders viewed under an electron microscope may look like minute crystals, i.e. scaled down versions of larger crystals or may have no distinguishing morphology.

In order for a polycrystalline thin film or powder to give rise to a diffraction event the crystallites must be correctly oriented with respect to the X-ray beam of a fixed wavelength. Figure 27 shows the interaction of a crystallite with an incoming X-ray beam. A set of planes (black) in (1) results in incoherent scattering of the incident X-rays. By rotating the crystallite the planes would rotate with the crystallite and there comes a point, (2), where the planes are correctly oriented with respect to the X-ray beam in rder to diffract in phase resulting in an intense diffracted ray.[149]

If the rotation was to continue to point (3) in the diagram then a second set of planes in purple would be correctly oriented in order to give rise to a diffraction event. If the crystallite was reoriented through all possible orientations such that every set of planes had the opportunity to diffract then over a period of time would result in many diffracted rays. A powder consists of many millions of crystallites each at different orientations with respect to the X-ray beam and statistically speaking there will be some at the correct orientation for diffraction to occur in contrast to manually rotating and re-orienting

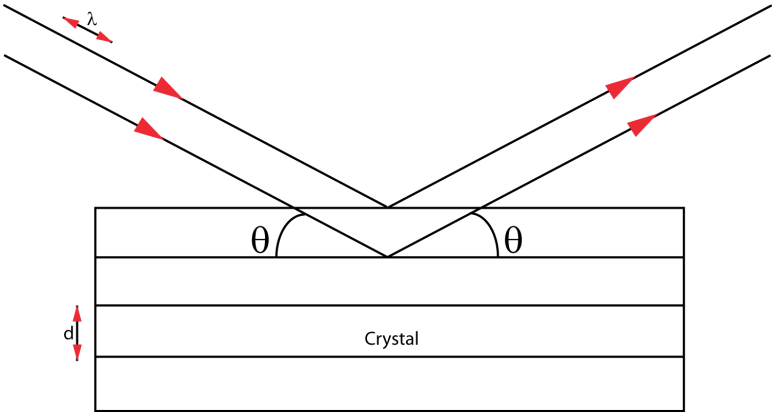

Figure 28: Schematic of X-ray diffraction from part of a single crystal.

a single crystal. In order for a crystal to diffract light, the Bragg equation must be satisfied:

$$n\lambda = 2d.sin\theta \tag{45}$$

where λ is the wavelength of the radiation used, d is the spacing between the planes and ϑ is the angle between the incident (or diffracted) ray and the corresponding crystal plane; n is an integer and is referred to as the order of diffraction and is often unity.

Figure 28 shows the idea behind Bragg's Law, that when achieved, X-ray beams scattered from successive planes in a crystal travel different different distances. If the difference is an integer number of wavelengths then the X-rays scattered from successive planes will interefere constructively when they reach the detector.[64,149]

The position of a diffracted peak gives information about the unit cell parameters whereas the intensity of a diffracted peak gives information about the atomic positions. The intensity of a diffracted X-ray beam is given as:

$$I_{hkl} = cjPLAF^2_{hkl} \tag{46}$$

where j is the multiplicity (symmetry equivalent reflections), P is the polarisation factor (polarisation of an X-ray photon can change as a result of scattering/diffraction), L is the Lorentz factor (geometric correction), A is the X-ray absorption (X-rays are absorbed as they pass through materials) and F is the structure factor (mathematical

treatment of how atoms scatter light). If the structure factors F_{hkl} are known for a full set of reflections then the electron density, at any position xyz in the unit cell can be calculated, corresponding to atomic positions. It is possible to measure F^2_{hkl} and consequently $|F_{hkl}|$ but not the sign of F_{hkl}. Computer programmes are often required to solve the structure, but more importantly a combination of X-ray and neutron diffraction is desirable.

PXRD data collected was used mainly for phase identification, unit cell refinement to yield lattice parameters, qualitative analysis of preferred orientation and crystallite size calculation. Unit cell refinement was performed via the Le Bail method, which estimates the reflection intensities without a structural model in contrast to the Rietveld model which estimates reflection intensities from a starting model. In the Le Bail[151] method all the reflection intensities are set to an arbitrary value and are treated as "calculated" values as if they had been derived from a structural model (i.e. Rietveld). The Rietveld code is then modified to extract "observed" intensities.[152,153] These observed intensity values will be biased by the starting values set for the "calculated" intensity but closer to the true value for the observed *I(hkl)* than any arbitrary value. The "calculated" intensity is then set to the value of the "observed" intensity and a least squares refinement performed on the diffraction profile to yield cell parameters and peak positions as well as resolution parameters such as peak widths and peak shapes. This procedure is then iterated so that a new set of observed intensities are obtained. As well as obtaining information about the unit cell parameters, peak shape also yields valuable information such as crystallite size and strain vital to materials chemistry. There are several parameters regarding peak shape that should be defined:

- Peak maximum (or peak height) is often denoted as I_{max} although it should not be used as an indicator of diffracted intensity.
- The area under the peak is generally taken as the peak intensity as it represents the sum of all the diffracted X-ray photons that have been detected regardless of peak shape.
- The broadness of a peak is dictated by the peak width. The full width half maximum (FWHM) of the peak is a common parameter describing peak width.

Peak broadening arises from two main sources:

1. Instrumental contributions
2. Sample contributions

Instrumental broadening arises from a variety of factors such as:

- the radiation not being perfectly monochromatic
- the source of the radiation has a finite physical size
- axial divergence of the incident and diffracted beam
- slit configuration in the diffractometer and
- misalignment of the diffractometer.

Sample broadening arises from:

- the size of the crystallite
- the micro-strain in a crystal lattice due to dislocations and concentration gradients
- stacking faults and twins which are grouped as structural mistakes and
- concentration gradients in inhomogenous compounds.

In order to determine sample broadening effects which may yield information about the size and stress of the diffracting crystallites, it is vital to remove any instrumental broadening effects by using a near perfect standard sample exhibiting zero sample broadening. A standard should be chosen so that the absorption of X-rays is similar to the sample in question. The measurement is then repeated to give the broadening effects of both the sample plus the instrument.[149] The instrument contribution is then substracted from the total to yield the broadening due to the sample only. The subtraction performed is dependent on the line profile (i.e. Gaussian or Lorentzian type). The crystallite size is given by the Scherrer relation who related the mean (volume average) crystallite size, L, of a powder to the broadening, β, of the diffraction peaks:

$$\beta_L = \frac{K\lambda}{Lcos\theta} \tag{47}$$

where ϑ is the Bragg angle in radians, λ is the wavelength of radiation used and K is a constant dependent on peak shape and crystallite shape, but is usually taken as 0.9. A common effect observed for thin film samples is that of preffered orientation of the crystallites. This is where the crystallites are oriented in a certain way resulting in fewer reflections being observed than expected. The degree of preferred orientation can be estimated by comparing the observed intensities in a diffraction pattern to a bulk standard. A method for achieving this was developed by Barrett and Massalski[154] and is known as the texture coefficient:

$$TC(hkl) = \frac{I(hkl)/I_0(hkl)}{\frac{1}{N}\Sigma_N I(hkl)/I_0(hkl)} \tag{48}$$

where TC is the texture coefficient of a given plane (hkl), I is the measured intensity, I_o is the intensity of a bulk powder and N is the number of reflections observed in the pattern. Any deviation of the texture coefficient from unity indicates a higher degree of preferred orientation of the crystallites.

XRD was performed using two machines. The Bruker-AXS D8 X-ray diffractometer with CuKα_1 and CuKα_2 radiation of wavelengths 1.54056 Å and 1.54439 Å respectively, emitted with an intensity ratio of 2:1, a voltage of 40 kV and current of 40 mA. This instrument allows for data to be collected at relatively short times by using a 2-D area X-ray detector to record large sections of multiple Debye-Scherrer cones simultaneously. Integration of the Debye-Scherrer cones after collection allows for a standard 1-D X-ray pattern to be plotted. X-ray diffraction (XRD) was also performed using a a Bruker D4 Endeavour X-ray diffractometer (theta/2theta mode) with CuKα_1 and CuKα_2 radiation of wavelengths 1.54056 Å and 1.54439 Å respectively, emitted with an intensity ratio of 2:1, a voltage of 40 kV and current of 30 mA.

2.3.2 *Scanning Electron Microscopy (SEM)*

SEM uses a high energy electron beam focussed on a sample to produce high resolution images of the sample surface. Bombardment of the sample surface with high energy electrons results in the formation of secondary electrons and backscattered electrons. Secondary elec-

trons are electrons ejected from the sample as a result of high energy electrons incident bombarding the sample.[155] As the kinetic energy of secondary electrons is generally low compared to that of backscattered electrons, they are normally recaptured by ionized atoms within the sample and thus can only escape from the surface of the sample. Backscattered electrons are electrons that have undergone elastic or inelastic scattering with the sample surface.[28] The kinetic energy of backscattered electrons is higher than that of secondary electrons. The intensity of backscattered electrons depends greatly on the atomic number. The scattering intensity is increased with atomic number number due to regions of higher electron density. Regions with higher electron density across a sample appear brighter in backscattered electron images. Scanning Electron Microscopy (SEM) was performed to determine surface morphology and film thickness using a JEOL JSM-6301F Field Emission SEM at an accelerating voltage of 4-5 keV. Images were recorded using SEMAfore software. Samples were coated with a sputtered layer of gold to enhance conductivity and reduce charging and allow for a conduction pathway between the film and the stage.

2.3.3 *Atomic Force Microscopy (AFM)*

Atomic force microscopy (AFM) was performed using a Veeco Dimension 3100 in contact mode, where a cantilever with an attached tip scans the surface of the sample to determine the surface topography.[73]

2.3.4 *X-ray Absorption Spectroscopy (XAS)*

X-ray absorption spectroscopy gives information on how X-rays are absorbed by an atom at energies near to and above the core-level binding energies of that specific atom. XAS is is extremely sensitive to formal oxidation state, coordination chemistry, coordination number and bond distances of the species around the atom being probed. Because of this, XAS is a powerful tool in determining the chemical state and local coordination environment of specific atoms within a material.[156] As it is an atomic probe, there is little prerequisite for samples and importantly sample crystallinity is not required. XAS experiments however do require intense and energy-tunable X-ray sources

which involves the use of synchrotrons.[157] XAS is usually divided into two regimes: X-ray absorption near edge spectroscopy (XANES) and extended X-ray absorption fine structure (EXAFS). XANES is used as a qualitative tool as it is extremely sensitive to formal oxidation state and coordination chemistry (e.g. octahedral, tetrahedral coordination environments) around the atom being probed where EXAFS is used to determine bond distances and coordination number of the neighbouring species around the absorbing atom. The main principle behind XAS is that when X-rays impinge on a material, an X-ray photon is absorbed by an electron in the material in a tightly bound core quantum level (i.e. 1s or 2 p level). The binding energy of the core level must be less than the energy of the incident X-ray in order for the photon to be absorbed.[157–159] As a consequence of this an electron is ejected as a photo-electron.[156] The probability that an X-ray will be absorbed is given by the absorption coefficient, μ, described by Beer's Law:

$$I = I_0 e^{-\mu t} \tag{49}$$

where I_o is the X-ray intensity incident on the sample, t is the sample thickness and I is the transmitted intensity through the sample. The absorption coefficient is a function of energy and is dependent on the sample density ρ, the atomic number Z, atomic mass A and the X-ray energy E:

$$\mu \approx \frac{\rho Z^4}{A E^3} \tag{50}$$

The Z^4 term allows for good contrast between materials and is why X-rays are useful in medical imaging. As the energy is ramped up in a XAS experiement there is a sharp rise in absorption, corresponding to the absorption edge of during the ejection of a photo-electron. A XAS experiment essentially shows how the absorption coefficient varies with energies at and above the absorption edge.

Once a photon has been absorbed a core hole is left behind. The relaxation pathways can be two-fold in order to fill the core hole. The first relaxation pathway is X-ray fluorescence, where a higher energy electron fills the core hole, resulting in an X-ray of well defined energy being emitted. The fluorescence energy is atom specific. The second

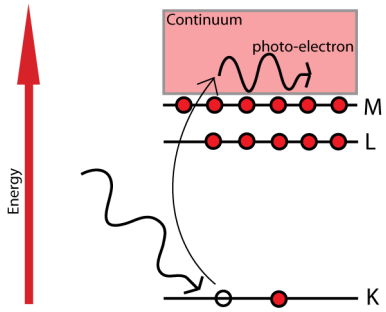

Figure 29: X-ray absorption by a core shell electron accompanied by ejection of a photo-electron.[156]

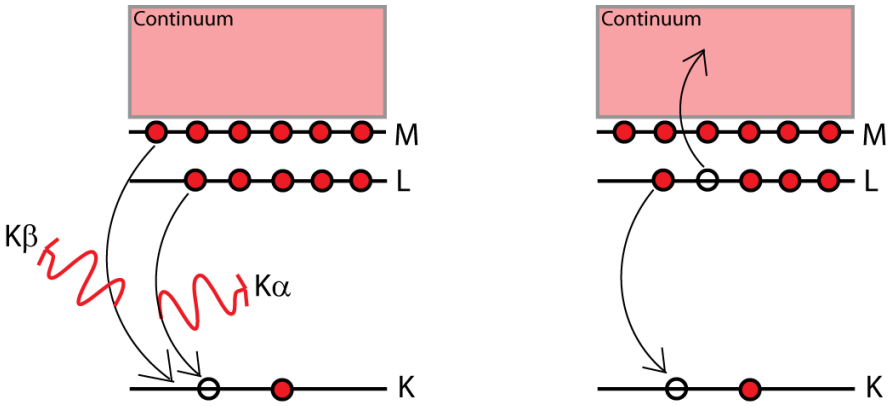

Figure 30: Relaxation pathways after absorption of an X-ray showing X-ray fluorescence (left) and Auger effect (right).[156]

relaxation pathway is where energy is emitted due to a higher energy electron filling a core-hole which results in the ejection of an electron (Auger electron). XAS experiments conducted in this thesis were carried out in fluorescence geometries. The absorption coefficient in transmission is given as:

$$\mu(E) = log(\frac{I_0}{I}) \tag{51}$$

whereas in fluorescence mode:

$$\mu(E) \propto \frac{I_f}{I_0} \tag{52}$$

where I_f is the measured intensity of a fluorescence line associated with the absorption process.

The XANES signal is much larger than the EXAFS signal and therefore the atom being probed can be in lower concentrations compared

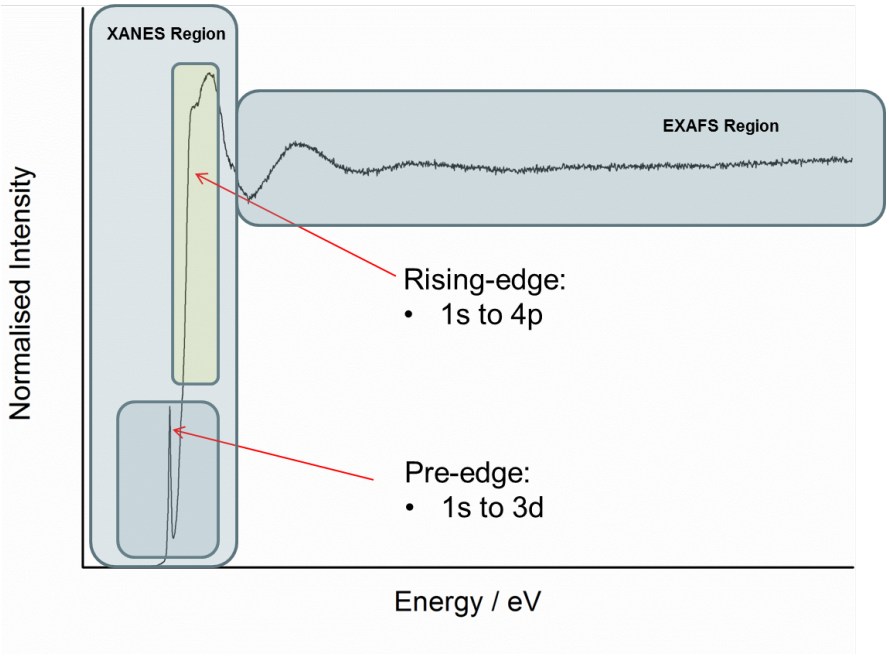

Figure 31: XAS for $TiSiO_x$ film showing the transitions attributed to the rising edge, absorption edge (i.e. XANES region) and the EXAFS region also.

to that of the EXAFS regime. Unfortunately there is not a XANES equation as the EXAFS equation breaks down at low-k due to the increase in mean free path at low-k. The XANES region is very useful though as the edge position is extremely sensitive to valence state, ligand type and coordination environment. The 3d levels in transition metal oxides are not normally involved in the absorption process unless there is strong hybridization between the metal 3d levels and the O 2p levels and XANES spectra is extremely sensitive to this hybridization. O 2p levels are normally too far away to result in mixing with metal 1s levels. The pre-edge feature in XANES region for example is most intense for metal ions having tetrahedral coordination and least intense for octahedral coordination; the intensity also depends on the electronic structure of the metal ions in a given oxidation state, for example systems with d^0 electron configuration tend to have the highest intensity.[156]

When looking at information for the EXAFS regime, the oscillations above the absorption edge are of interest as shown in figure 31. The EXAFS regime is best described by the wave-behaviour of the photo-

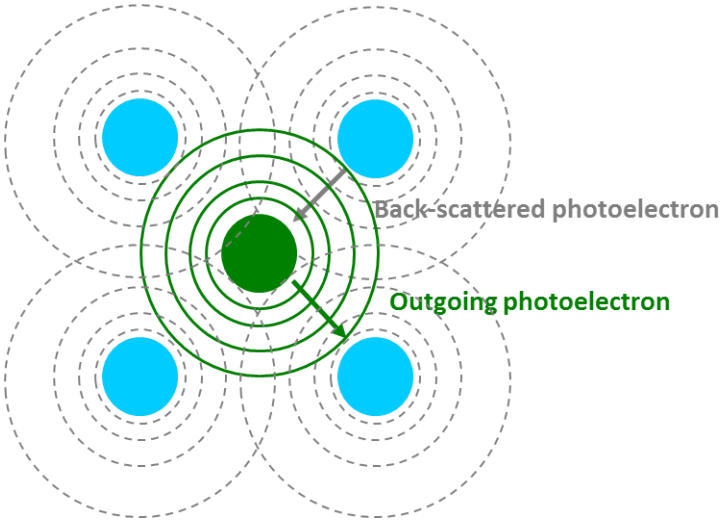

Figure 32: Schematic representation of the EXAFS process showing the interaction of the photo-electron and the back-scattered wave.

electron as shown pictorially in figure 32. The EXAFS fine structure is given by:

$$\chi(E) = \frac{\mu(E) - \mu_0(E)}{\triangle\mu_0(E)} \tag{53}$$

where μ(E) is the measured absorption coefficient, μ_o(E) is a smooth background which represents the absorption of the isolated atom only and $\Delta\mu_o$(E) is the step measured in the absorption μ(E) at the threshold energy E_o.

It is convention to convert the energy of the X-rays to k-space, the wave number of the photo-electron which is the inverse of distance and given as:

$$k = \sqrt{\frac{2m(E - E_0)}{(h/2\pi)^2}} \tag{54}$$

where E_o is the absorption edge energy and m is the electron mass. The quantity of note in EXAFS is χ(k) which is essentially the oscillations as a function of the photo-electron wave number. The oscillations in EXAFS decay with k and and is usually multiplied by k^3. The nearest neighbour coordination shells show up as different fre-

quencies in the oscillations in χ(k). These can be modelled using the EXAFS equation:

$$\chi(k) = \sum \frac{N_j f_j(k) e^{-2k^2\sigma_j^2}}{kR_j^2} sin[2kR_j + \delta_j(k)] \quad (55)$$

where f(k) and δ(k) are the scattering properties of the neighbouring atoms of the atom being probed, N is the number of neighbouring atoms, R is the distance from the atom being probed to the neighbouring atoms and σ^2 is the diorder in the neighbour distance. The number of atoms neighbouring the atom being probed, the bond distance and disorder can all be calculated knowing the scattering amplitude and phase shift.[156,158]

2.3.5 *UV/Visible/Near IR Absorption Spectroscopy*

UV/Visible/near IR spectra were taken using a Perkin Elmer Fourier transform Lambda 950 UV/Vis spectrometer over a wavelength range of 300 nm to 2500 nm in both transmission and reflection modes. The transmission spectra background was taken against an air background.

2.3.6 *Electrical Testing*

Hall effect measurements were carried out using the van Der Pauw method to determine the sheet resistance, free carrier concentration (N) and mobility (μ). A square array of ohmic contacts arranged on 1 cm^2 samples were then subjected to an input current of 1 mA and a calibrated magnetic field of 0.58 T. The transverse voltage was then measured. The measurement was repeated by reversing the direction of the magnetic field and the current. The magnitudes of the measured voltages were similar but with opposite signs indicating that the hysteresis was negligible. The Hall coefficient R_H was calculated from transverse voltage, dc current injected, the magnetic field and the film thickness.

2.3.7 *Raman Spectroscopy*

Raman microscopy was performed using a Renishaw In Viva system which consisted of a light microscope (Leica DL-LM; Olympus BX) coupled to a Raman spectrometer with a laser (Ar^{+}) excitation wavelength of 514.5 nm. The microscope was equipped with a 50 x objective (N-plan). The microscope optics were used to focus the laser beam onto the sample and to collect the scattered light to a focus of approximately 10 μm^2.The Rayleigh scattering component was removed using a notch filter. The instrument was calibrated against the Stokes Raman signal of pure Si at 520 cm^{-1}.

Chapter III

TIN DIOXIDE FILMS

3

FLUORINE DOPED TIN DIOXIDE FILMS

The following chapter describes the deposition of doped tin oxide films using Aerosol Assisted Chemical Vapour Deposition (AACVD) and Atmospheric Pressure Chemical Vapour Deposition (APCVD) on glass and polymer coated stainless steel substrates. The main dopants chosen for this study was fluorine (anionic) in order to observe any electrical/structural changes to the tin oxide system. It was found that the use of aerosol delivery system to deposit fluorine doped tin dioxide (FTO) resulted in films with enhanced functional properties in terms of sheet resistance and surface morphology for use as electrodes in solar cell devices compared to commercially available FTO coatings.

3.1 INTRODUCTION

Chapter one discussed the need for energy based materials and in particular the role that TCOs play in energy capture and conservation through a wide range of applications. As mentioned before TCOs are materials which combine optical transparency with electrical conductivity.[30,63] In order for materials to be transparent they must display a band gap greater than the highest frequency of visible light (3.1 eV). Metals for instance are highly conductive but do not transmit visible light and transparent materials such as glasses are insulators. By extrinsic doping with aliovalent elements the conductivity of TCOs can be improved. The introduction of impurities into the crystal structure results in donor states near the conduction band if the conductivity is n-type or acceptor states near the valence band if the conductivity is of p-type character. An important requirement in doping is that these states must be shallow in order to maintain optical transparency. These materials underpin the photovoltaic industry by providing the transparent electrodes for thin film amorphous silicon solar cells, dye sensitized solar cells (DSSC), flat panel displays in polymer light emitting devices.[55,56,60] For practical applications in devices ranging from solar cell electrodes to light-emitting diodes a TCO must have a resis-

tivity of less than 10^{-3} Ω.cm and over 80% transmittance in the visible region. TCO materials are generally limited to materials that show n-type conductivity such as In_2O_3, SnO_2 and ZnO although some p-type materials are known. Given the production cost of tin doped indium oxide (ITO) research into improving FTO and zinc oxide films must be increased. Conducting polymer films, such as polyaniline are also of interest primarily due to their flexibility but unfortunately are not stable in air. Fluorine doped tin dioxide coated glass has been exploited since the 1940s for use as an anti-fogging coating for aircraft windows by using an electrical current to heat the glass. Over 35 million sq. metres of F:SnO_2 are made annually in the USA. This has included a rapid increase in production for the photovoltaic industry. The use of fluorine doped tin dioxide for photovoltaic applications has risen from an almost zero market share in the year 2000 to a 50% share in 2009, with an impetus towards replacing sputtering deposition techniques with CVD and nanoparticle printing methodologies.[88,160] However, optimising the optical and electronic properties of TCOs for specific applications are a key commercial challenge.[52,53]

The following chapter investigates the use of Aerosol Assisted Chemical Vapour Deposition (AACVD) of doped tin dioxide thin films as a low cost, scalable alternative to traditional deposition techniques such as APCVD, dc/rf sputtering, sol-gel and spray pyrolysis.[1,29,78] The use of AACVD resulted in control over the electrical and crystal properties of films by optimising the temperature and dopant concentration. This work also highlights the crucial role which droplet size plays in the deposition process, for controlling morphology and physical characteristics of the films by comparing two methods of aerosol generation. Control over the film properties can be achieved through variations in temperature, dopant concentration and aerosol droplet size using Aerosol Assisted Chemical Vapour Deposition (AACVD)[161] and that this enables materials with enhanced functional properties keeping up with the increasing demands of novel technologies.

3.2 EXPERIMENTAL

Aerosol Assisted Chemical Vapour Deposition (AACVD) was performed on a horizontal-bed, quartz, cold-walled tubular carbon reactor with a laminar gas flow. The horizontal tubular reactor with a cross sectional area of 10 cm^3 was fitted with a top plate above

the substrate to limit the longitudinal roll convection and provide a laminar gas/aerosol flow. The aerosol which was fed over the heated substrate in the reaction chamber was produced using two distinct techniques: ultrasonic generation and Collision type. These two methods for aerosol droplet generation produce different size distributions of droplets, which in turn resulted in very different film characteristics. The application of high frequency sound waves, known as ultrasonic generation, produces droplets where the size is related to the density and surface tension of the solvent as well as the operating frequency of the piezoelectric and are associated by Lang's equation. The average droplet size produced using a standard humidifier (20 kHz) and methanol as the solvent is 45 μm. The aerosol is then carried towards the reaction chamber using a plain flow of nitrogen gas (1 l/min). This technique, which produced relatively large aerosol droplets, shall be referred to from here on in as ultrasonic-AACVD (u-AACVD).

In contrast to the ultrasonic technique, a Collison type atomizer was also used to generate an aerosol, but of smaller droplet diameter. The precursor solution was delivered as an aerosol which was created using a TSI 3076 constant output Collison type atomizer, using compressed air as the carrier gas. The Collison method was described in chapter 1. This type of aerosol generator produces a constant droplet concentration of $10^7/cm^3$ and a mean droplet diameter of 0.3 μm.[17] These relatively small droplets have a higher surface area to volume ratio and shall be referred to as Collison-AACVD (c-AACVD).

The aerosol solution was prepared using mono-butyl tin chloride (MBTC), 10 g, in methanol (200 ml). trifluoroacetic acid (TFA) served as the fluorine dopant source. Pilkington barrier glass (50 nm layer of SiO_2 coated onto glass) was used as the substrate material to prevent leaching of ionic impurities from the glass. These were cleaned using isopropyl alcohol (IPA) and acetone and allowed to fully air dry prior to use.

The substrate temperature was varied from 350-550 °C along with the molar ratio of F/Sn from 0-50 mol.% in the precursor solution. The substrate temperature and fluorine content were varied in order to optimize the process and form the highest quality films. The deposition time was kept constant at 30 minutes. Both ultrasonic and Collison type aerosol generation were tested under the different growth conditions.

Atmospheric Pressure Chemical Vapour Deposition (APCVD) was also used as a deposition technique for F:SnO_2 thin films in order to allow for comparison with a similar precursor set: MBTC was used as the tin precursor delivered by a heated bubbler (160 °C). A schematic of the APCVD set-up used to grow tin dioxide thin films is shown in figure 33.

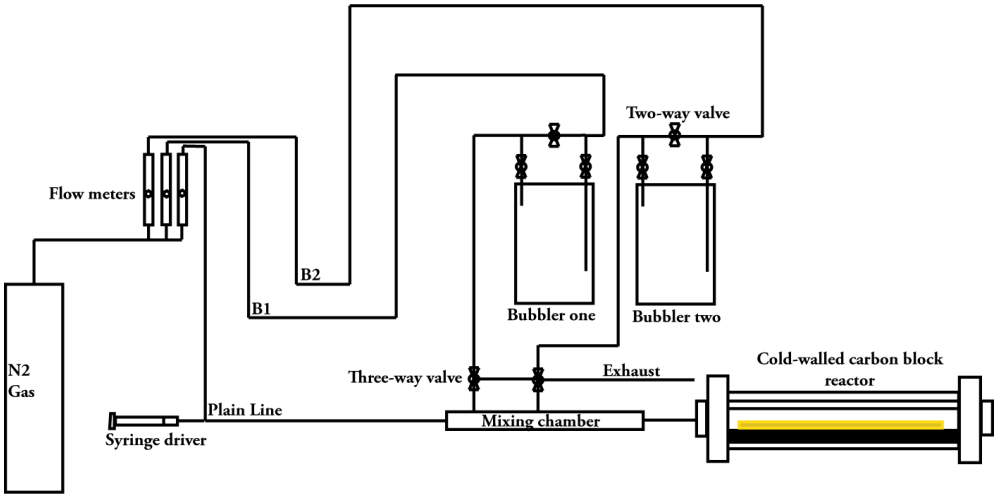

Figure 33: Schematic of the APCVD set-up used to deposit FTO films, where B1 is monobutyltin trichloride, B2 is ethyl acetate and the fluorine source is introduced via the plain line.

Aqueous trifluoroacetic acid was used as the fluorine source delivered by a syringe driver through a heated evaporator (10 vol.% acid, 200 °C) with a plain flow of nitrogen carrier gas. A gas flow of ethyl acetate was used as the oxygen source (60 °C). The deposition was performed in a similar carbon reactor as mentioned previously, with a barrier glass substrate, and over 350- 550 °C. The flow rates and syringe driver speed were varied to optimize the films with regards to sheet resistance.

3.3 RESULTS AND DISCUSSION

Tin dioxide and fluorine doped tin dioxide films were produced over a range of deposition temperatures and concentrations of fluorine in the precursor solution, by using both c-AACVD and u-AACVD, from MBTC and TFA acid in methanol. By varying the fluorine content in solution from 0-50 mol.% the films were appraised in terms of their

sheet resistance. It was found that by changing the fluorine concentration in solution and depositing films at a constant temperature (450 °C) that the sheet resistance dropped to a minimum at ~ 10 mol.% of fluorine in solution which levelled off but then started to increase at ~ 40 mol.% fluorine. Therefore 30 mol.% of fluorine was chosen as the constant amount of dopant in the precursor solution. Films were also produced using an APCVD thermal delivery method from a similar precursor set. These three techniques were chosen to highlight the changes in functional properties afforded by changing the state of the incoming precursor. APCVD uses a stream of molecular gas species reacting on the surface of the substrate for film formation. AACVD utilises an incoming solution based liquid droplet as the transport medium and reacting species. By controlling the droplet size of the aerosol, i.e. using a small droplet size (0.3 μm), generated by a Collison-type atomiser, superior films in terms of opto-electronic properties could be grown. As such the following chapter will focus on the comparison between c-AACVD grown F:SnO_2 to those grown by u-AACVD (large droplet ca 45 μm) and APCVD films deposited in our lab and data recorded from leading commercial products. Figure 34 shows a schematic of the various deposition processes used to grow tin dioxide thin films.

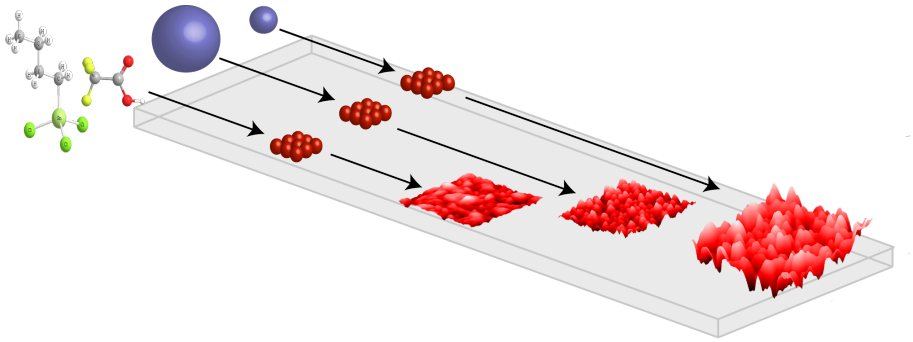

Figure 34: Schematic of the different deposition processes, ranging from APCVD (left) which delivers the reagent to the heated substrate via a molecular gas, u-AACVD (middle) which delivers the reagent via a large aerosol droplet (~ 45 μm) and c-AACVD (right) which delivers the reagent species to the heated substrate for reaction via a small aerosol droplet (~ 0.3 μm). These varying delivery routes affect the growth modes and end properties of the resultant thin films.

3.3.1 *AACVD of FTO Thin Films*

FTO films were produced via AACVD showed high optical transparency (~ 80% across the visible) and film growth rates were recorded between 5-15 nm/min as a function of the deposition temperature. The films were free from pin-hole defects, indicating that the deposition process did not involve any large scale gas-phase nucleation. The films showed good adhesion to the glass substrate passing both the Scotch tape test and steel scalpel scratch test. This is somewhat unusual for AACVD derived films which can tend to be particulate in nature from extensive gas phase reaction. Further, it indicates that the films are likely to be growing from finely attached nucleation points at the surface. Solubility testing of the films was carried out in organic solvent (ethanol and toluene), under basic conditions (2M NaOH) and acidic conditions (2M HCl). The presence of the film on the substrate surface was monitored using electrical resistance measurements as the electrical resistance of plain glass is too high to be measured using a multimeter. The films were suspended in the organic solvents, acid and base showed no change after a period of over one month. The films were stable in air for over six months, showing no change in optical or electrical properties. Films derived from both c-AACVD and u-AACVD gave transparent conducting thin films of F:SnO_2 which produced repeatable properties, including electrical resistance measurements. The c-AACVD produced films gave superior results with a repeatable sheet resistance of 4-5 Ω/sq whilst the u-AACVD process gave films with repeatable values of 90 Ω/sq for films deposited at 500 °C.

3.3.2 *APCVD of FTO Thin Films*

FTO thin films were synthesised by thermal APCVD. The films showed high optical transparency (~ 80% across the visible) and the film growth rate was ~ 1 μm/min as a function of the deposition temperature. The films showed good adhesion to the glass substrate passing both the Scotch tape test and steel scalpel scratch test. Solubility testing of the films was carried out in organic solvent (ethanol and toluene), under basic conditions (2M NaOH) and acidic conditions (2M HCl). The films were screened by their electrical properties mon-

itored using electrical resistance measurements as the electrical resistance of plain glass is too high to be measured using a multimeter.

A series of films were synthesized using MBTC as the tin source, EtOAc as the oxidising agent and trifluoroacetic acid as the dopant source. The precursor ratio was kept constant at 1:20 MBTC: EtOAc along with the deposition temperature at 500 °C. The deposition time was varied independently. Nitrogen (BOC, 99.99%) was used to deliver the precursors to the CVD chamber. The plain line flow was 1.5 L/min, bubbler one (MBTC) was heated to 165 °C and the nitrogen flow kept at 1 L/min and bubbler two (EtOAc) was heated to 62 °C and the nitrogen flow kept at 3 L/min for films produced with varying deposition time. The amount of precursor delivered to the reaction chamber was calculated from a = (VP x F)/((760 - VP) x 24.4), where a is the molar flow rate (mol/min), VP is the pressure of the material at the bubbler temperature (mmHg) and F is the carrier gas flow rate through the bubbler (L/min). The molar flow rates for the precursors corresponds to 7.9 mmol/min for MBTC, 165 mmol/min for ethyl acetate and 0.65 mmol.min for TFA.

The precursors were delivered to the exhaust by passing nitrogen gas through the bubblers and the dopant was introduced via the plain flow line by opening the syringe driver valve, kept at 5 ml/min. Once the flow had stabilised the three-way valve was switched to allow the precursors to enter the mixing chamber for deposition to occur. After the allotted reaction time the three-way valve was switched to the exhaust and the bubblers were closed. The as-deposited films showed no obvious trends with respect to changing the deposition time. A deposition time of 60 seconds produced films of comparable sheet resistance but this parameter proved unreliable as the films varied in sheet resistance from 10 Ω/sq to 250 Ω/sq using identical deposition conditions. Structural characterisation was performed on the films obtained via APCVD. Opto-electronic characterisation however was performed on Pilkington-NSG TEC glass to compare AACVD derived films with commercial products.

3.3.3 *XRD Analysis*

X-ray diffraction patterns of the as-deposited c-AACVD F:SnO_2 films at substrate temperatures ranging from 400-550 °C are presented in figure 35. The films deposited at 350 °C were partially amorphous

and films deposited at higher temperatures were polycrystalline in nature. Furthermore they showed increasing crystallinity with respect to deposition temperature. The diffraction patterns all correspond to the cassiterite structure of tin dioxide. The lattice parameters were computed by fitting a Le Bail model to the patterns using General Structure Analysis System (GSAS).[162,163] Stoichiometric tin dioxide powder has a tetragonal rutile structure and crystallises in the space group $P4_2/mnm$. The cell parameters used for modelling were $a = b = 4.737$ Å and $c = 3.185$ Å. The lattice parameters a and c varied from 4.735-4.749 Å and 3.167-3.205 Å respectively, depending on conditions (Table 1). It was seen from Scherrer width calculationa that the crystallite size increased with deposition temperature.[150]

Substrate T/°C	Crystallite Diameter/nm	a/Å	c/Å	Unit Cell Volume/Å^3
400	10	4.749	3.167	71.43
450	24	4.735	3.185	71.42
500	28	4.737	3.197	71.75
550	26	4.744	3.205	72.14

Table 1: Variation in film thickness, crystallite diameter size and unit cell parameters of F:SnO_2 films deposited by c-AACVD (aerosol droplet size of 0.3 μm) with varying substrate temperature.

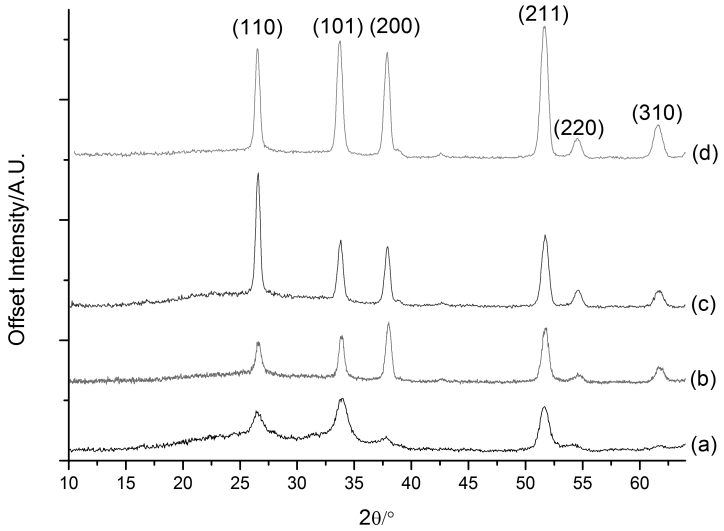

Figure 35: XRD patterns of F:SnO_2 films deposited by c-AACVD (30 mol.% F:Sn in solution) at (a) 400 °C, (b) 450 °C, (c) 500 °C and (d) 550 °C.

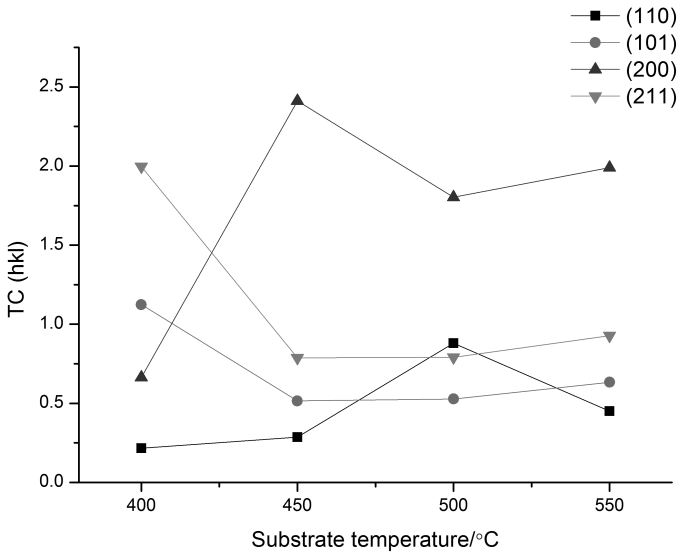

Figure 36: Variation of the texture coefficient (TC) with different temperatures of FTO using c-AACVD (30 mol.% F:Sn in precursor solution).

The preferred orientation of the crystallites in doped tin dioxide films have been reported and correspond to (211), (110), (200) and (301) planes depending on the substrate temperature, film thickness and dopant concentration. Afify *et al*. and Agashe *et al*. reported that the (200) plane is particularly sensitive to substrate temperature which controls the growth of the films.[33,74,91] Belanger *et al*. prepared FTO films by CVD and observed that films with a thickness of c.a. 0.4 μm the dominant planes were found to be the (200), (400), (301) and (211).[91] Belanger *et al*. also found that deep trap levels of grain boundaries surfaces are mostly associated with the (110), (211) and (301) orientations and not with the (200) plane.

The diffraction patterns show that at lower deposition temperature there is an initial broad feature in the diffraction pattern at low 2ϑ, attributed to the amorphous nature of the glass substrate. From the above results it can be seen that the films produced by c-AACVD as a whole showed crystallites preferentially aligned along the (200) plane as calculated from the texture coefficient.[74] The TC(200) calculated at a substrate temperature of 400 °C was found to be 0.66. The intensity of the (200) reflection increased with temperature and TC(200) increased also showing the crystallites preferentially oriented along this plane. This particular plane is predicted to have no deep lying trap levels at grain boundary surfaces correlating to a higher degree

of conductivity across the substrate plane.[91] The calculated TC(200) at a substrate temperature of 450 °C was 2.41, this decreased with substrate temperature as the (110), (101) and (211) reflections increased in prominence.

The XRD patterns for u-AACVD and APCVD derived films are given in figure 37. Cassiterite structured SnO_2 films were synthesised in both cases.

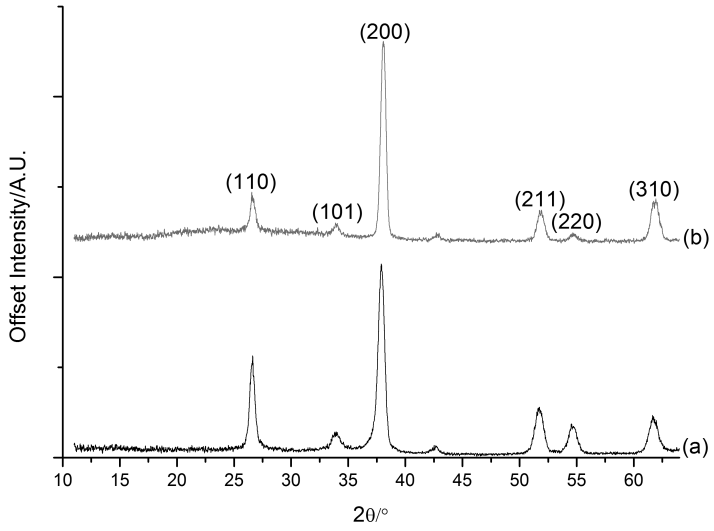

Figure 37: XRD pattern of (a) as deposited F:SnO_2 film by thermal APCVD at substrate temperature of 500 °C (precursor set: MBTC, ethyl acetate and TFA aqueous solution) and (b) as deposited F:SnO_2 film by u-AACVD at substrate temperature of 500 °C (30 mol.% F:Sn in solution).

The degree of preferred orientation with each of the methods was shown to be variable. Each technique shows the crystallites preferentially oriented along the (200) plane, however the APCVD and u-AACVD routes seem to result in a higher degree of surface diffusion at 500 °C with texture coefficient values of 3.21 and 3.22 respectively. The crystallite size was also calculated for both the APCVD and u-AACVD films produced at 500 °C using the Scherrer equation, this gave values of 34 nm and 44 nm respectively. Both show a larger crystallite sizes compared to c-AACVD film at 500 °C. This indicates a greater level of surface reaction leading to larger crystal regions in the polycrystalline films.

3.3.3.1 *Film Morphology*

SEM and AFM were used to study the surface morphology of the F:SnO_2 films. Films deposited at 350 °C were X-ray amorphous which was evident from the XRD data.[93] Figure 38 shows the films deposited by c-AACVD between 400 °C-550 °C which demonstrate a surface structure composed of octahedral particles. The octahedral particles increase in size with the deposition temperature from ca. 100 nm to 400 nm in diameter. This size increase follows the trend given by crystallite size from the XRD patterns, however they are much larger agglomerations. The film grown at 550 °C shows formation of discrete octahedral particles.

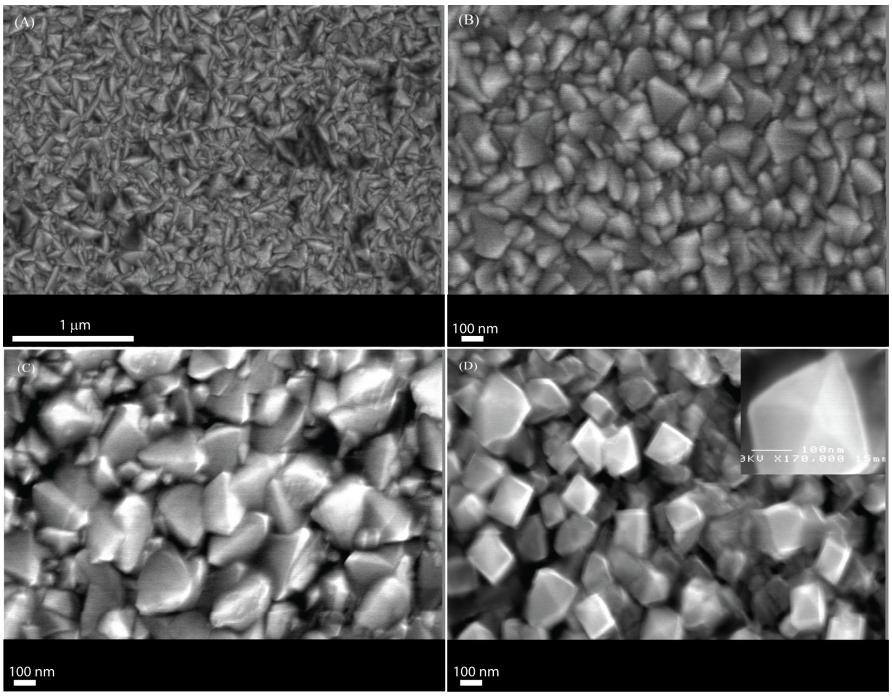

Figure 38: SEM images of F:SnO_2 films deposited by c-AACVD (30 mol.% F:Sn in solution) at (a) 400 °C, (b) 450 °C, (c) 500 °C and (d) 550 °C (inset shows close up particle).

The film morphologies of films produced by u-AACVD and APCVD (figure 39 and 40 respectively) show a noticeable difference compared to films were produced using c-AACVD (figure 38). The particle shape, coverage and roughness all vary in comparison to the c-AACVD method. The films produced by APCVD were smoother than those produced by both AACVD procedures. The SEM images showed void spaces for films produced by APCVD in certain areas as well as poor particle connectivity and coverage compared to films pro-

duced by AACVD, which has a detrimental effect on the conductivity and hence performance of the films. The AFM imaging (Figure 41) demonstrates the 3 dimensional depth profile of a c-AACVD thin film. A hierarchical structure is shown, comprised of the octahedral particles which have formed larger aggregates in the 500 nm range. This larger texturing can be attributed to the c-AACVD delivery process whereby the precursors begin pre-reacting in the aerosol droplets as they approach the heated substrate, owing to the high surface area to volume ratio in the aerosol droplets.[1] The shape and size regime of these larger aggregates is approaching the optimised surface structuring required for light scattering and trapping in thin film solar cells.[71] The optimised surface structure being pyramidal morphology with particles in the size range of 400-700 nm which corresponds to the visible wavelengths of light.

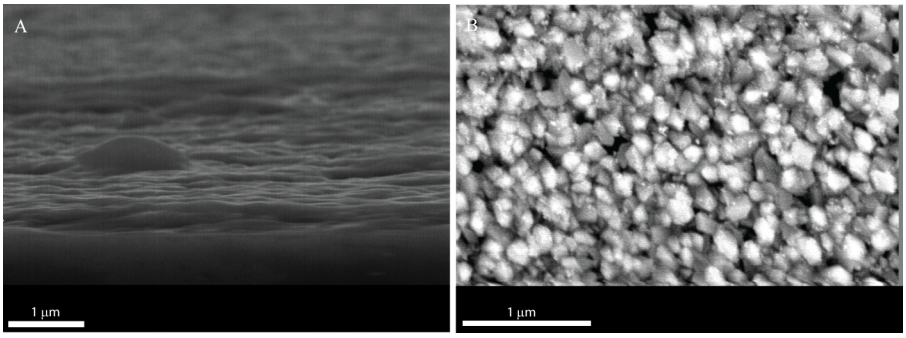

Figure 39: SEM image of F:SnO_2 deposited by u-AACVD (30 mol.% F:Sn in solution) at 500 °C (a) side-on image and (b) top down image.

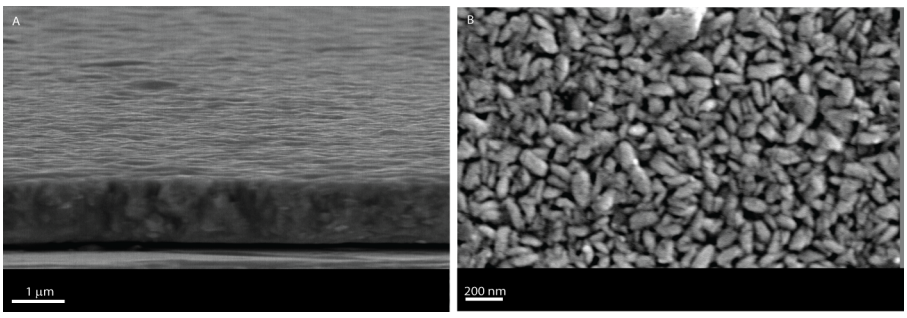

Figure 40: SEM images of F:SnO_2 deposited by APCVD at 500 °C from a monobutyltin trichloride, ethyl acetate and trifluoroacetic acid precursor set (a) side-on image and (b) top down image.

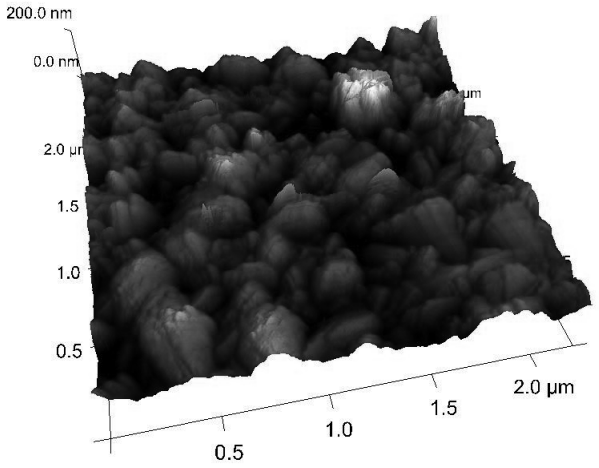

Figure 41: Atomic Force Microscopy image of F:SnO_2 thin film deposited by c-AACVD at 500 °C (30 mol.% F:Sn in precursor solution).

Sample	Substrate T/°C	Roughness (RMS)/nm	Surface Area/μm^2
c-AACVD	500	62.3	6.10
u-AACVD	500	52.2	4.85
APCVD	500	20.7	4.25

Table 2: Comparison of surface roughness and surface area for F:SnO_2 deposited by c-AACVD, u-AACVD and APCVD derived films.

Sample	Average visible light transmission/%	Haze Value (T_{diff}/T_{tot})/%
S3(450°C)	79.4	1.74
S4(500°C)	79.1	7.84
S5(550°C)	80.1	11.42

Table 3: Transmission and Haze values for F:SnO_2 films deposited by c-AACVD at varying substrate temperatures (30 mol.% F:Sn in solution).

Haze measurements were taken in order to determine the ability of the F:SnO_2 films to scatter and trap light. Desirable haze values for use in solar cells are in the 8-15 (T_{diff}/T_{tot}) range. As shown in Table 3 the higher temperature films display a haze value within the correct range. The origin of haze in tin dioxide films with thickness (> 500 nm) is due to the surface roughness of the films and particle sizes which correspond to the wavelengths of visible light. This is

coupled with an average light transmission across the visible of 80% and the desired surface morphology demonstrated by the SEM and AFM imaging.

3.3.3.2 *Electrical Properties*

Hall Effect measurements were conducted on the F:SnO_2 films formed in this work by using the van der Pauw technique in order to determine the electrical properties of the films. These studies showed that F:SnO_2 films produced to be of n-type character. The c-AACVD films gave a minimum stable sheet resistance of 4 Ω/sq. The APCVD derived films and u-AACVD films gave minimum sheet resistances of of 40 Ω/sq and 90 Ω/sq respectively. The incorporation of fluorine is well known to enhance the conductivity of SnO_2. Fluorine doped tin oxide is known to have fluorine incorporated by substitution of oxygen as the ionic radii are comparable, (F^-: 1.17 Å, O^{2-}: 1.22 Å) which results in free electrons in the conduction band. Ramaiah *et al.*[164] reported that the conductivity of heavily doped samples, where (F/Sn molar ratio = 0.15) resulted in decreased conductivity as excess fluorine in the films resulted in the formation of reduced tin species. The effect of deposition temperature on the carrier density, mobility and resistivity is very significant as the conduction mechanisms of F:SnO_2 are highly dependent on the carrier concentration. When the carrier concentration is of the order of 10^{18} cm^{-3} the scattering of the electrons is greatly affected by the grain boundaries. When the carrier concentration is between 10^{18} and 10^{19} cm^{-3} the scattering of the electrons is affected by grain boundaries and bulk properties.[63,84] When the carrier concentration is in excess of 10^{19} cm^{-3} the scattering processes are mainly attributed to bulk properties which screen the grain boundary effects. Also to a first approximation grain boundary conduction mechanisms can be largely ignored if the grain size is much larger than the electron mean free path (~ 10 nm).

Sample	Film thickness/nm	N/cm^{-3}	μ/cm^2(V.s)$^{-1}$	R_{SH}/Ω.sq^{-1}	ρ/Ω.cm
S2 (400 °C)	610	-	-	18	1.1 x 10^{-3}
S3 (450 °C)	680	5.7 x 10^{20}	25	5	2.7 x 10^{-4}
S4 (500 °C)	720	6.4 x 10^{20}	12	4	2.2 x 10^{-4}
S5 (550 °C)	700	8.2 x 10^{19}	9	28	2.0 x 10^{-3}
TEC 8	650	5.3 x 10^{20}	28	8	5.2 x 10^{-4}
TEC 15	350	5.6 x 10^{20}	21	15	5.3 x 10^{-4}
Asahi-U	900	2.2 x 10^{20}	32	9.7	8.8 x 10^{-4}

Table 4: Film thickness, charge carrier density, Hall mobility, sheet resistance and resistivity of F:SnO_2 thin films as a function of deposition temperature produced by c-AACVD (30 mol. % F:Sn in solution) and compared to TEC 8, TEC 15 and Asahi-U produced by Pilkington NSG and Asahi Glass Company respectively.

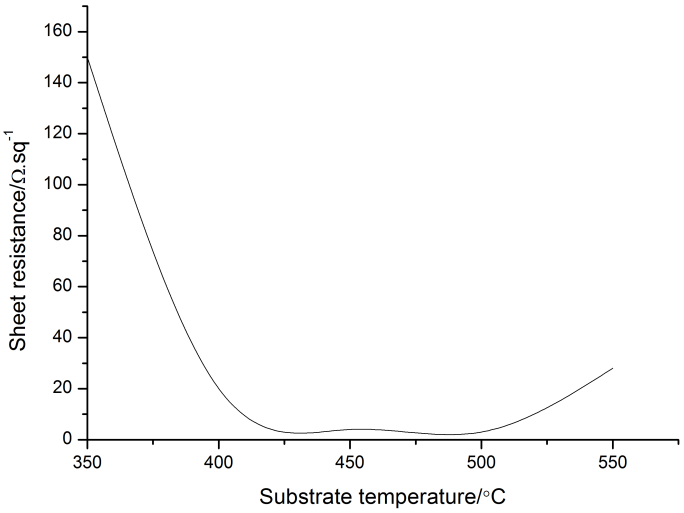

Figure 42: Variation in sheet resistance with deposition temperature of F:SnO_2 thin films produced by c-AACVD (30 mol.% F:Sn in solution).

It can be seen from the data that the sheet resistance decreases with increasing deposition temperature. The crystallinity and crystallite size were noted to increase with deposition temperature up to 500 °C. This indicates that grain boundary resistance effects attributed to smaller crystallites comparable to the electron mean free path are negligible. The sheet resistance increases again with films deposited at 550 °C and from the SEM images it is clear that there is poor connectivity of the particles compared to those deposited at lower temperatures.

The charge carrier density was determined using the van der Pauw technique. Hall effect data could not be obtained for films deposited at 400 °C and the fluorine content could not be determined by WDX analysis. Hall effect data showed that the carrier density increased from 5.7 x 10^{20} cm^{-3} for c-AACVD films formed at a substrate temperature of 450 °C to 6.4 x 10^{20} cm^{-3} for films deposited at 500 °C. The concentration of fluorine for films deposited at 450 °C was 1.6 at.% compared to 2.2 at.% for films deposited at 500 °C as determined from WDX analysis. The decrease in sheet resistance with increasing temperature can be attributed to the increase in charge carrier concentration but the mobility of the charge carriers reduced, possibly due to an increase in the number of defects in the film, hindering the mobility of the electrons. At a substrate temperature of 550 °C the carrier concentration decreased to 8.2 x 10^{19} cm^{-3}, thus tending to more stoichiometric tin dioxide.[84] The fluorine content in the films deposited at 550 °C was ca. 1 at.% supporting the Hall effect data, in which a reduction in the charge carrier concentration was observed. The mobility for films deposited at 500 °C was 12 $cm^2/V.s$ and did not drop significantly for films deposited at 550 °C (9 $cm^2/V.s$) but the sheet resistance did increase from 4 Ω/sq to 28 Ω/sq respectively, which could be attributed to a reduction in the number of charge carriers. It has been shown previously for FTO films that the sheet resistance/bulk resistivity increases with deposition temperature due to a reduction in the carrier concentration as well as the diffusion of alkali ions into the films. The depositions however in our case, were carried out on silica barrier glass, ruling out the possibility of alkali metal diffusion. On a more qualitative note, it was seen from the the SEM images that for films deposited at 550 °C, the formation of discrete particles could be seen resulting in poor connectivity between grains which could impact the electrical properties of the films.

Comparison of the electrical properties of c-AACVD F:SnO_2 films to those produced by thermal APCVD by Pilkington NSG are shown in table 4. The u-AACVD films of F:SnO_2 exhibited a sheet resistance too high (> 90 Ω/sq) for accurate Hall effect measurements. This level of resistance is also too high for any infrared reflectivity. The APCVD derived films gave a minimum sheet resistance of 40 Ω/sq but were deemed too inconsistent to take forward to electrical testing, hence a comparison with commercial APCVD films (TEC 8 and TEC 15) produced by Pilkington NSG was considered appropriate. It can be

seen that the films we have produced by c-AACVD are comparable to those produced by Pilkington NSG in terms of sheet resistance, resistivity and show very similar levels of carrier concentration and electron mobility.

3.3.3.3 *Optical measurements*

The room temperature transmission and reflection characteristics of the F:SnO_2 films produced by c-AACVD were investigated using visible/near IR spectrometry. The spectra shown in figures 43 and 44 were taken using an air background and indicate a high transparency across the visible (~ 80% transmission at 550 nm in air, including the substrate absorbance) and a high reflectivity in the infrared (~ 80% reflection at 2500 nm in air).

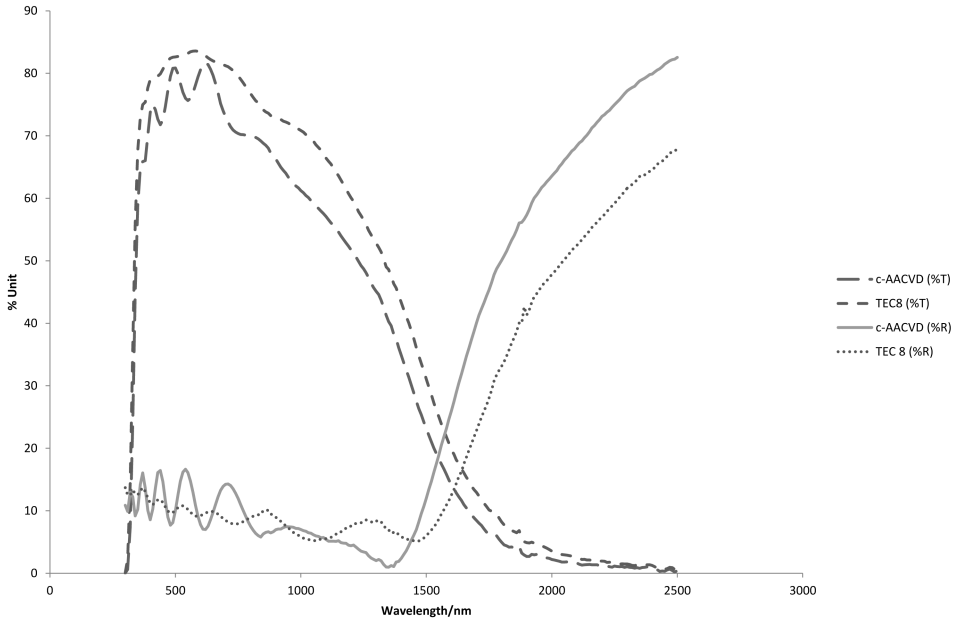

Figure 43: Optical transmittance and reflectance taken with an air background comparing c-AACVD grown F:SnO_2 (450 °C deposition temperature and 30 mol.% F:Sn in solution (5 Ω/sq) and commercial F:SnO_2 (8 Ω/sq Pilkington TEC 8)).

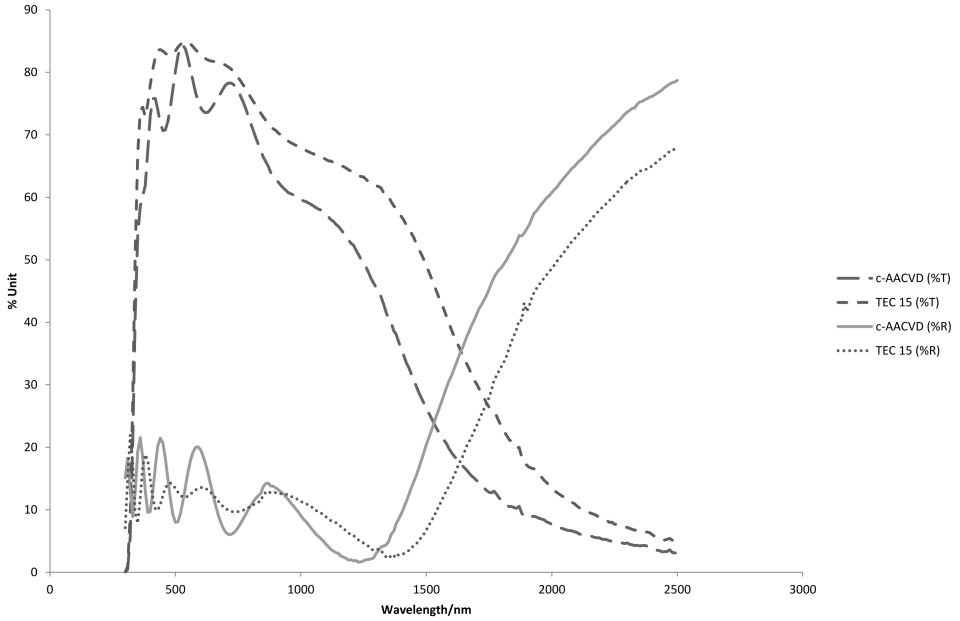

Figure 44: Optical transmittance and reflectance spectra taken with an air background comparing c-AACVD grown F:SnO_2 (400 °C deposition temperature and 30 mol.% F:Sn in solution (18 Ω/sq) and commercial F:SnO_2 (15 Ω/sq Pilkington TEC 15)).

The films display prominent interference effects. These interference fringes are caused by the multiple reflections at the three interfaces of the air/thin film/transparent substrate bi-layer. Included in figures 43 and 44 are plots of spectra taken from leading commercial F:SnO_2 thin films on glass substrates. Pilkington TEC 8 and TEC 15 glass was used as the reference products with a sheet resistance of 8 Ω/sq and 15 Ω/sq respectively as well as resistivities of the same order of magnitude. This allows for comparison of optical properties between our c-AACVD films (400 °C (18 Ω/sq) and 450 °C (5 Ω/sq)) with commercial films of a similar electrical conductivity. The onset of the infrared reflection occurs at the plasma resonance frequency where the electromagnetic radiation incident on the film can induce resonance of the free carriers within the metal oxide matrix. It can be shown that the plasma frequency is dependent upon the conductivity, the di-electric constant and the mean free relaxation time of the material. This means that increasing the charge carrier density and decreasing the charge carrier effective mass (reducing retarding forces on the free electrons, such as scattering defects) will increase the plasma resonance frequency of the TCO, thus shifting the resonance reflection effect to a shorter wavelength. This effect can be

seen in figure 43 and more pronounced in figure 44 where an approximate 200 nm blue shifting of the plasma edge has occurred. The c-AACVD F:SnO_2 films show a rapid onset of the IR reflection and a reflectivity at 2500 nm which is 10-15% higher than the commercial products. It should however be noted that a 2-5% drop in transmission (ignoring the interference pattern) over the visible accompanies the high IR reflectivity, however the commercial coating has a built in anti-reflective layer that improves transmission. Essential properties for low-ε-coatings include a high reflective value for IR radiation (> 2000 nm) and a rapid onset of the plasma edge which separates the transparent and reflective regime across the wavelength range.[71,165] Both of these attributes are present in the films formed in this work and exceed commercially available films.

It has been shown that by changing the precursor delivery method that the functional electronic, crystal and surface texture properties of F:SnO_2 films can be tailored for different applications. Other work has been published using a spray deposition technique to deposit F:SnO_2 films close to 1 μm thick with a sheet resistance of 3.42 Ω/sq, a charge carrier concentration of 25 x 10^{20} cm^{-3} and a mobility of 6.6 cm^2/V.s. Ultra sonic spray pyrolysis has been used to achieve a high charge carrier density of 8 x 10^{20} cm^{-3} and mobility of 20 cm^2/V.s with a transmission across the visible of 77%.[86] These results show similar electrical characteristics to films which have been deposited by c-AACVD, however, we achieve the same performance with a much thinner film. In addition to the excellent electrical performance the c-AACVD films show a surface morphology which can be tailored using the temperature of deposition to suit different applications. A shifting of the plasma edge was also observed for films grown using c-AACVD as a deposition technique. These attributes indicate that c-AACVD can make coatings with superior properties that could be scaled for application in solar cells.

3.4 CVD OF FTO ON POLYMER COATED STEEL

Fluorine doped tin oxide films were synthesized on high temperature resistant polymer coated steel substrates using a variety of CVD techniques for the potential use in dye sensitized solar cells (DSSC) forming the back electrode. Atmospheric pressure chemical vapour deposition (APCVD) and variants of aerosol assisted chemical vapour

deposition (AACVD) were used to prepare films comparable to commercial standards. Films were synthesized by APCVD using MBTC, ethyl acetate and TFA. Films synthesized by AACVD were produced using MBTC, TFA and methanol. This work highlights the rapidity of APCVD compared to AACVD, essential when depositing films on a sensitive polymer substrate, in producing high quality films at a fraction of the time. The films displayed high conductivity (< 10 Ω/sq) as well as the correct morphology to be used as solar cell electrodes.

3.4.1 *APCVD Films on Polymer Substrates*

3.4.1.1 *Reagents and conditions*

The substrates were cleaned using isopropanol and acetone then left to dry in air before being mounted in the CVD chamber. A series of films were synthesized using MBTC as the tin source, EtOAc as the oxidising agent and trifluoroacetic acid as the dopant source. The precursor ratio was kept constant at 1:20 MBTC: EtOAc along with the deposition temperature but the deposition time was varied. Nitrogen (BOC, 99.99%) was used to deliver the precursors to the CVD chamber. The plain line flow was 1.5 L/min, bubbler one (MBTC) was heated to 165 °C and the nitrogen flow kept at 1 L/min and bubbler two (EtOAc) was heated to 62 °C and the nitrogen flow kept at 3 L/min for films produced with varying deposition time. The amount of precursor delivered to the reaction chamber was calculated from a = (VP x F)/((760 - VP) x 24.4), where a is the molar flow rate (mol/min), VP is the pressure of the material at the bubbler temperature (mmHg) and F is the carrier gas flow rate through the bubbler (L/min). The molar flow rates for the precursors were identical to the APCVD films deposited on glass substrates. The precursors were delivered to the exhaust by passing nitrogen gas through the bubblers and the dopant was introduced via the plain flow line by opening the syringe driver valve, kept at 5 ml/min. Once the flow had stabilised the three-way valve was switched to allow the precursors to enter the mixing chamber for deposition to occur. After the allotted reaction time the three-way valve was switched to the exhaust and the bubblers were closed. The reactor was switched off and the substrate was allowed to cool under a flow of nitrogen gas and taken out of the reactor below 150 °C.

3.4.2 *Results and Discussion*

3.4.2.1 *X-ray Diffraction*

X-ray diffraction patterns for the as-deposited fluorine doped tin dioxide thin films on polymer coated substrates with varying deposition time were recorded. The films with shorter deposition times were partially amorphous in nature and with increasing deposition time (> 30 seconds) the films were polycrystalline. The diffraction patterns recorded corresponded to the cassiterite structure of tin dioxide. The peaks were indexed to the bulk powder pattern of tin dioxide obtained from ICSD-16635, which can be seem clearly from 45(a). There also appears to be a small amount of impurity as peaks at 24° and 31° (2ϑ) were also recorded which could be attributed to β-SnO. Peaks at 44°, 65° and 83° (2ϑ) are due to the underlying electro-chrome coated steel (ECCS) substrate. The (112) reflection expected at 64° (2ϑ) is more than likely to be a convolution of the ECCS reflection which occurs at 64° (2ϑ) as is the (222) reflection at 83° (2ϑ) which is also coupled with the ECCS peak at 82° (2ϑ). The most intense peak was the (211) plane, which has been reported to be a crystallographic plane associated with deep lying traps but as the particle size is larger than the electron mean free path the scattering by grain boundaries becomes negligible. The enhanced conductivity even with this crystollgraphic plane as the most intense could also be an indication of the concentration of free electrons in the films, indicating a high concentration of free carriers. When $N > 10^{19}$ cm^{-3} the conductivity can be attributed to the bulk of the film with nearly free electron (homogeneous) conduction and is not limited to temperature mediated hopping mechanisms as would be the case if grain boundary scattering was to be a governing factor. The particle size increased with deposition time, as expected due to the greater amount of reactants delivered to the reaction chamber, which can also be seen on the SEM images where the particle size increases with deposition time.

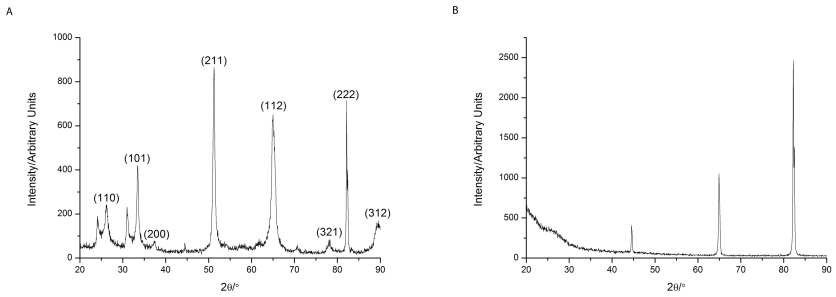

Figure 45: X-Ray Diffraction pattern of (a) F:SnO_2 film deposited on PI/ECCS from the APCVD reaction of monobutyltin trichloride with ethyl acetate and trifluoroacetic acid for 40 seconds and (b) PI/ECCS substrate indicating peaks arising from iron in steel.

3.4.2.2 *Raman Spectroscopy*

Raman spectroscopy was performed in order to provide additional information to the XRD data on the presence of tin oxide and it can be used to distinguish between SnO and SnO_2 but as tin dioxide thin films are low volume Raman scatterers obtaining good data is difficult. Tin dioxide, which contains 6 unit cell atoms, has 18 vibrational modes. Group theory gives these as:

$$\Gamma = A_{1g} + A_{2g} + B_{1g} + B_{2g} + E_g + 2A_{2u} + 2B_{1u} + 4E_u \tag{56}$$

Of these 18 modes, four are Raman active (three non-degenerate modes, A_{1g}, B_{1g}, B_{2g}) and the doubly degenerate E_g. Two are silent (A_{2g} and B_{1u}). In the Raman active modes, the oxygen atoms vibrate while the Sn atoms are at rest. The non-degenerate modes vibrate in the plane perpendicular to the c-axis while the doubly degenerate mode vibrates in the direction of the c-axis, with all six oxygen atoms of the octahedral participating in the vibration. From the spectra shown in figure 46, it can be seen that due to the fluorescence of the polymer under the action of laser light the large number of counts recorded can mainly be attributed to laser light and not Raman light. As a direct consequence of this, bands expected to be detected are washed out. Any bands arising from the substrate are also not identified. To determine the Raman active vibrations, bulk tin oxide powder (Tin(IV) oxide; Sigma Aldrich, -325 mesh, 99.9 %) was placed upon float glass and used as a reference as can be seen from figure 46(a). The A_{1g} mode (totally symmetric) is readily identified as it is the most intense peak, followed by the B_{2g}.

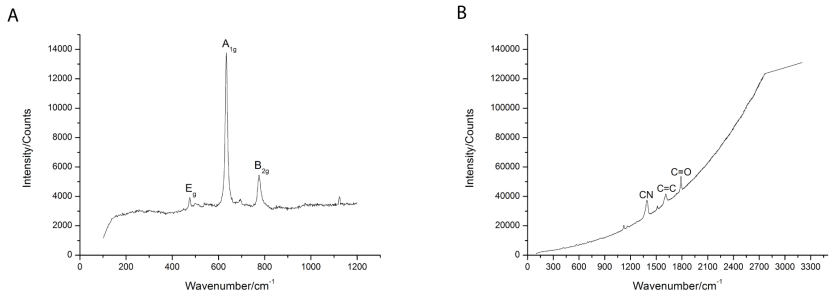

Figure 46: Raman patterns of (a) bulk tin dioxide powder and (b) F:SnO_2 film grown by the APCVD reaction of monobutyltin trichloride with ethyl acetate and trifluoroacetic acid for 40 seconds on a PI/ECCS substrate.

The doubly degenerate mode E_g is more difficult to see especially as a thin film. The peak at 1100 cm^{-1} in the reference spectrum is attributed to the float glass substrate and is known as the silicate peak, corresponding to a SiO_4 tetrahedron connected to a single non-bridged oxygen. The laser power was set to 10 %. Figure 46(b) shows the spectrum recorded for FTO on PI coated ECCS which shows C=C, C-N and C=O vibrations attributed to the polymer. It is clear that any peaks relating to the tin oxide are being masked by the fluorescence of the substrate.

3.4.2.3 *Film Morphology*

The films produced by APCVD were optically transparent, showed interference fringes along the length of the substrate and were chemically bound to the polymer surface passing the Scotch tape test. The colour of the underlying polymer substrate was noted to have turned slightly darker over the course of the deposition as a result of heating. The film thickness was determined by side on SEM images and was found to be 1 μm for a 60 second deposition.

Deposition time /s	MBTC flow rate/ $l.min^{-1}$:bubbler temp/°C	EtOAc flow rate/ $l.min^{-1}$:bubbler temp/°C	Reactor temp/ °C	Gas phase MBTC: EtOAc ratio	R_{SH}/ $\Omega.sq^{-1}$
10	1:165	3:62	500	1:20	80
30	1:165	3:62	500	1:20	40
40	1:165	3:62	500	1:20	10
60	1:165	3:62	500	1:20	20

Table 5: Conditions used to grow F:SnO_2 thin films from the APCVD reaction of monobutyltin trichloride with ethyl acetate and trifluoroacetic acid dissolved in water and the resulting sheet resistance values of the obtained films.

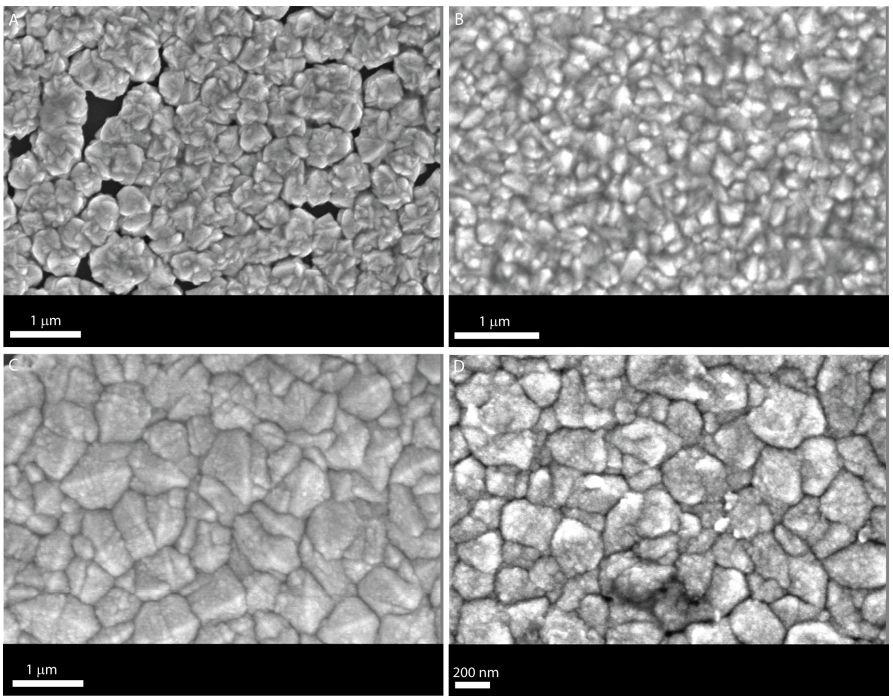

Figure 47: Top down SEM images of F:SnO_2 thin films deposited by the APCVD reaction of monobutyltin trichloride with ethyl acetate and trifluoroacetic acid for (a) 10 s, (b) 30 s, (c) 40 s and (d) 60 s.

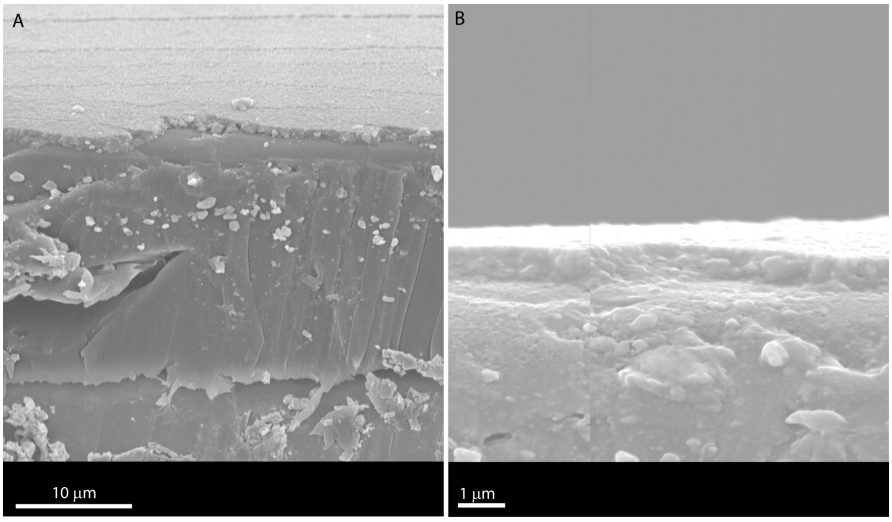

Figure 48: Side on SEM images of F:SnO_2 thin films deposited by the APCVD reaction of monobutyltin trichloride with ethyl acetate and trifluoroacetic acid with a deposition time of 40 seconds (a) 30° tilt and (b) 0° tilt.

Scanning electron microscopy (secondary electron) was used to study the surface morphology of the FTO films. The films with a deposition time of 10 seconds showed incomplete substrate coverage, as cracks and voids could be seen from the SEM images. The particles were sharp and appeared pyramidal in nature but were poorly connected, which can be attributed to the deposition time. As the deposition time increased the greater packing and connectivity of the particles became evident with little to no voids apparent from the SEM images. Films deposited for 40 seconds, figure 47(c), showed larger particles from the SEM images comapred to those of shorter deposition time, around 500 nm in diameter. The thickness of the films (figure 48) deposited for 40 seconds was found to be around 800 nm and the distinctive layers of ECCS, a 24 μm polymer layer and tin oxide could be seen very clearly.

3.4.2.4 *Electrical Properties*

The doped tin dioxide films exhibited n-type conductivity with a minimum stable sheet resistance of 10 Ω/sq. The incorporation of fluorine greatly enhances the conductivity. The fluorine doping level was kept constant for each deposition and was controlled by the amount forced through by the syringe driver. Films deposited for 10 seconds, the R_{SH}= 80 Ω/sq and this decreases with deposition time to 40 Ω/sq for a 30 second deposition. The fluorine content was determined at ca. 0.7

at.% for these films by WDX analysis. Films deposited for 40 seconds showed a mininum sheet resistance of 10 Ω/sq and a corresponding fluorine content of 1.8 at.%.

This value increases slightly to 20 Ω/sq for a 60 second deposition with a fluorine content of 1 at.%. This could be attributed to a slight blockage at the inlet as the substrate showed incomplete coverage. It can be seen from the SEM images that as the deposition time increases, the films appear to become more densely packed with fewer cracks and voids and as a result of better connectivity between the particles as well as increasing particle/grain size the resistance encountered by the electrons to the flow of current is reduced. Hall effect could not be used on steel substrates and electrical data was obtained using the linear 4-point-probe technique described in chapter 1.

3.4.3 *AACVD Films on Polymer Substrates*

3.4.3.1 *Reagents and conditions*

The precursor solution was prepared by dissolving MBTC (10 g) and TFA (0.3 g) in methanol (200 ml) and placed into the Collison atomiser. The polymer coated ECCS sheets were cleaned with IPA and acetone and placed into the cold walled CVD reactor at the desired temperature and then the precursor solution was passed through with the compressed air pressure at 2 bar.

3.4.4 *Results and Discussion*

The films produced by AACVD were optically transparent showed interference fringes along the length of the substrate and were chemically bound to the polymer surface passing the Scotch tape test. The films were completely free from pin-hole defects, indicating that the deposition process did not involve any large scale gas-phase nucleation.

3.4.4.1 *X-Ray Diffraction*

X-ray diffraction patterns for the deposited fluorine doped tin dioxide thin films with varying deposition time were collected. The diffraction patterns recorded corresponded to the cassiterite structure of tin

dioxide. It can be seen from figure 49 that for AACVD derived films the (200) reflection is present compared to APCVD derived films with no impurities attributed to SnO phase.

The most intense reflection recorded were the (222) and (112) at 64° and 82°(2ϑ). As found with the APCVD derived films these two reflections are most probably a convolution of the underlying substrate peaks coupled with tin dioxide reflections.

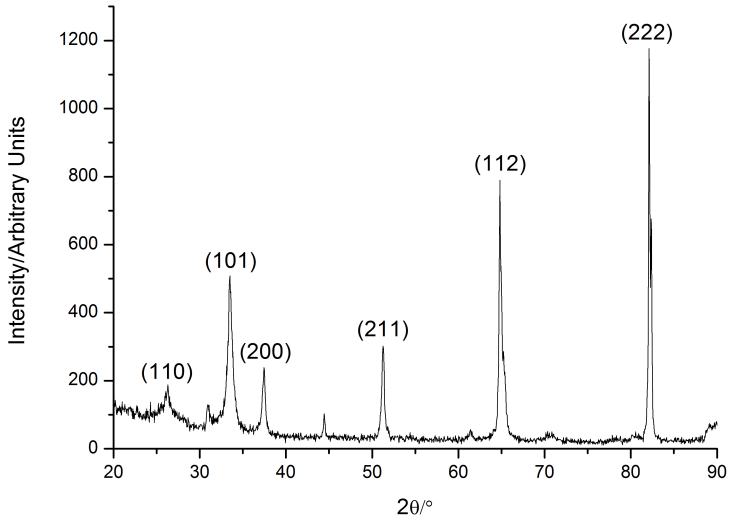

Figure 49: XRD pattern for F:SnO_2 film grown by the AACVD reaction (30 minutes) of monobutyltin trichloride with methanol and trifluoroacetic acid at 500 °C.

3.4.4.2 *Raman Spectroscopy*

Raman spectroscopy was once again performed in order to provide additional information to the XRD data but as mentioned for APCVD films, any peaks corresponding to tin dioxide were not seen. The pattern recorded shows very high fluorescence as seen with APCVD derived films as a result of the polymer substrate.

3.4.4.3 *Film Morphology*

Scanning electron microscopy (secondary electron) was used to study the surface morphology of the FTO films. The films with a deposition time of 10 minutes showed incomplete substrate coverage, and appeared to be thinner in comparison to APCVD derived films and films deposited for 15 minutes or more.

Deposition time/ min	F:Sn molar ratio	Methanol volume/ml	Reactor temp/ °C	R_{SH}/ $\Omega.sq^{-1}$
10	1:3.3	200	500	70
15	1:3.3	200	500	12
20	1:3.3	200	500	15
30	1:3.3	200	500	10

Table 6: Conditions used to grow F:SnO_2 thin films from the AACVD reaction of monobutyltin trichloride with methanol and trifluoroacetic acid and the resulting sheet resistance values for the films obtained.

Cracks and voids were evident and focusing on the surface was difficult as can be seen in figure 50(a). The nucleation of the particles is evident though from the images but the features are not defined for films deposited for a shorter time. As the deposition time increased to 15 minutes the amount of precursor entering the reaction chamber is increased and it is clear from the images that surface features, such as pyramidal particles, can be identified and the films appear more dense and better connected than those deposited at shorter run times. The images obtained for films deposited at 20 minutes however are not consistent and this could be due to the fact that the area chosen to analyse did not exhibit optimum conductivity for the given deposition time and the features appeared to be star/needle like, perhaps the phase before the denser films seen for depositions carried out for 30 minutes. Films deposited for 30 minutes were dense and well packed, with sharp pyramidal features leading on from those deposited for 15 minutes and exhibited microstructure comparable to APCVD derived films.

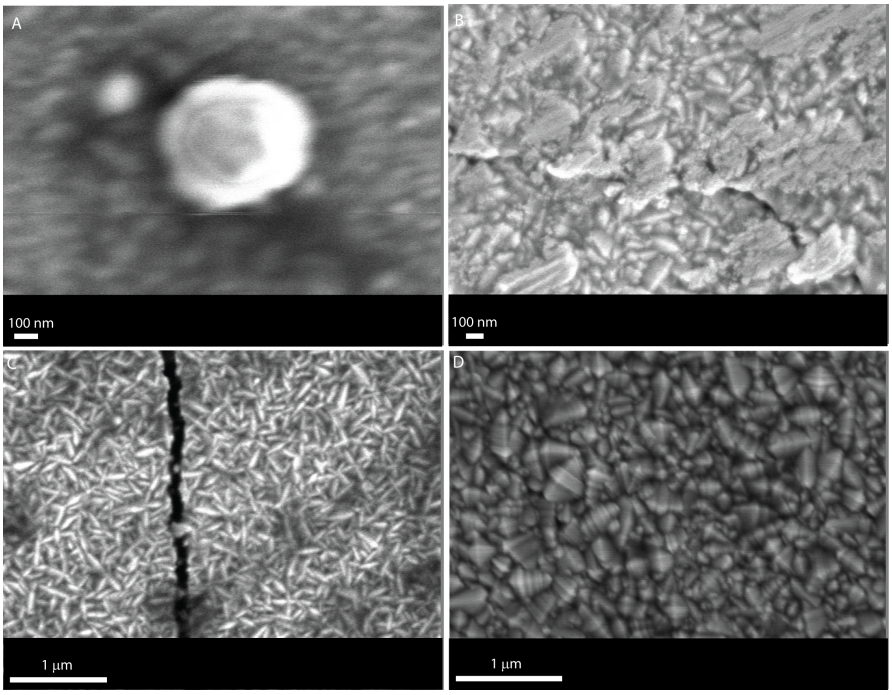

Figure 50: Top down SEM images of F:SnO_2 thin films grown by the the AACVD reaction of monobutyltin trichloride with methanol and trifluoroacetic acid at 500 °C for (a) 10 minutes, (b) 15 minutes, (c) 20 minutes and (d) 30 minutes.

3.4.4.4 *Electrical Properties*

The doped tin dioxide films once again exhibited n-type conductivity with a minimum stable sheet resistance of 10 Ω/sq. The incorporation of fluorine greatly enhances the conductivity. The fluorine:tin molar ratio was kept at 1:3.3. Films deposited for 10 minutes, the R_{SH}= 70 Ω/sq and had a corresponding fluorine content of ca. 0.8 at.% from WDX analysis. The sheet resistance decreased down to 12 Ω/sq for a 15 minute deposition. This decrease in electrical resistance is evident in conjunction with the SEM images as the film appears to be thicker and more dense with better connected particles compared to films derived from 10 minute depositions.

This value increases slightly to 15 Ω/sq for a 20 minute deposition and then once again decreases to 10 Ω/sq for a 30 minute deposition. The fluorine content varied from 1-1.5 at.% for films deposited for longer deposition times as determined from WDX analysis. In conjunction with the SEM images the increase in conductivity can be explained qualitatively however information on the number of free

carriers and mobility etc is not known to get a greater insight to link these different parameters.

3.5 CONCLUSIONS

c-AACVD was shown to be a more effective and simple method for the deposition of fluorine doped tin dioxide films with excellent optical and electrical properties over films produced by APCVD, as well as films produced by u-AACVD. This chapter demonstrates that the deposition process using a Collison type atomizer over an ultrasonic type or APCVD, resulted in the best coatings in terms of reproducibility. The c-AACVD method is advantageous over the u-AACVD method due to the fact that the droplets generated by this method are significantly smaller in diameter than those generated by an ultrasonic humidifier. This could result in shorter evaporation times of the solvent, complete solute precipitation, with a droplet size similar to the grains as seen by SEM. Control over the carrier mobility, charge carrier density, IR reflectance, crystallinity and the surface morphology of the films have shown to be highly dependent upon deposition temperature using this technique. This work demonstrates a move towards tailoring functional properties of the films to specific applications, including transparent conducting materials for thin film photovoltaics, polymer devices and architectural glazing. Deposition temperatures of 450 °C for c-AACVD grown F:SnO_2 thin films were found to be optimum for use as low-emissivity coatings with a low visible light haze value (1.74%), a high charge carrier mobility (25 $cm^2/V.s$), high charge carrier density (5.7 x 10^{20} cm^{-3}), high transmittance across the visible (~ 80%) and a high reflectance in the IR (80% at 2500 nm). A deposition temperature of 500 °C was found to be optimum for the production of c-AACVD grown F:SnO_2 thin films for use as top electrodes in thin film photovoltaics giving a low sheet resistance (4 Ω/sq) and a surface texturing on the micrometer scale with a haze value of 8% for light scattering and trapping within thin film photovoltaic devices.

It has also been shown that AACVD and APCVD can be used to deposit highly conducting doped tin oxide films on polymer coated steel. APCVD has been developed to produce coatings with conductivities comparable to those of c-AACVD but at a fraction of the time as required by industry specifications of the layer properties.

The surface morphology of the coatings produced by each method however may affect the performance in their role as a back contact for DSSCs. The AACVD derived films showed sheet resistance values comparable to the APCVD derived films but the length of deposition was much longer. The polymer appeared not to be denatured by the length of the deposition. It would be beneficial to test the performance of the metal oxide coatings on the on-line furnace to test if they can survive a titania sintering phase for DSSC production. This work shows that either APCVD or even AACVD is a facile route to producing electrically conductive thin films of fluorine doped tin dioxide for the potential use as electrodes in DSSCs.

The next chapter deals with the synthesis and characterisation of zinc oxide thin films. Zinc oxide thin films have been a promising alternative to ITO and FTO thin films in terms of optical properties, electrical properties and stability especially when doped. Undoped zinc oxide films are of little interest as the films are unstable at high temperatures. The next chapter discusses the optical and electrical properties of zinc oxide, fluorine doped zinc oxide and aluminium doped zinc oxide as stable alternatives to commercially available TCO products.

Chapter IV

ZINC OXIDE FILMS

4

TRANSPARENT CONDUCTIVE ZINC OXIDE FILMS BY AACVD

The following chapter presents the results from a series of experiments for growing conductive and transparent ZnO and doped ZnO films via a dual source AACVD route. ZnO films in general were synthesized by the reaction of diethyl zinc (in toluene) with methanol by dual source aerosol assisted chemical vapour deposition. These films exhibited electrical and optical properties comparable to commercial transparent conducting oxides (TCOs) based on oxides of tin or indium. The enhanced electrical properties of these films could possibly be explained by the high solubility of hydrogen in the zinc oxide structure, which serves as an n-type dopant, as shown by computational groups. Doping the zinc oxide structure with fluorine resulted in films with improved electrical properties compared to plain ZnO as well as showing idealised surface texturing for photovoltaic applications. The process was not only limited to anionic dopants but cationic dopants such as aluminium could also be incorporated into the zinc oxide structure also.

4.1 INTRODUCTION

Transparent conducting oxides (TCOs) have been discussed in chapters 1 and 3 and are materials which combine optical transparency with electrical conductivity. In order for materials to be transparent they must display a band gap greater than the highest frequency of visible light (3.1 eV).[98,166] Metals for instance are highly conductive but do not transmit visible light and transparent materials such as glasses are insulators.[87,167] TCOs exhibit intrinsic conductivity due to defect states in the crystal structure.[34,168] By extrinsic doping with aliovalent elements the conductivity of TCOs can be improved. The introduction of impurities into the crystal structure results in donor states near the conduction band if the conductivity is n-type or acceptor states near the valence band if the conductivity is of p-type character.[63] An important requirement in doping is that these states

must be shallow in order to maintain optical transparency.[71] These materials underpin the photovoltaic industry by providing the transparent electrodes for thin film amorphous silicon solar cells, dye sensitized solar cells (DSSC), flat panel displays in polymer light emitting devices.[30,55,56,60] TCO materials are generally limited to materials that show n-type conductivity such as In_2O_3, SnO_2 and ZnO although some p-type materials are known such as $CuAlO_2$, $SrCu_2O_2$ and NiO.[169] For practical applications in devices ranging from solar cell electrodes to light emitting diodes a TCO must have a resistivity of less than 10^{-3} Ω.cm and over 80% transmittance in the visible region.

A key requirement for advances in TCO technology will be to reduce resistivity with no deleterious effects to the optical properties over the visible region. Low resistivity is achieved through very high levels of doping with concentrations in excess of 1×10^{20} cm^{-3}. This can then result in high free carrier absorption and high plasma resonance reflectivity, resulting in poor transmission. This may look bleak but there is the potential for improvements in electrical conduction while maintaining the optical transmission through increasing the carrier mobility. This will be achieved through improving the microstructure of the films, reducing "killer" defect concentrations and reducing impurity scattering centres. The materials challenge for increasing the TCO grain size, while reducing point defect concentration is complicated however by the need for high temperature for the former and low temperature deposition for the latter. An additional major area for TCO performance improvement for PV applications is in interfacial properties. These physical (e.g. surface roughness/topography), optical (optical scatter) and electronic properties (losses at interfaces) at the TCO borders are critical for optimising performance. For example a controlled degree of scattering is essential for optimising efficiency and this level should vary with wavelength according to PV material employed.

The current most used TCO is tin doped indium oxide (ITO).[14,23] Due to the scarcity and cost of indium alternatives need to be found. Fluorine doped tin oxide (FTO) is emerging as a replacement to ITO with electrical properties approaching that of ITO with high transmittance as has been discussed in chapter 3.[48,170,171] Zinc oxide films have received much attention to replace ITO as the industrial standard. With consideration of the environment, ZnO is a promising alterna-

tive because zinc is relatively inexpensive, abundant, relatively non-toxic and can exhibit electrical properties comparable to ITO.[27,49,172–174] The source of intrinsic n-type conductivity in plain zinc oxide is a controversial topic. Computational studies have shown that native defects are not high concentration shallow donors. Vacancies however were found to have sufficiently low formation energies but zinc and oxygen vacancies are deep acceptors and donors respectively. The n-type conductivity was attributed to unintentional doping of hydrogen. The mechanism for this is the propensity of hydrogen to bond to oxygen and thus be incorporated into the crystal structure. The resulting O-H bond is much like doping with fluorine. The studies showed that H^+ is the most stable charge state for all Fermi level positions calculated and the formation energy low enough to allow for a large solubility of hydrogen in n-type ZnO.[34,175] This chapter investigates the use of Aerosol Assisted Chemical Vapour Deposition (AACVD) of ZnO, F:ZnO and Al:ZnO thin films as a low cost, scalable alternative to traditional deposition techniques such as APCVD, dc/rf sputtering, sol-gel and spray pyrolysis.[1,75,161,176] This work shows that AACVD gives control over the electrical and crystal properties of the films. The structural and optical properties play a major role in determining efficiency and practicality of use. Fully characterising and understanding these relationships via AACVD would be beneficial. This is because the current routes to these materials by PVD processes produce poor crystallinity, due to low substrate temperatures and unwanted plasma erosion as the films grow. There have been PVD routes to reduce the impact and improve crystallinity by sputtering onto hot substrates. The number of grain boundaries, quality of crystal structure and the interfaces are problematic. We report that by combining aerosols of diethyl zinc and methanol we have formed zinc oxide films with electrical conductivity and optical transparency comparable to the best extrinsically doped zinc oxide but also to commercial products based on SnO_2 and In_2O_3. By intentionally adding fluorine and aluminium as extrinsic dopants the opto-electronic properties were further enhanced.

4.2 EXPERIMENTAL

Depositions were carried out under nitrogen (99.99% from BOC). Precursors were placed in a glass bubbler and an aerosol mist was cre-

ated using a piezo electric device. $ZnEt_2$ (1.1 M in toluene) and $AlMe_3$ (2.0 M in toluene) were procured from Aldrich and were utilised as bought. $C_6H_5CF_3$ was also procured from Aldrich and treated with CaH_2, distilled, degassed, and stored over molecular sieves. ZnO films were synthesized by transferring dry toluene (15 ml) to $ZnEt_2$ solution (15 ml) in a bubbler. Dry methanol (45 ml) was transferred to a separate bubbler. These were then atomized. The metal precursor flow was kept at 0.6 l/min and the alcohol flow was kept at 0.6 l/min. The two aerosol flows were then mixed at a Y-junction and then delivered to the heated glass substrate (Fig. 51). The substrate temperature was kept at 450 °C. Deposition time was 90 minutes. After the deposition the bubblers were closed and the substrates were cooled under a flow of nitrogen. Fluorine doped zinc oxide films were prepared by adding $C_6H_5CF_3$ (15 ml) to $ZnEt_2$ solution (15 ml).

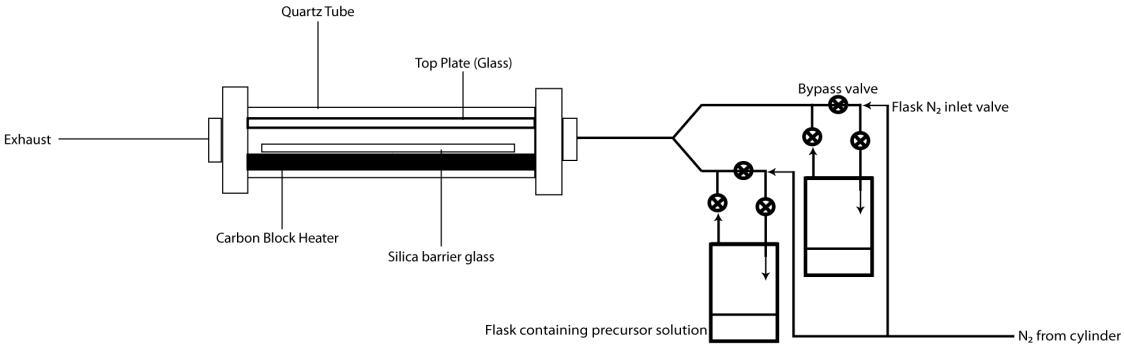

Figure 51: Schematic of dual source AACVD apparatus used for deposition of ZnO films.

Aluminium doped zinc oxide films were prepared by transferring dry toluene (15 ml) to $ZnEt_2$ solution (15 ml) and adding $AlMe_3$ solution (2 ml) to the bubbler. These were then atomized as mentioned above. At the end of the deposition the nitrogen flow through the aerosol was diverted and only nitrogen passed over the substrate. The glass substrate was allowed to cool with the graphite block to less than 100 °C before it was removed. Coated substrates were handled and stored in air. The coated glass substrate was cut into ca. 1 cm × 1 cm squares for subsequent analysis. The glass substrate was SiO_2, precoated (ca. 50 nm thick SiO_2 barrier layer) standard float glass (NSG) 15 cm × 4 cm × 0.3 cm. A top plate was suspended 0.5 cm above the glass substrate to ensure a laminar flow.

X-ray diffraction (XRD) was used to analyse the samples in a Bruker D4 Endeavour X-ray diffractometer (theta/2theta mode) with $CuK\alpha_1$

and CuKα_2 radiation of wavelengths 1.54056 Å and 1.54439 Å respectively, emitted with an intensity ratio of 2:1, a voltage of 40 kV and current of 30 mA. The angular range of the patterns collected was 10° < 2ϑ < 70°. A step size of 0.05° was used, with 1200 steps at 8s/step corresponding to a scan time of 3 hours. Le Bail models were fitted to the collected data using General Structure Analysis System (GSAS) and EXPGUI suite in order to determine the unit cell parameters and crystallite size from the Lorentzian broadening term.[162,163]

Scanning Electron Microscopy (SEM) was performed to determine surface morphology and film thickness using a JEOL JSM-6301F Field Emission SEM at an accelerating voltage of 4-5 keV.

Wavelength dispersive X-ray spectroscopy (WDX) was used to quantify the atomic percentage of F, Al and Zn using a Phillips ESEM at an accelerating voltage of 10 kV. The standards used for Zn, F and Al were metallic zinc, Na_3AlF_6 and Al_2O_3 respectively. The oxygen concentration was not determined due to interference from the substrate.

Atomic Force Microscopy (AFM) analysis was performed using a Veeco Dimension 3100 in contact mode, where a cantilever with an attached tip scans the surface of the sample to determine the surface topography.

UV/Visible/near IR spectra were taken using a Perkin Elmer Fourier transform Lambda 950 UV/Vis spectrometer over a wavelength range of 300 nm to 2500 nm in both transmission and reflection modes. The transmission spectra background was taken against an air background.

Hall effect measurements were carried out using the van Der Pauw method to determine the sheet resistance, free carrier concentration (N) and mobility (μ).[69] A square array of ohmic contacts arranged on 1 cm² samples were then subjected to an input current of 1 mA and a calibrated magnetic field of 0.58 T. The transverse voltage was then measured. The measurement was repeated by reversing the direction of the magnetic field and the current. The magnitudes of the measured voltages were similar but with opposite signs indicating that the hysteresis was negligible. The Hall coefficient R_H was calculated from transverse voltage, dc current injected, the magnetic field and the film thickness.

Zn K-edge XAS measurements were carried out at beam-line (I18) at the UK synchrotron, Diamond, which operates at 3 GeV and 300 mA. The beam line is equipped with Si(111) monochromator and 27

mm period undulator, ion chambers for measuring incident and transmitted beam intensity and a 4 element Si drift fluorescence detector for measurement in fluorescence mode. All the measurements were carried out in fluorescence mode and typically 6 scans were averaged to produce the spectra. X-ray absorption spectra were processed using ATHENA [158] software and subsequent analysis of the EXAFS data were performed using ARTEMIS. [158]

4.3 RESULTS AND DISCUSSION

Highly transparent and conductive zinc oxide films and doped analogues were deposited on silica coated float glass by the AACVD reaction of diethylzinc solution (in toluene) and methanol. The electrical properties combined with the optical properties were better than any previous plain zinc oxide films reported. The reaction presumably proceeded via in-situ generation of the organozinc alkoxides (RZnOR') as intermediates. [173,177] Fluorine doped and aluminium doped zinc oxide films were also deposited by adding trifluorotoluene and trimethylaluminium solution (in toluene) as the dopant sources. The AACVD reactions for each system were carried out at 450 °C.

Element	Plain Glass	ZnO	F:ZnO	Al:ZnO
Si/at.%	30	0.6	0.8	0.4
O/at.%	70	50.3	53.7	49.6
Zn/at.%	-	49.1	43.4	45.8
F/at.%	-	-	2.1	-
Al/at.%	-	-	-	4.2

Table 7: Chemical composition of ZnO, F:ZnO and Al:ZnO films grown on glass by the dual source AACVD reaction of diethyl zinc with methanol at 450 °C determined from WDX analysis.

The films deposited were uniform, showed excellent coverage across the glass substrates and were adherent, passing the Scotch tape test. In order to determine the chemcial composition of the films, WDX analysis was carried out, using standards mentioned in the experimental, on all the samples to establish the presence of dopants within the system as shown in table 7. XRD was then used to then determine

the structure of the deposited films. The X-ray diffraction patterns of the as-deposited films formed by dual source AACVD are shown in figure 52. From the collected diffraction patterns in all cases a broad feature can be seen around 20° 2θ which is attributed to amorphous scattering from the glass substrate (Fig. 52). The Bragg peaks for all the films could be indexed to the wurtzite structure of zinc oxide. The ZnO films showed a large degree of preferred orientation, with the crystallites oriented along the (101) plane. Preferred orientation effects are common in zinc oxide films but the crystallites tend to pack in the *c*-direction along the (002) plane.

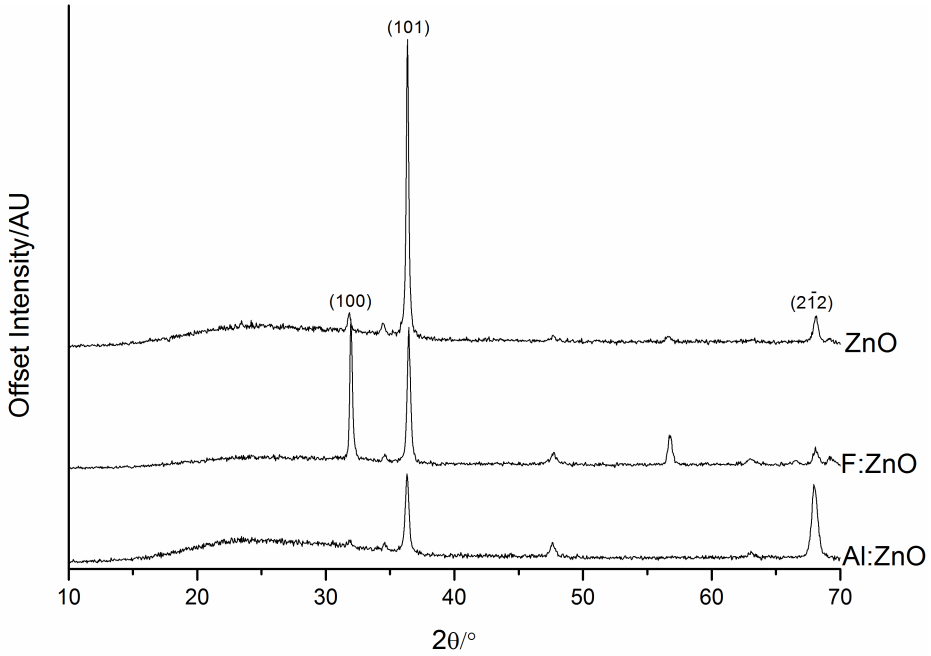

Figure 52: X-ray diffraction pattern of ZnO, F:ZnO and Al:ZnO thin films.

Preferred orientation in thin films is related to the surface free energy of each crystal plane and the (002) plane is the most energetically stable crystal plane for zinc oxide deposited on a surface without the influence of epitaxy. The mechanism of preferred orientation in zinc oxide films was studied by Fujimura *et al.*[178] They observed that (100) textured films are obtained by promoting the kinetic state (low substrate temperatures and fast growth rates) as opposed to the equilibrium state (high substrate temperatures and slow growth rates). Raising the substrate temperature and lowering the deposition rate should promote the (002) plane. As the fluorine source is added to the system and incorporated into the crystal structure the relative prominence of the (100) plane is increased leading to a more random

growth of crystallites. The introduction of fluorine could be altering the growth kinetics of the F:ZnO films compared to the ZnO and Al:ZnO films permitting an alternative pathway for precursor decomposition and film growth resulting in crystallites growing in the (100) plane as well as the (101) plane. A change in the growth kinetic and structural properties was also observed by Juarez *et al.*[179] This was confirmed by the SEM micrographs which clearly show a change in the ordering of the crystallites as fluorine is introduced within the system. Aluminium incorporation showed little change to the preferred orientation from that of plain zinc oxide.

Sample	Dep. T/°C	Film Thickness/nm	Crystallite Diameter/nm	a/Å	c/Å	Unit Cell Volume/Å^3
ZnO	450	714	108	3.2472(2)	5.1955(12)	47.442(14)
F:ZnO	450	820	448	3.2460(2)	5.2103(18)	47.543(18)
Al:ZnO	450	600	103	3.2496(4)	5.1914(16)	47.477(18)

Table 8: Film Thickness, crystallite diameter and unit cell parameters of ZnO films grown on glass by the dual source AACVD reaction of diethyl zinc with methanol at 450 °C.

Table 8 shows the film thickness, crystallite diameter and unit cell parameters as a function of dopant addition. The crystallite diameter for F:ZnO films was around 4 times greater than ZnO and Al:ZnO. This could be due to the effect that fluorine has on nucleation and growth in the ZnO system leading to enhanced crystal growth. The comparative unit cell parameters increased as a function of dopant addition. The film microstructure and thickness was investigated with scanning electron microscopy (SEM) and atomic force microscopy (AFM). The as-deposited films were composed of granular plate-like features as can be seen from figure 53. ZnO and Al:ZnO films exhibited very similar particle shape and dimensions and appeared smoother compared to the F:ZnO film. Figure 54 shows the AFM topographic images for the as-deposited films. The roughness (rms) determined by AFM imaging was 20 nm and 10 nm for ZnO and Al:ZnO respectively. The particle size was much larger for F:ZnO films however, which also links to the crystallite diameter as determined from the PXRD data. The PXRD data also showed the emergence of the (101) plane and the change in packing of the crystallites along this plane can also be seen from the SEM images as well as the AFM height image.

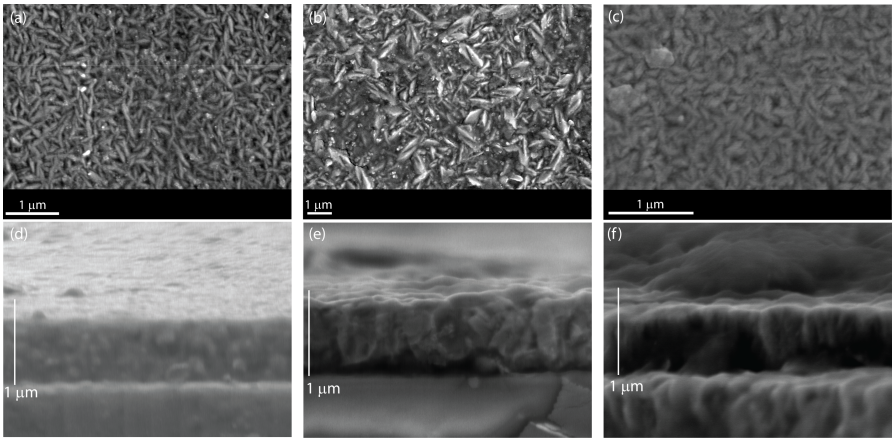

Figure 53: SEM images of (a) top down view of ZnO film, (b) top down view of F:ZnO film, (c) top down view of Al:ZnO film, (d) side on view of ZnO film, (e) side on view of F:ZnO film and (f) side on view of Al:ZnO film. All films were grown on glass by the dual source AACVD reaction of diethyl zinc with methanol at 450 °C.

The features for the F:ZnO film were on the sub-micrometer scale and the film appeared hazy. The surface roughness also increased when introducing fluorine into the system to 58 nm, compared to ZnO and Al:ZnO possibly by in-situ surface etching. This morphology is ideal for photovoltaic applications where optimised surface texturing is required for light scattering and trapping in thin film solar cells. The optimised surface structure required for light trapping and scattering is pyramidal morphology with particles in the size range of 400–700 nm which corresponds to the visible wavelengths of light. Notably the F:ZnO films were an average of 448 nm.

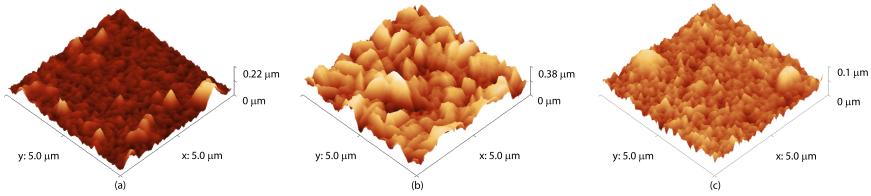

Figure 54: 3-D AFM image of (a) ZnO film, (b) F:ZnO film and (c) Al:ZnO film all grown on glass by the dual source AACVD reaction of diethyl zinc with methanol at 450 °C.

Hall effect measurements were conducted on the zinc oxide films formed in this work by using the van der Pauw technique to determine the electrical properties of the films. These studies showed that the ZnO films produced were of n-type character. The ZnO films showed stable sheet resistances of 7 Ω/sq. The source of intrinsic

n-type conductivity in ZnO is a controversial topic. Computational studies have shown that native defects are not high concentration shallow donors, typical requirement for conductivity in TCOs. Vacancies however were found to have sufficiently low formation energies but zinc and oxygen vacancies are deep acceptors and donors respectively. One possibility for the unusually high n-type conductivity observed pristine ZnO films could be due the to unintentional doping of hydrogen. The mechanism for this is the propensity of hydrogen to bond to oxygen and thus be incorporated into the crystal structure. The computational studies showed that H^+ is the most stable charge state for all Fermi level positions calculated and the formation energy low enough to allow for a large solubility of hydrogen in n-type ZnO. This was also seen in the charge carrier density of 5.80 x 10^{20} cm^{-3}. In order to further clarify the presence of unintentionally doped H^+, X-ray absorption spectroscopic measurements at the Zn K-edge to determine whether there is any oxygen or zinc vacancy in the system. Figure 55 shows the Zn K-edge EXAFS and associated Fourier transforms (FT) collected for a plain ZnO film and a bulk ZnO powder.

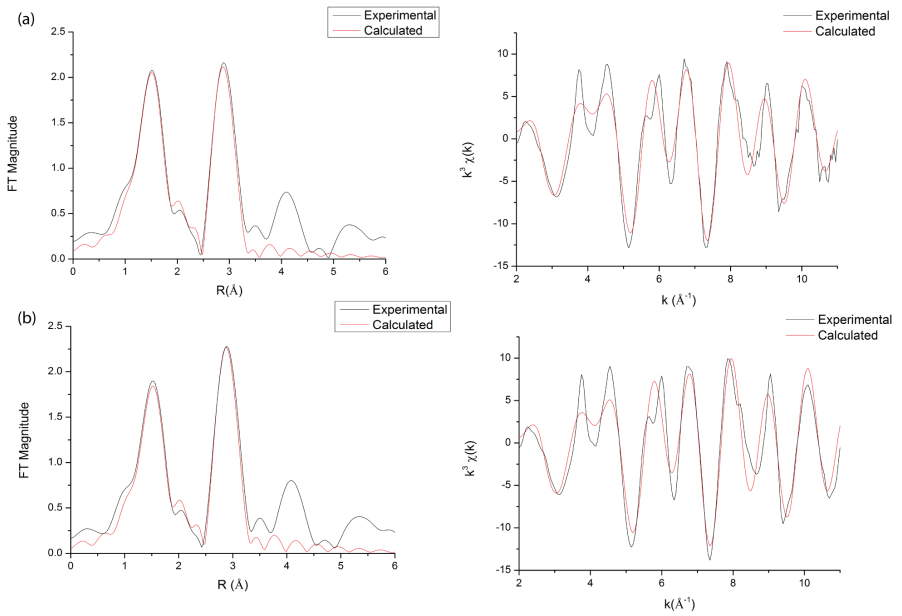

Figure 55: Zn K-edge EXAFS and associated Fourier transforms (FT) are given along with the calculated EXAFS and Fourier transforms for (a) plain ZnO film and (b) bulk ZnO powder.

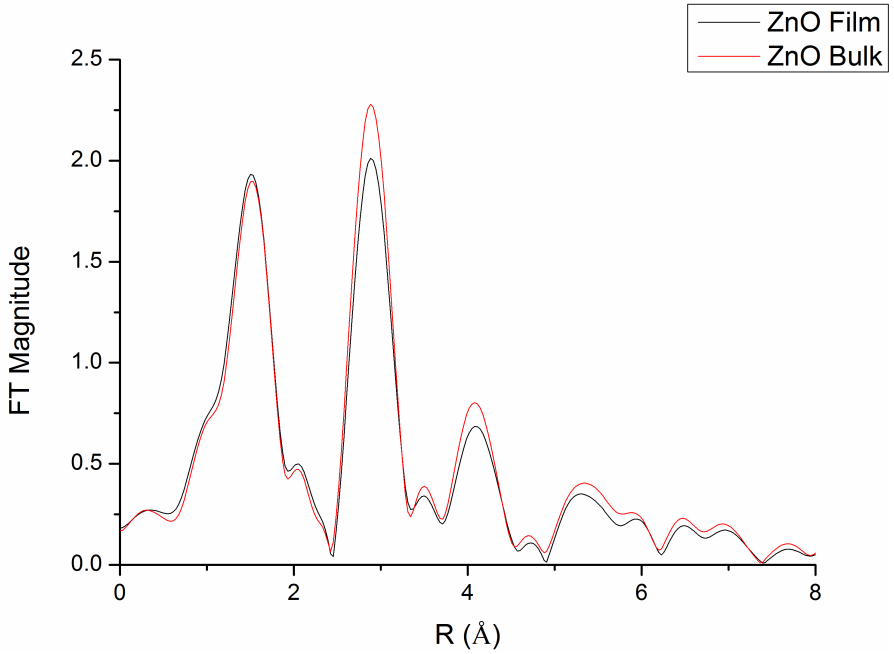

Figure 56: Comparison of the Fourier transforms of Zn K-edge EXAFS of bulk ZnO and ZnO film data.

System	Atom-Pair	N	R (Å)	σ^2(Å^2)	R-Factor
ZnO Bulk	Zn-O	4	1.96	0.005	0.055
	Zn-Zn	12	3.22	0.007	
ZnO Film	Zn-O	4.24	1.95	0.006	0.042
	Zn-Zn	9.9	3.23	0.0085	

Table 9: Structural parameters obtained from the analysis of Zn K-edge EXAFS data of bulk ZnO powder and as deposited ZnO film.

The difference in intensity in the Fourier transform plots between a plain ZnO film suspected to be doped with H^+ and a bulk ZnO powder was significant and a comparison between the Fourier transform of the Zn K-edge EXAFS of ZnO film and bulk ZnO and are shown in figure 56. The coordination number and bond distances obtained from detailed analysis of the EXAFS data are given in table 9. It is clear from the figure 56 and table 9 that the Zn-Zn coordination number is less by ca. 18% compared to Zn-O coordination. These results are similar to those reported recently for a hydrothermally synthesised ZnO powder claiming hydrogen incorporation into the ZnO structure.[180] Thus the results indicate the presence Zn vacancies in the film could support the presence of unintentional substitution of

hydrogen in the system. Further investigation (a combination of EXAFS/neutron diffraction/secondary ion mass spectrometry) would be required to fully support this argument however.

Sample	Film Thickness/nm	Sheet Resistance/$\Omega.sq^{-1}$	Roughness/nm	$\rho/\Omega.cm$	$\mu/cm^2.(V.s)^{-1}$	N/cm^{-3}
ZnO	714	7.2	20	5.12×10^{-4}	21	5.80×10^{20}
F:ZnO	820	4.5	58	3.70×10^{-4}	32	5.31×10^{20}
Al:ZnO	600	14	10	8.35×10^{-4}	17	4.35×10^{20}
TEC 8	650	8	-	5.2×10^{-4}	28	5.30×10^{20}
TEC 15	350	15	-	5.3×10^{-4}	21	5.60×10^{20}
Asahi-U	900	9.7	-	8.8×10^{-4}	32	2.2×10^{20}

Table 10: Electrical properties of as deposited zinc oxide thin films compared against commercial standards.

The introduction of fluorine into the system decreased the sheet resistance. Fluorine-doped zinc oxide is known to have fluorine incorporated by substitution of oxygen as the ionic radii are comparable, (F^-: 1.17 Å, O^{2-}: 1.22 Å) and this results in free electrons, which populate the conduction band. The fluorine concentration in the films was 2 at. % determined from wavelength dispersive X-ray analysis (WDX) analysis. The specific resistivity of zinc oxide films decreases from 5.12×10^{-4} Ω.cm to 3.70×10^{-4} Ω.cm with the introduction of fluorine into the system. The charge carrier concentration in these films was also lower than the zinc oxide films, with increased charge carrier mobility (Table 10), resulting in the plasma frequency shifted to lower energy. The Al:ZnO films deposited had a thickness of 600 nm and a sheet resistance of 14 Ω/sq. The aluminium concentration was 4 at. % determined by WDX analysis. The specific resistivity increased in Al:ZnO films and the mobility of the charge carriers was also reduced. These films however showed a reduction in charge carriers even though the aluminium concentration determined by WDX was relatively high (4 at. %), indicating clustering or segregation of dopant species resulting in deleterious effects to the electrical properties of the films.

The relatively small size of the surface features coupled with the low surface roughness make these coatings suitable for electrodes in dye sensitised solar cells but may also find an application in architectural glazing to reduce radiation energy loss by reflecting the thermal IR radiation emitted from a room due to low scatter in the visible region because of the small particle size. All the films displayed prominent interference effects. These interference fringes are caused by the multiple reflections at the three interfaces of the air/thin film/transparent substrate bi-layer. The room temperature transmission and re-

flection characteristics of the zinc oxide films deposited by AACVD were investigated using visible/near IR spectrometry. The spectra shown in figures 57 and 58 were taken using an air background and indicate a high transparency across the visible (~ 80% transmission at 550 nm in air, including the substrate absorbance) for zinc oxide films. The films also showed 50% reflectivity in the infrared at 2500 nm in air.

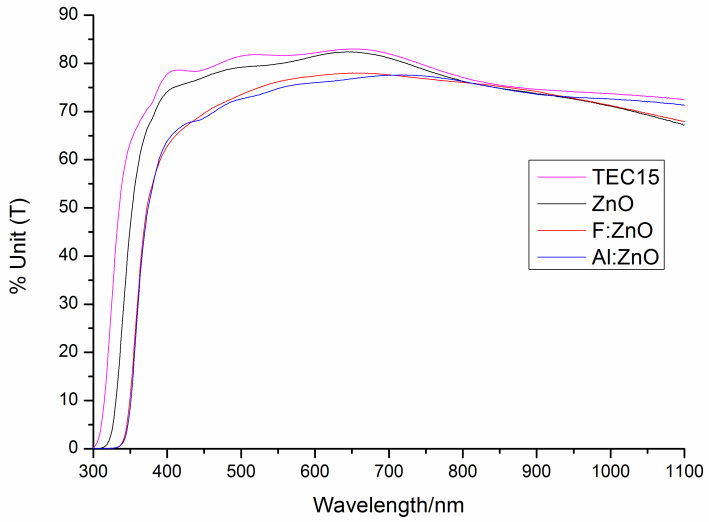

Figure 57: Optical transmission spectrum taken against an air background showing zinc oxide films and doped analogues grown at 450 °C compared to commercial F:SnO_2 (NSG TEC 15).

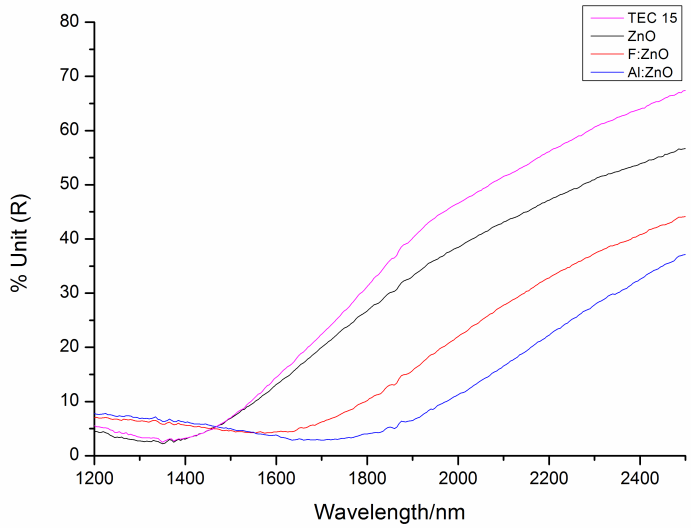

Figure 58: Optical reflection spectrum taken against an air background showing zinc oxide films and doped analogues grown at 450 °C compared to commercial F:SnO_2 (NSG TEC 15).

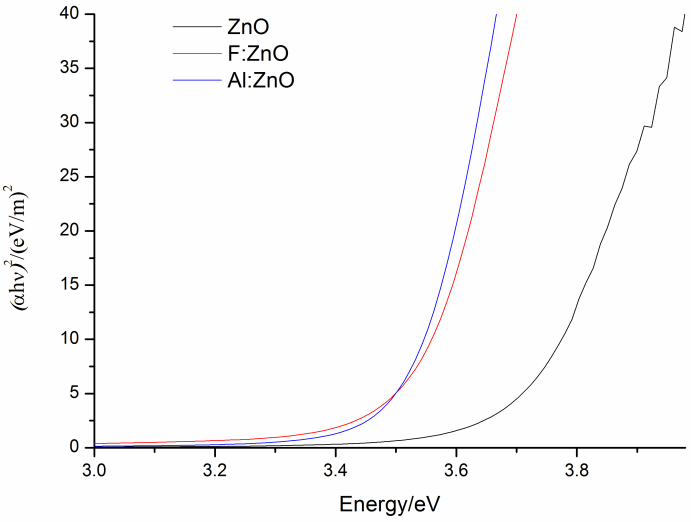

Figure 59: Tauc plots to determine optical band gap for zinc oxide, fluorine doped zinc oxide and aluminium doped zinc oxide films deposited at 450 °C.

The transmission for F:ZnO and Al:ZnO decreased slightly to ~ 76%. Included in figures 57 and 58 are plots of spectra taken from leading commercial F:SnO_2 thin films on glass substrates. Pilkington TEC 8 and TEC 15 glass was used as the reference products with a

sheet resistance of 15 Ω/sq as well as resistivities of the same order of magnitude. The onset of the infrared reflection occurs at the plasma resonance frequency where the electromagnetic radiation incident on the film can induce resonance of the free carriers within the metal oxide matrix. The plasma frequency is dependent upon the conductivity, the dielectric constant and the mean free relaxation time of the material.[71] This means that increasing the charge carrier density and decreasing the charge carrier effective mass (reducing retarding forces on the free electrons, such as scattering defects) will increase the plasma resonance frequency of the TCO, thus shifting the resonance reflection effect to a shorter wavelength. This effect can be seen in figure 58 with zinc oxide films, where the charge carrier concentration was high and thus the plasma edge was seen at approximately 1400 nm. The ZnO films showed high reflectivity in the IR but lower than that of commercial products. The reduction in charge carriers with F:ZnO and Al:ZnO relates to the onset of the plasma edge of these samples with the onset for F:ZnO around 1600 nm and the of Al:ZnO around 1800 nm, red shifted compared to ZnO films. The IR reflectivity however was for F:ZnO and Al:ZnO was around 40% and 35% respectively. Essential properties for low-ε-coatings include a high reflective value for IR radiation (> 2000 nm) and a rapid onset of the plasma edge which separates the transparent and reflective regime across the wavelength range. ZnO films displayed both of these attributes in this work and approach that of commercially available films, whereas F:ZnO and Al:ZnO were more suited to PV applications. The direct band gaps were determined by constructing Tauc plots using the $(\alpha h\upsilon)^2$ relation as shown in figure 59. These ranged from 3.7 eV for ZnO to 3.4 and 3.5 eV for F:ZnO and Al:ZnO respectively. This is due to the Burstein-Moss effect, as electrons populate the conduction band, the optical band gap is effectively increased.

4.4 CONCLUSIONS

AACVD was shown to be an effective and simple method for the deposition of highly transparent and conductive zinc oxide, fluorine-doped zinc oxide and aluminium doped zinc oxide films. The unintentionally doped zinc oxide films discussed in this chapter displayed excellent optical and electrical properties comparable to coatings based on tin and indium oxides. These could be used as low-

ε-coatings or electrodes in photovoltaics. Dopants could easily be incorporated into the system and this was shown by synthesizing fluorine doped zinc oxide and aluminium doped zinc oxide. Fluorine doped zinc oxide films displayed high transparency and excellent electrical characteristics. The surface morphology together with the opto-electronic properties makes this material ideal for PV applications requiring light trapping and scattering. Aluminium doped zinc oxide films also displayed high transparency with electrical properties suitable for PV applications requiring low haze and light scattering such as in DSSC. Control over the carrier mobility, charge-carrier density, IR reflectance, crystallinity and the surface morphology of the films have shown to be highly dependent upon dopant introduction using this technique. This work demonstrates a move towards tailoring functional properties of the films to specific applications, including transparent conducting materials for thin film photovoltaics, polymer devices and architectural glazing.

Chapter V

ZEOLITE FILMS

5

ZEOLITE FILMS BY CVD AND HYDROTHERMAL SYNTHESIS

Zeolites are the most important class of crystalline nanoporous solids with a range of applications including ion-exchange, gas separation, absorption and catalysis. These crystalline solids are widely used in the form of powders. However, over the last twenty years zeolite membranes and films have been extensively studied not only for gas-separation applications, but also for more novel emerging applications, in particular in the field of electronics as low-k dielectrics and as corrosion resistant materials. The current processes for the preparation of zeolite films have been limited to solution processing methods. These processes involve the use of an organic templating agent in a sol-gel/hydrothermal process, similar to conventional methods to produce crystalline powder zeolites. To overcome some of these issues the work in this chapter explores the combination of chemical vapour deposition (CVD) and hydrothermal (HT) synthesis to deposit amorphous/crystalline oxide films on a given substrate. The driving force for carrying out the work was initially to see whether commercially available silica coated barrier glass from NSG coated with tetrapropylammonium hydroxide (TPAOH) could be converted into a zeolite film. This proved the concept of converting dense amorphous silica films into crystalline zeolites. As a result of this, CVD was used to deposit precursors for hydrothermal work up to yield microporous materials. Amorphous silica films deposited by CVD were successfully converted to zeolite using hydrothermal methods.

5.1 INTRODUCTION

The use of zeolite powders in ion-exchange, gas separation/absorption and catalysis has been known for decades making zeolites the most important class of crystalline nanoporous solids.[138,181] The use of zeolites in the form of films dates back to the 1940s in ion-selective sensing applications. The fabrication of zeolites as films/membranes during the 1940s is sometimes described as the brute force approach

where zeolite powders were pressed into pellets or work was conducted on the faces of zeolite single crystals. The performance of these rudimentary zeolitic films was poor and the processing challenge for high performance (in terms of coating uniformity) zeolite membranes became apparent.[59,125–127,139–141,182–184] There has been a large amount of research invested in the last 25 years on zeolitic films in order to optimise the processing challenge as well as controlling particle morphology and microstructure which is key to the overall peformance of the zeolite film for a given application. The opportunity afforded by growing zeolite films allows for unconventional applications to be explored such as low-k dielectric coatings in the electronic industry, corrosion resistant coatings, chemical sensors, ion-exchange electrodes and light harvesting devices. The first commercially available zeolite films were concentrated to small-scale applications and the films were coated on 10 m^2 substrates. The main issues in commercialisation, despite the intense research, has been the high cost of fabrication, poor performance of the zeolite films compared to powder analogues and major difficulties in reproducibly coating large substrate areas. Large area coatings inevitably require reliable processing technologies, while satisfying essential film characteristics such as film continuity, thickness control, crystallite orientation (pore orientation) and pin-hole (defect) free films.[127,128,140,143,182,183,185]

The established laboratory scale routes to zeolite synthesis are *in-situ* crystallisation, dry and wet gel conversion and secondary seeded growth. *In-situ* growth is where the support is kept in contact with the zeolite precursor solution and crystal growth is promoted on the surface of the support. The quality of the membrane formed however is sensitive to procedures and conditions, including the position of the support in the autoclave. A major factor affecting membrane quality is the long induction time in the autoclave as over-exposure to the basic medium required for zeolite growth can result in chemical attack of the membrane. The second established method is known as the dry/wet gel conversion.[121,127,182,183] This was first described by Xu *et al*. with the synthesis of mordenite frameworMFI membranes by coating an amorphous aluminosilicate gel onto a substrate and crystallisation by exposing the coated substrate to vapours of triethylamine, ethylenediamine and water. When the structure directing agent is not involved in the gel synthesis then the process is known as "Vapour Phase Transport" (VPT). When the gel contains the templating agent

the amorphous to crystalline conversion is known as "steam-assisted crystallisation". The problem with this method is that there is an associated large volume shrinkage during the gel transformation to zeolite which often leads to defects in the films.

In order to improve upon some of the drawbacks associated with in-situ crystallisation and dry/wet gel conversion, seeding and secondary growth (SSG) is the third established route to synthesising zeolite films. Secondary seeded growth essentially decouples the nucleation step from crystal growth. For film synthesis a layer of seed crystals, previously nucleated and deposited on a support, are grown into a continuous layer. Seeded films tend to have enhanced physical and mechanical properties than in-situ or wet/dry gel grown films. SSG films are currenty seen as the most attractive route for depositing zeolite layers due to improved control over physical and mechanical properties such as crystal orientation and film defects. Although SSG offers more in scalability than zeolite films grown by in-situ crystallisation and dry/wet gel conversion there are however issues with scalability.[5,125,126,142]

To overcome some of these issues and more importantly to enhance the possibility of large-scale membrane and film production capabilities, chemical vapor deposition (CVD) was used to deposit an amorphous film on a given substrate, followed by conversion to a zeolite using hydrothermal methods.[29,48] The MFI system was chosen due to the forgiving synthesis conditions and because the MFI structure is a model system for zeolite membranes to investigate crystal preferred orientation on membranes. The mordenite framework inverted (MFI) structure, as described in the introduction chapter, is orthorhombic (crystallises in *Pnma)* but can exist as monoclinic ($P12_1/n1$) after calcination. For separation membranes crystals oriented in the *b*-axis i.e. parallel to the substrate are more favourable than *c*-axis oriented crystals. The crystal orientation is heavily influenced by the hydrothermal conditions used during the synthesis. For *b*-axis oriented crystals, ideally lower temperature synthesis and shorter durations are required compared to *c*-axis oriented films. This chapter describes the conversion of a dense, amorphous silicon dioxide film into silicalite-1 (S-1) and a titanium doped silicon dioxide film into titanium silicalite-1 (TS-1). As well as titanium doped silica films, iron doped silica films could also be synthesized during the CVD stage of the process as well as retention of local-structure upon conversion to the MFI struc-

ture. This new methodology represents a powerful strategy for facile incorporation of titanium into the silicate matrix with retention of the local structure during conversion to crystalline zeolite. It also offers the possibility for including a range of alternative metal dopants into silicon dioxide matrices in a controlled fashion that could enable formation of a wide range of functional zeolitic films.

5.2 EXPERIMENTAL

Silica coated barrier glass supplied by NSG was cut into 1 cm^2 pieces and dip coated with tetrapropylammonium hydroxide (TPAOH, 1M) solution. TPAOH is described as a template molecule in zeolite synthesis. It is described as a template molecule because it is thought to direct the structure of the porous silicate/aluminosilicatezeolite framework over the template molecule, and the template molecule is retained in the pores of the structure. It is also described as a structure directing agent (SDA) but the exact mechansim of zeolite crystallisation is unclear. The template can be removed from the resultant structure by calcination at 550 °C without collapse of the porous structure. The template coated glass was then suspended above distilled water (0.5 g) in a PTFE liner. The liner was loaded into a stainless steel autoclave and a SAC was carried out at 180 °C for 24 hours. The autoclave was then cooled to ambient temperature and the product was washed with distilled water and dried in the oven.

Amorphous silicon dioxide and titanium doped silicon dioxide were both synthesized on two different substrates, alumina and silicon wafers. The procedure of forming dense films is schematically described in figure 60. Aerosol-assisted chemical vapour deposition (AACVD) was carried out using a hot-walled quartz tube loaded with the specific substrates. Tetraethylorthosilicate (TEOS) or a mixture of TEOS and tetraethylorthotitanate (TEOT), in the molar ratio of 100:1 Si:Ti, were nebulised using a humidifier (operating at 20 kHz) and transferred to the reaction chamber using nitrogen carrier gas while maintaining the substrate temperature at ca. 700 °C in the reaction chamber. Iron doped silicon dioxide films were synthesised in the exact same manner with a mixture of TEOS and ferrocene in the molar ratio of 100:1.

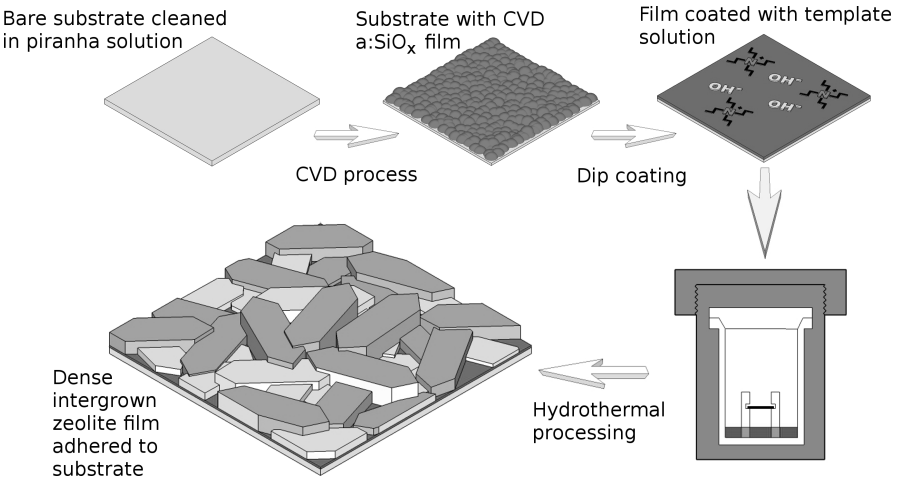

Figure 60: Schematic diagram of the process for making amorphous films and conversion to crystalline zeolite is shown.

The CVD reaction setup is shown is figure 61. Typically after an hour, the substrates were cooled and then coated with a solution of tetrapropylammonium hydroxide (TPAOH, 1 M) and transferred into a PTFE-lined stainless steel autoclave. Hydrothermal reactions were performed at ca. 165 °C for 24 hours. The conversion process for iron doped silicon dioxide films to Fe-Silicalite however took 48 hours. Products were then washed with distilled water and dried at ambient temperature. The structure directing agent was removed by calcination of the films at 550 °C and both the as-synthesized and calcined samples were characterized in detail.

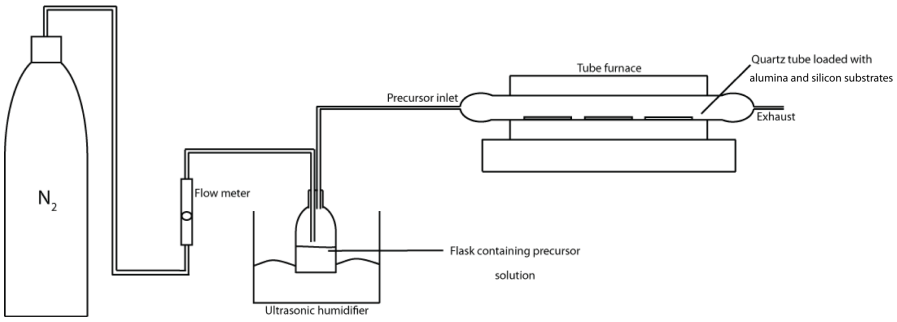

Figure 61: Schematic of the AACVD process used to deposit silica films on alumina and silicon substrates.

The standard characterisation techniques for zeolite films in terms of structure are by X-ray methods (angle and energy dispersive) and scanning electron microscopy (SEM). XRD gives information about the phase, crystal orientation and atomic positions. SEM gives information about the crystal size, morphology, defects and thickness.

Complimentary techniques such as AFM and HR-TEM can also give valuable information regarding zeolite films growth and zeolite composition resepctively. The relative quantity of zeolite on a porous support can be estimated by gas adsorption (BET). If a dense support is used then ellipsometry is the preferred tool to determine film thickness and void volume fraction.

XRD data was collected using a Bruker D4 diffractometer equipped with a copper X-ray tube. SEM micrographs were recorded using a JEOL JSM-6301F field emission SEM operated at an accelerating voltage of 5 kV. Ti K-edge XAS measurements were carried out at beamline (B18) at the UK synchrotron, Diamond, which operates at 3 GeV and 300 mA. The beam line is equipped with Si(111) double crystal monochromator, ion chambers for measuring incident and transmitted beam intensity and a 9 element Ge fluorescence detector for measurement in fluorescence mode. All the measurements were carried out in fluorescence mode and typically 6 scans were averaged to produce the spectra. X-ray absorption spectra were processed using ATHENA[158] software and subsequent analysis of the EXAFS data were performed using EXCURVE[186]. Atomic force microscopic images were recorded using VEECO diDimension in tapping mode.

5.3 RESULTS AND DISCUSSION

Zeolite films were prepared on silica barrier glass supplied by NSG by dip coating the glass slides with TPAOH followed by hydrothermal treatment at 180 °C for 24 hours. The resultant films were white in appearance and adhered to the glass substrate. The films were resistant to peeling by the Scotch tape test and could not be removed by a brass scalpel but could be removed from the support by a steel scalpel. Figure 62(a) shows the SEM image of films grown on silica barrier glass and highlighted is the conventional morphology of S-1 crystals lying beneath unusual plate-like morphology of S-1 crystals. Figure 62(b) shows a high-resolution image showing the plate-like morphology.

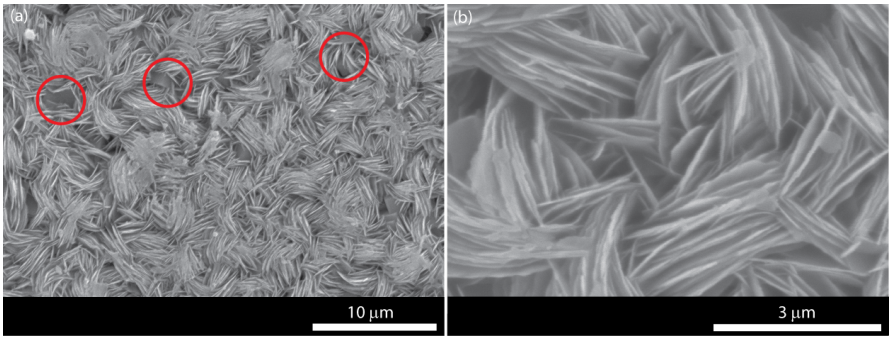

Figure 62: SEM of (a) low-resolution image of silicalite-1 (S-1) film grown on SiO_2 barrier glass highlighting the nature of prismatic crystals underneath platelet type morphology of zeolite crystals and (b) high-resolution image of silicalite (S-1) film grown on SiO_2 barrier glass highlighting unsual plate like morphology of S-1 crystals.

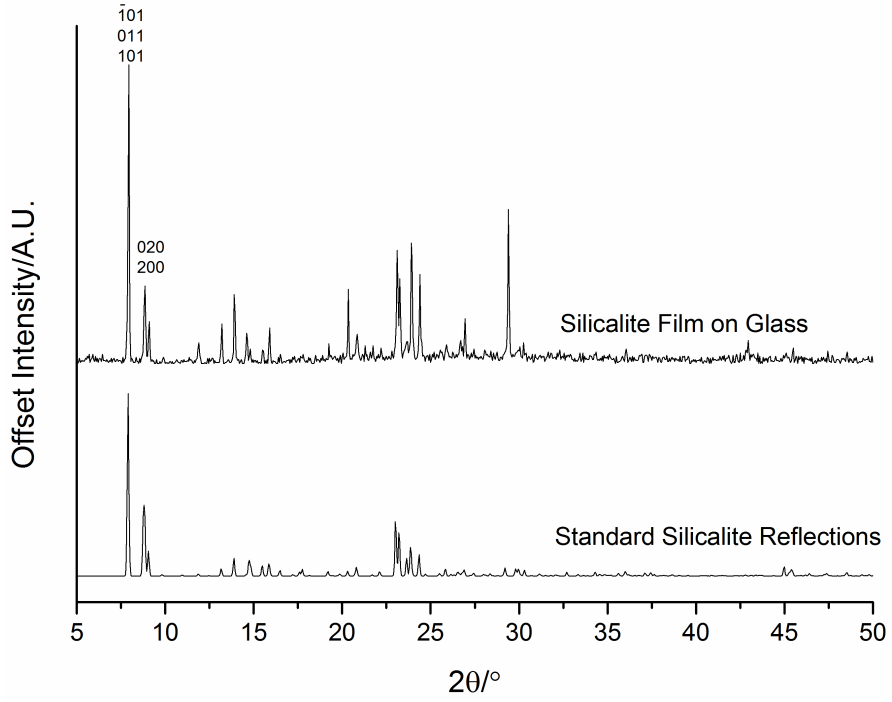

Figure 63: XRD pattern for silicalite-1 film grown on SiO_2 barrier glass (NSG) by dip coating the surface with TPAOH followed by SAC at 180 °C.

The corresponding XRD pattern associated with the S-1 film/SiO_2 glass is shown in figure 63. The characteristic low angle reflections for silicalite can be seen. Uncharacteristic reflections for silicalite at high angle were also observed indicating a degree of preferred orientation of the crystals also seen in the SEM micrographs from the plate like morphology of the crystals.

Dense compact silica films were synthesised on alumina and silicon substrates by the pyrolysis of tetraethylorthosilicate (TEOS) using AACVD. TEOS is commonly used in APCVD to deposit silica films. AACVD was used here due to the simplicity of non heated lines and the compatibility of TEOS with the AACVD process.[6] The deposition process of silica requires no external oxygen source. Studies have shown that possible decomposition pathway for TEOS is most likely to liberate ethylene as such:

$$(SiO)_2Si(OC_2H_5)_2 \longrightarrow (SiO)_2Si(OC_2H_5)(OH) + C_2H_4 \quad (57)$$

$$(SiO)_2Si(OC_2H_5)(OH) \longrightarrow (SiO)_2Si(OH)_2 + C_2H_4 \quad (58)$$

The deposition rate is most likely to be limited by the rate of removal of surface alkyl groups as ethylene. The introduction of oxygen has no bearing on the deposition rate. The introduction of ozone however can be used to enhance the deposition rate of silica films as it provides a lower energy pathway for decomposition by trapping TEOS molecules on the surface and reacting with the ethoxy ligands. In order to dope titanium into these films, the titanium analogue of TEOS, tetraethylorthotitanate (TEOT) was mixed with TEOS during the CVD stage. These films were then converted into dense zeolite films by hydrothermal treatment of CVD grown amorphous films of silicon dioxide and titanium doped silicon dioxide into S-1 and TS-1 films respectively on both silicon and alumina substrates. The zeolite films were white in appearance and were adherent to the substrate. Typical XRD patterns of the as-synthesized films on alumina are shown in figure 64. It is clear from the XRD pattern that the amorphous silicon dioxide film on alumina (a:SiO_2 on Al_2O_3) does not have any reflections related to a dense silicate phase, in particular no reflections related to quartz were observed.

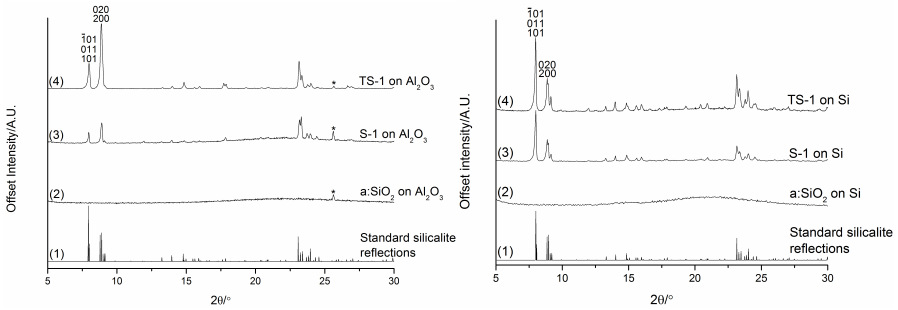

Figure 64: Typical XRD patterns of the as-synthesized films deposited on Al_2O_3 on the left and silicon substrates on the right. A reflection from the alumina support is asterisked and silicon reflections appear above 30° in 2ϑ. Also note that the relative intensities of the reflections of the zeolite films are not similar to those typically seen for the corresponding powder which is due to preferred orientation of the zeolite crystals.

Similar observations were made for the titanium system and no forms of dense titania were present. Minor reflections from the alumina substrate are asterisked. Substrate reflections were also seen for films deposited on silicon wafers. The XRD patterns demonstrate that the amorphous film has been converted to phase-pure silicalite, as shown in figure 65. However, the relative peak intensities of the zeolite films differ to those seen in the corresponding bulk powder, due to preferred orientation effects. For example, the 020/200 reflection appears to be intense compared to the -101/ 011/101 reflection. A similar observation has been made for oriented zeolite films, however, our samples appear to be not completely *b*-oriented.[125]

Figure 65(a) and (c) shows SEM micrographs of amorphous silicon dioxide and titanium doped silicon dioxide films deposited on alumina. All the amorphous films produced by the CVD process showed dense, compact uniform films composed of spherical particles independent of substrate. Figure 65(b) and (d) show SEM micrographs of crystalline S-1 and TS-1 films deposited on alumina. The SEM images back up the XRD data showing that Figure 66 shows low resolution SEM micrographs of amorphous titanium doped silicon dioxide and TS-1 on alumina substrates showing that there are no macroscopic cracks/defects which would limit film application in catalysis and gas separation.

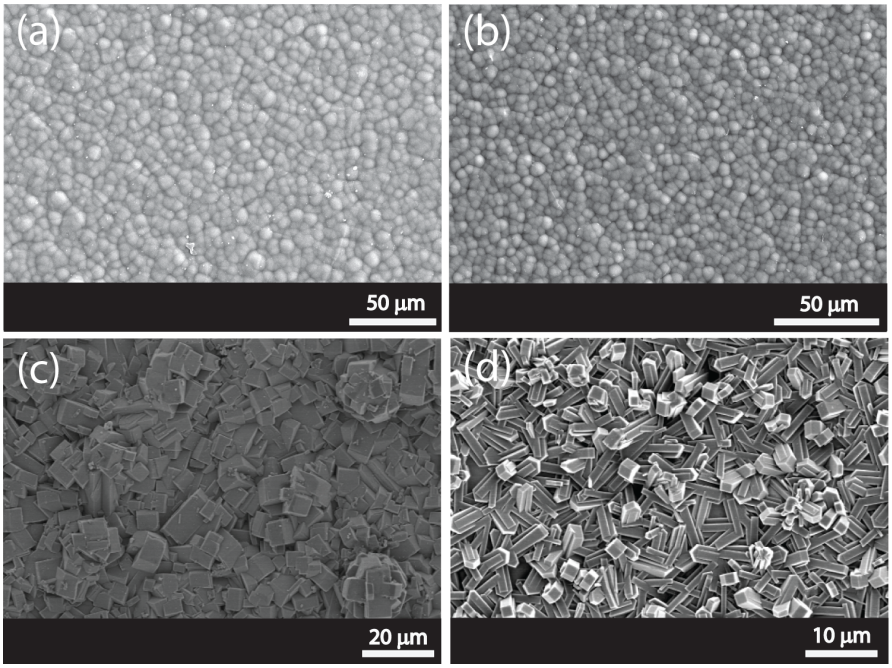

Figure 65: Typical SEM micrographs of (a) amorphous silicon dioxide film on alumina, (b) amorphous titanium doped silicon dioxide films on alumina, (c) S-1 film on alumina and (d) TS-1 film on alumina.

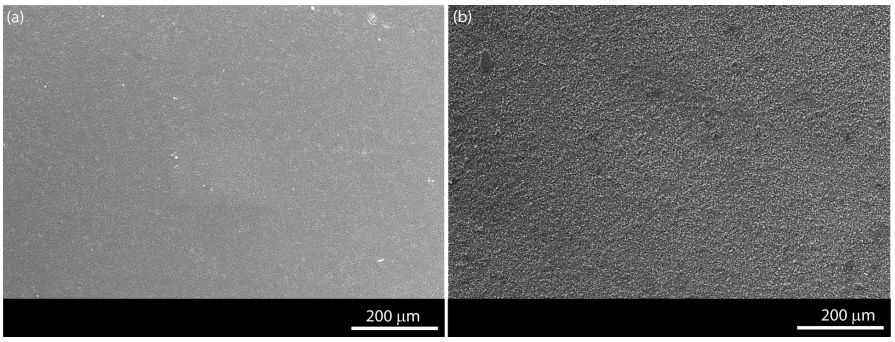

Figure 66: Low resolution SEM micrographs of (a) amorphous titanium doped silicon dioxide film on alumina and (b) TS-1 film on alumina showing that there are no visible macro-cracks in the as-deposied amorphous film as well as the crystalline zeolite film.

Amorphous silicon dioxide and titanium doped silicon dioxide films were also deposited on silicon substrates and are shown in figure 67 for completeness. The amorphous silicon dioxide films and doped analogues looked identical to amorphous films deposited on alumina substrates. The zeolite films on silicon however differed to zeolite films on alumina. The preferred crystal orientation of zeolite films deposited on silicon substrates appears more random compared to zeolite films deposited on alumina. A reason for this could be the

length of crystallisation and zeolite films deposited on silicon substrates may require less time to form on the parent substrate compared to films deposited on alumina. Okubo *et al*. showed that it was possible to convert silicon wafers with a native oxide layer into S-1 films and during the conversion process it is not known whether silicon is being dissolved and re-deposited as zeolite.[137] The difference in preferred crystal orientation of the zeolite films deposited on alumina and silicon can be clearly seen in the XRD patterns (figure 64) as the films deposited on silicon substrates reflect a more random distribution of zeolite crystals to that of a pure powder sample of S-1 compared to zeolite films deposited on alumina substrates which are somewhat *b*-oriented. A full time-evolution of zeolite films on alumina and silicon substrates however would be needed to carry out in order to verify this observation. In light of this, the majority of the analysis was focussed on alumina substrates to reduce any ambiguity arising from using silicon substrates.

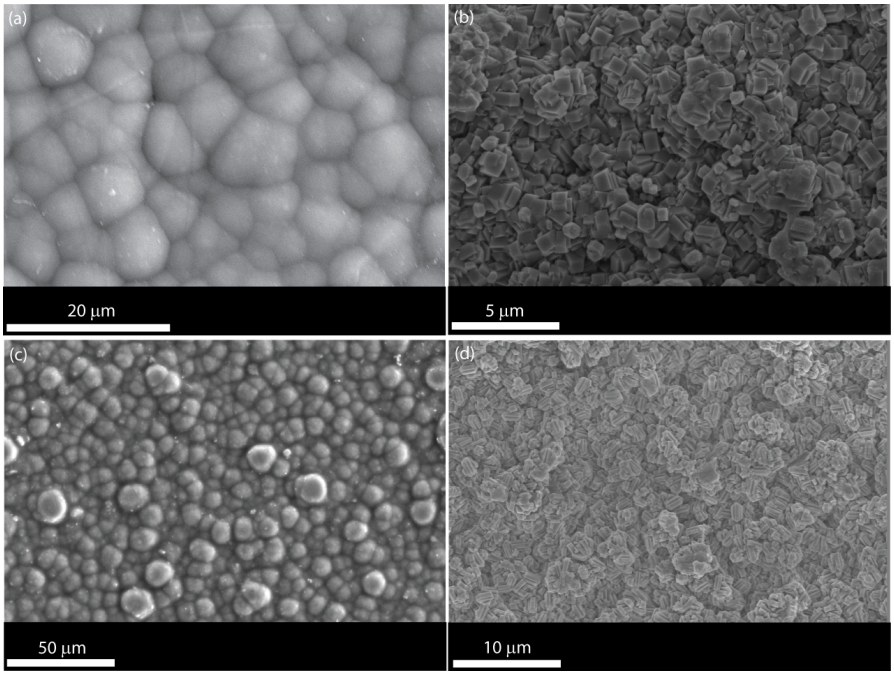

Figure 67: Typical SEM micrographs of (a) amorphous silicon dioxide film on silicon, (b) amorphous titanium doped silicon dioxide films on silicon, (c) S-1 film on silicon and (d) TS-1 film on silicon.

Atomic Force Microscopic (AFM) was performed on amorphous titanium doped silicon dioxide films and crystalline TS-1 films on alumina and is shown in figure 68. The image suggests that the zeolite crystals were formed from the spherical amorphous particles

indicating a direct solid-solid conversion of the amorphous matrix to a crystalline solid. The mechanism of conversion of a dry amorphous gel into a crystalline metastable phase (zeolite) is still a contentious subject but it is believed to be via a solid-solid transformation, but studies have shown that if a pathway exists, then a hydrothermal/-solvothermal route will prevail over true solid-solid transformations as the activation energy for the former case is lower. It has been proposed that potential growth units from the amorphous material may detach (dissolve) and migrate through the solution to a crystal growth site. Another case proposed is that the detached unit may never fall into solution but but be transferred from an amorphous region to an adjacent centre of crystal growth. AFM studies conducted at different time periods of crystallisation would shed more light on the mechanism of transformation of CVD grown amorphous layers to crystalline zeolite films.

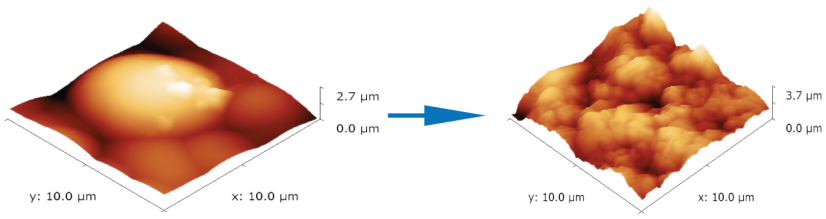

Figure 68: AFM image of amorphous titanium doped silicon dioxide film on alumina and conversion into TS-1 film.

EDX analysis for the titanium system showed the presence of titanium in the film (titanium content of ca 2 at. %), however, it was not possible to determine whether titanium is incorporated into the silicate matrix in both the amorphous and zeolite film using either XRD or SEM techniques.

In order to establish that the metal ions are incorporated into the zeolitic matrix and hence show that doping at the CVD stage carried through the transformation process, X-ray absorption spectroscopy studies at the Ti K-edge were performed. Ti K-edge X-ray absorption spectra of the amorphous and crystalline films are shown in Figure 69 along with two model compounds $Ti(OSiPh_3)_4$ and ETS-10 (tetrahedral Ti and octahedral Ti coordination, respectively) for which the local structure is well documented. Ti^{4+} is well known to adopt, four (tetrahedral), five or six coordination environment.[159,187,188] While 4 and 6 coordinated titanium centers are common, 5 coordinated is

exceptionally rare and therefore we used the above mentioned two model systems to determine the structure of titanium centers in the titanosilicate films. The intense pre-edge peak (marked as A in figure 69) is used extensively to determine the local coordination geometry of the titanium ions in a variety of systems.[159,188] It is well-established that this pre-edge feature is intense for metal ions having tetrahedral coordination and less intense for octahedral coordination; the intensity also depends on the electronic structure of the metal ions in a given oxidation state, for example systems with d^0 electron configuration tend to have the highest intensity. Comparison of the intensity of the pre-edge peak in the XANES of titanosilicate films with the two model systems suggests that titanium ions are in the +4 oxidation state and in a tetrahedral geometry. In particular, the XANES features (both A and B) of the titanosilicate films appears to be similar to that of the model compound $Ti(OSiPh_3)_4$ implying that isolated tetrahedrally coordinated titanium ions are present in the silicate matrix.

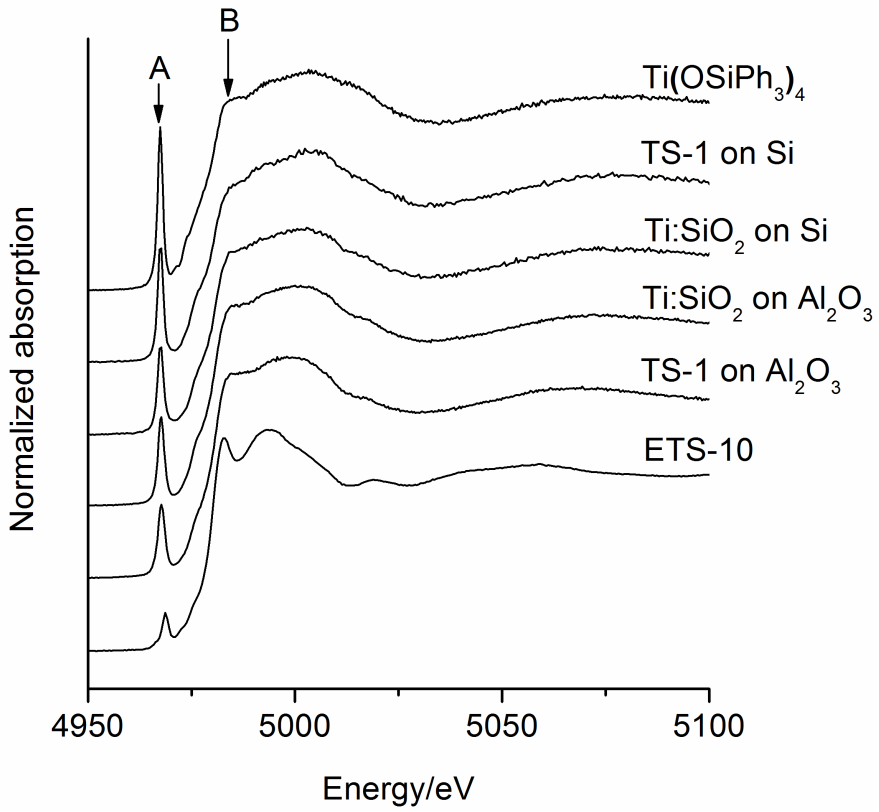

Figure 69: Ti K-edge XANES of titanium doped silicon dioxide films and corresponding model compounds.

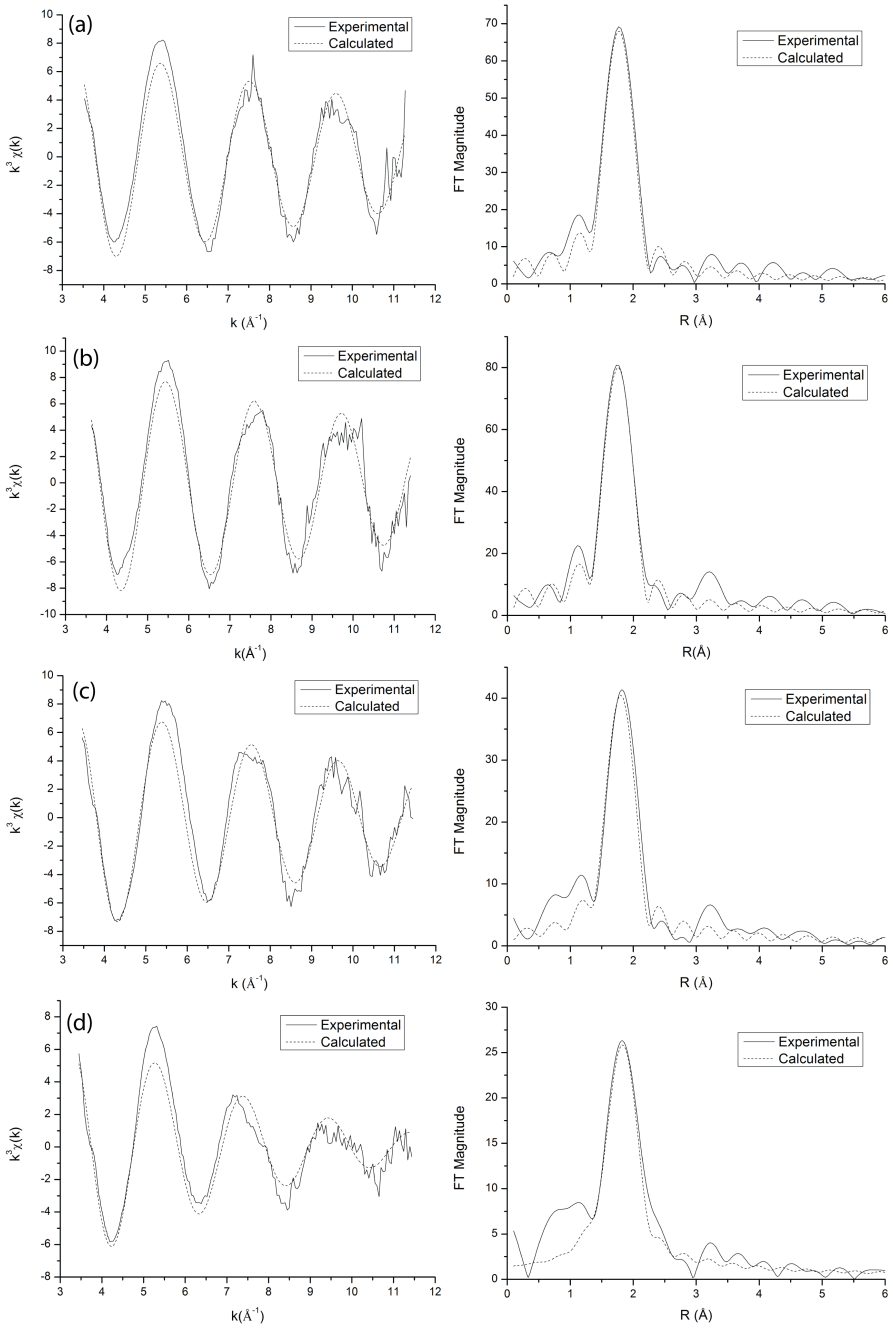

Figure 70: Ti K-edge EXAFS and associated Fourier transforms (FT) are given along with the calculated EXAFS and Ft's for (a) titanium doped silicon dioxide film on silicon, (b) TS-1 film on silicon, (c) titanium doped silicon dioxide film on alumina and (d) TS-1 film on alumina. The EXAFS derived Ti-O distances are (a) 1.81 Å, (b) 1.82 Å, (c) 1.82 Å and (d) 1.86 Å. Typical Ti-O distance for a highly ordered tetrahedral coordination is ca 1.80 as evidenced for $Ti(OSiPh_3)_4$ compound.

Further evidence of the tetrahedral coordination geometry of the titanium ions in both amorphous and crystalline zeolitic films comes

from detailed analysis of the Ti K-edge EXAFS data. The analysis was focused on the first shell, since it directly reveals the nature of first neighbor coordination geometry. The best fit obtained between experimental and computed EXAFS are shown in figure 70. The EXAFS derived average first neighbor Ti-O distance for all the titanium containing films are in the range of 1.80 to 1.87 Å which suggests that some of these systems contain distorted Ti-O environments. In particular the alumina supported films show lower pre-edge intensity and a Ti-O distance of ca 1.87 Å compared to the silicon supported systems in which the Ti-O distance is ca 1.81 Å. Similar observation has been made for vanadium containing systems.[189] Although the higher Ti-O distance may indicate the presence of some octahedral Ti-O species, comparison of the Ti K-edge feature, figure 69, (marked as B) on the top of the edge suggest that they are very similar, irrespective of the support, to the model compound $Ti(OSiPh_3)_4$ wherein Ti(IV) ions are present in regular tetrahedral coordination; presence of octahedral coordination will increase the intensity of the feature B, as seen in ETS-10 data.

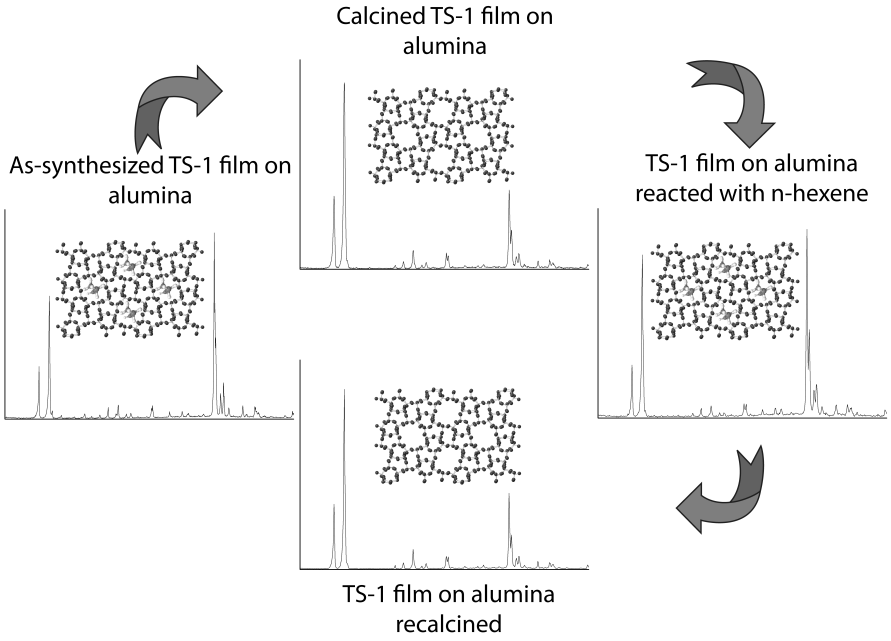

Figure 71: Pore accessibility for TS-1 films on alumina followed by XRD. Note that the relative peak intensities of the reflections at low angles are different with respect to high-angle in the as-synthesised (which contains organic template) and the one reacted with n-hexene compared to the calcined forms.

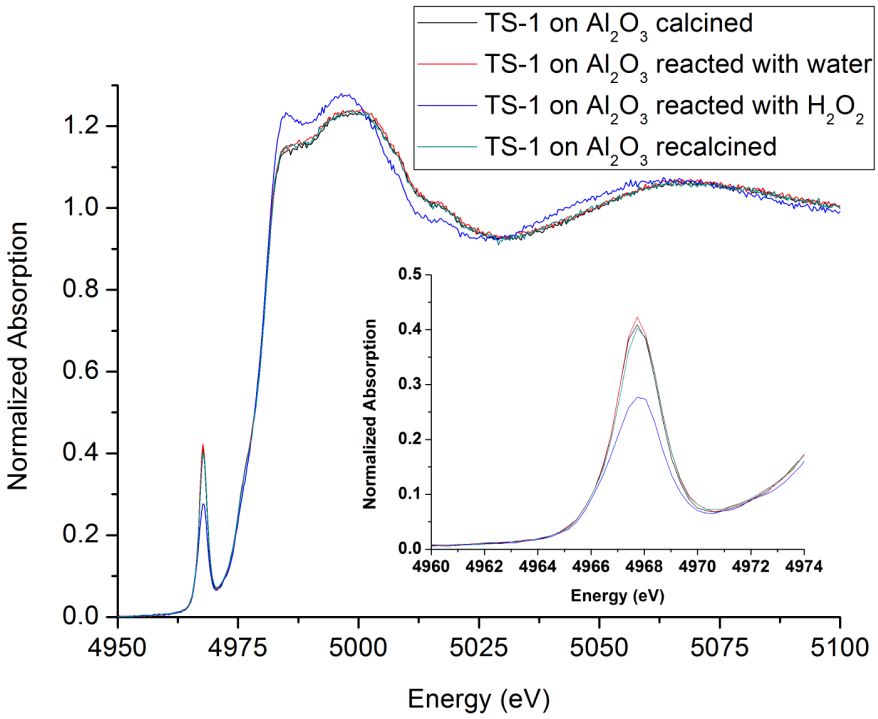

Figure 72: Reactivity of titanium centres for TS-1 films on alumina followed by Ti K edge XANES.

Reactivity and pore accessibility of the titanium silicalite-1 (TS-1) films were confirmed through a representative reaction with n-hexene, water or hydrogen peroxide. The XRD pattern of the sample reacted with n-hexene, for example, showed a loss of intensity for the low angle reflections, as these are known to be affected by the presence of molecules occluded in the pores (see figure 71).[190] This demonstrates the accessibility of the pores of the zeolite films, and the ability for molecules to be adsorbed and retained in the pores. Upon calcination to remove all of the organics and other molecules the intensities in the low angle region of the XRD pattern are regained correlating with the empty state of the pores.

Further evidence of the presence of accessible titanium sites within the pores comes from the study of Ti K-edge XANES, see figure 72. The pre-edge intensity of the calcined TS-1 films and that exposed to water were found to be similar, suggesting the hydrophobic nature of the films. Upon reaction of the TS-1 films with hydrogen peroxide, the intensity of the pre-edge feature decreased, indicating that the titanium centers are accessible and are available for reactions. SEM micrographs showed that these films were found to be unaffected after reaction with hydrogen peroxide. Recalcination of the reacted

films restored the pre-edge intensity in the Ti K-edge XANES and confirmed the regeneration of active sites (figure 72).

To demonstrate the generality of this method iron doped silicon dioxide films were also explored. As mentioned in the experimental section iron was incorporated into the silica matrix by mixing dopant amounts of ferrocene with TEOS during the CVD stage. These films were then converted to Fe-Silicalite by the standard procedure described above. Iron doped films were only deposited on alumina substrates to negate any ambiguity arising from silicon substrates during the conversion process of amorphous silica films to crystalline zeolite.[191] Figure 73 (a) shows the SEM image of amorphous iron doped silicon dioxide films deposited on alumina exhibiting the characteristic spherical particle morphology as seen with amorphous silicon dioxide and titanium doped silicon dioxide films. Figure 73 (b) shows the SEM image of Fe-Silicalite deposited on alumina. It is clear from the image that the crystals appear to be more randomly oriented than S-1 and TS-1 films deposited on alumina. The reason for this could be the increased synthesis time required for Fe-Silicalite films i.e. 48 hours as opposed to 24 hours leading to more random crystals. This random crystal orientation can be seen from the XRD pattern of Fe-Silicalite on alumina (figure 74).

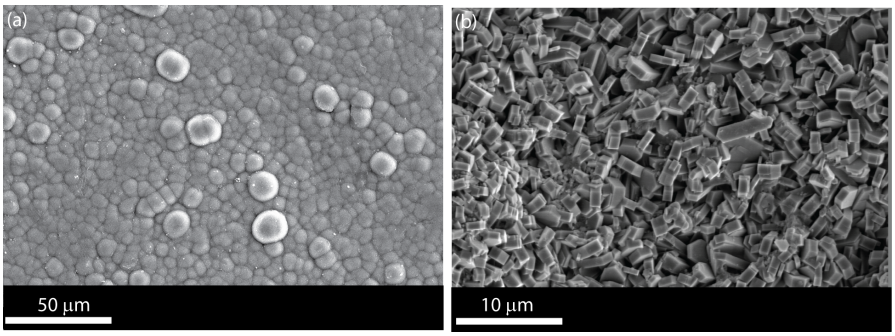

Figure 73: SEM images of (a) amorphous Fe-doped silicon dioxide film deposited on alumina and (b) Fe-Silicalite film deposited on alumina, note the more random distribution of preferred crystal orientation compared to TS-1 analogues. This could be due to the longer crystallisation time required for Fe-doped systems.

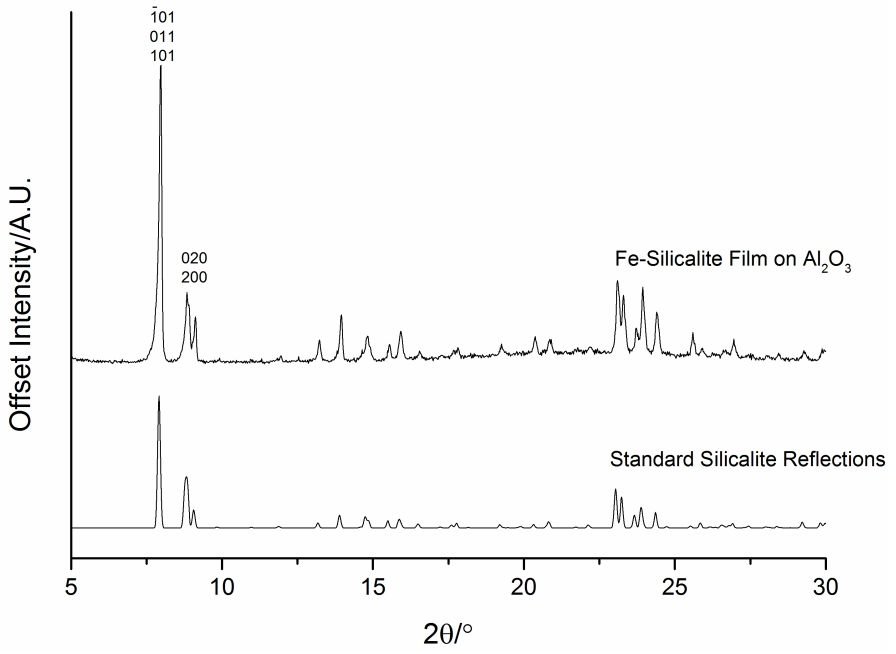

Figure 74: XRD pattern of Fe-Silicalite films deposited on alumina substrates.

The amorphous iron doped silicon dioxide films and Fe-Silicalite films were analysed by EDX to determine if iron was incorporated into the silicate and silicalite matrix. EDX analysis revealed the presence of iron in both the amorphous and zeolite films ca. 0.8 at.%. In order to determine the coordination around the iron centre in both the amorphous and zeolite films, XANES was performed on the samples in fluorescence mode (Fe K-edge). It is well-established that this pre-edge feature is intense for metal ions having tetrahedral coordination and least intense for octahedral coordination; the intensity also depends on the electronic structure of the metal ions in a given oxidation state, for eg. systems with d^0 state has highest intensity and therefore more pronounced for Ti(IV) compared to Fe(III).[192]

By comparing the XANES data of these systems with powder Fe ZSM-5 catalysts prepared by conventional methods, $FePO_4$ (Fe(III) ions in both these systems are in tetrahedral coordination) and Fe_2O_3 (Fe(III) ions are in octahedral coordination) systems, it can be said that iron is in the +3 oxidation state and in tetrahedral coordination. Thus it is clear from the XANES study that it is possible to produce Fe-Silicalite films containing isolated tetrahedrally coordinated metal ions in the silicalite matrix.

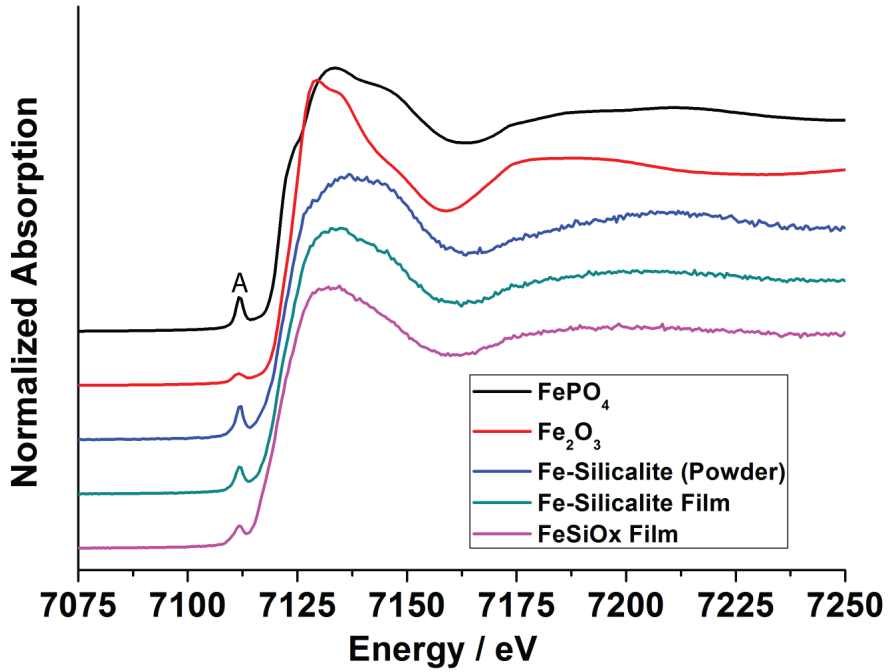

Figure 75: Fe K-edge XANES of various iron containing silicate films along with respective model systems are shown. (XANES data were recorded using fluorescence mode at B18 at the Diamond Light Source, which operates at 3 GeV with a typical current of ca 250 mA). The 1s-3d transition (pre-edge feature) is marked as A in the figure. The pre-edge feature intensity is highest when the metal ions are in tetrahedral geometry, $FePO_4$ in the case of iron systems). This intensity is lowest when these ions are surrounded by octahedral coordination, as seen in Fe_2O_3. Any deviation, in particular distorted geometry, will affect the intensity of this pre-edge feature.

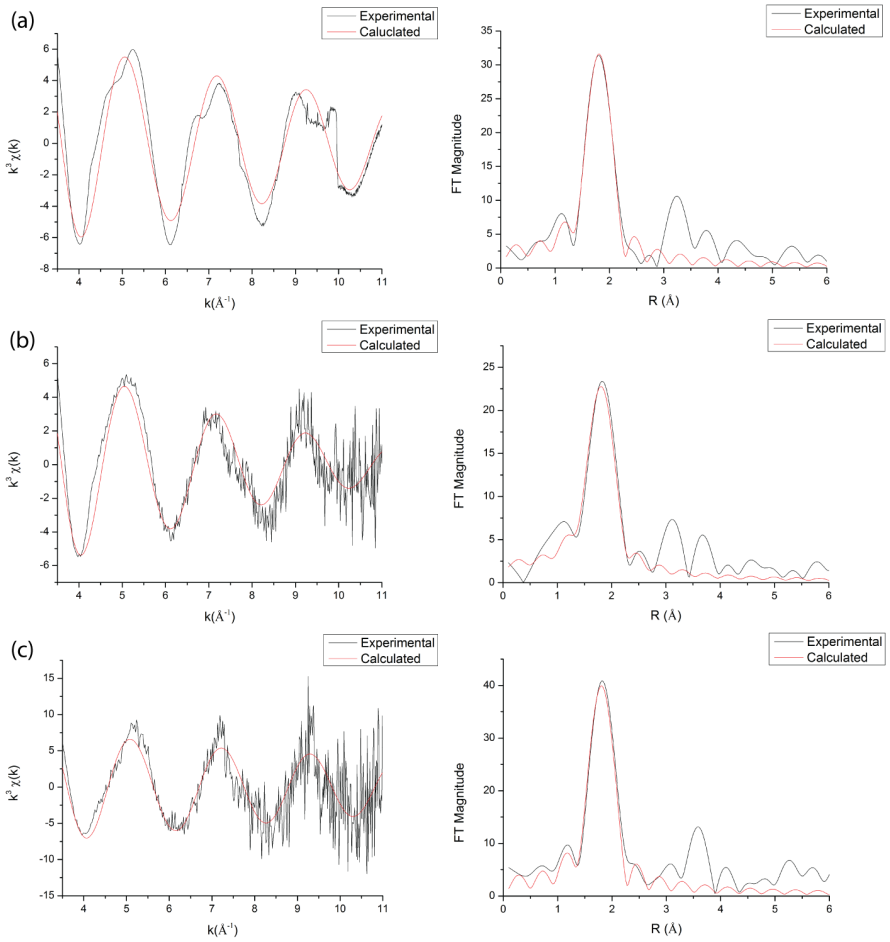

Figure 76: Fe K-edge EXAFS and associated Fourier transforms (FT) are given along with the calculated EXAFS and FT's for (a) $FePO_4$, (b) Fe-Silicalite film on alumina and (c) Fe-Silicalite powder sample synthesised by conventional hydrothermal methods.

Similarly, refinement of the EXAFS data revealed the Fe-O distances of $FePO_4$, Fe-Silicalite (powder sample prepared by conventional hydrothermal methods) and Fe-silicalite films were similar and shows an average Fe-O distance of ca 1.85 Å which is typical for a Fe(III) in tetrahedral coordination geometry; typical best fit between experimental Fe K-edge EXAFS data and the associated FT's are shown in figure 76.

5.4 CONCLUSIONS

A new method of of engineering dense zeolite films by combining the advantages of CVD processing and templated hydrothermal synthesis is presented in this chapter. More importantly, this method can

be readily used to produce zeolitic films containing metal ions in the framework sites, in such a way that these ions are accessible to reactants. Furthermore, the films produced by this method are shown to be hydrophobic in nature by Ti K edge XANES measurements. The scalable nature of the CVD process means that this method could provide a solution to many of the challenges in producing zeolite films for large-scale applications, in particular in the field of electronics, gas-separation, catalysis and corrosion science. The following chapter expands upon zeolite frameworks and explores metal-organic framework films synthesised in a similar fashion.

Chapter VI

METAL-ORGANIC FRAMEWORK FILMS

6

METAL-ORGANIC FRAMEWORK FILMS BY CVD AND SOLVOTHERMAL SYNTHESIS

The previous chapter discussed the synthesis of zeolite films from a combined CVD/HT route. To expand on this metal-organic framework (MOFs) films were also explored from a CVD/solvothermal approach. MOFs are a relatively new class of microporous materials which are a combination of organic/inorganic building blocks. The synthesis of MOF films has mirrored the synthesis of zeolitic films. As mentioned previously, the most direct method for depositing zeolitic films has been to use a colloidal suspension of zeolite powder particles, which are spin coated onto the desired substrate. The problems associated with this method are that the particles are not rigidly bound to the substrate but are loosely dispersed on the surface. Similar to the synythesis of zeolite films by CVD and HT methods, MOF films could be synthesized by depositing zinc oxide nanoparticulate films by CVD and subsequently converting them into MOF-5 films via a solvothermal (ST) procedure. These films could find application in gas storage due to their high porosity as well the possibility of introducing reactive groups into the pores as well as network flexibility (which allows for reversible adsorption) which are the main reasons why MOFs are emerging as competition to zeolites.

6.1 METAL-ORGANIC FRAMEWORK FILMS

Metal-organic frameworks (MOFs) are a relatively new class of microporous materials which are a combination of organic/inorganic building blocks.[76,193] They are not as stable as their inorganic congeners (microporous aluminosilicates and aluminophosphates), but can survive to temperatures above 200 °C, exhibit high crystallinity and very high surface areas. MOFs are essentially composed of metal oxide units with organic linkers separating the metal ions, this arrangement can often result in interesting structural topologies. Apart from the high porosity of MOFs (as shown in figure 77) the possibility of introducing reactive groups into the pores as well as network flex-

ibility (which allows for reversible adsorption) are the main reasons for which MOFs are preferred to zeolites in gas storage applications, among many others.[76,145,193,194] Other applications including catalysis, luminescence and fluorescent materials, and drug storage and delivery have also been demonstrated. MOFs are used in both their powder form and as continuous, thin porous membranes supported on solid substrates.

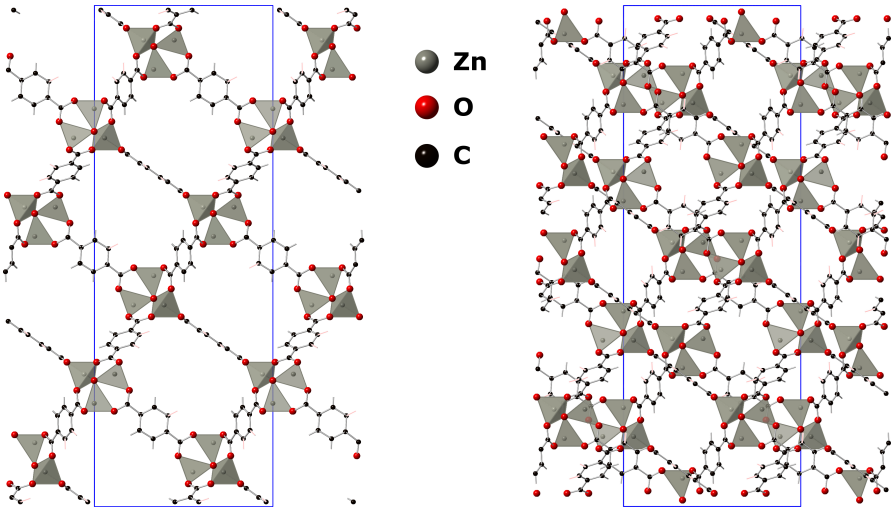

Figure 77: Crystal structures of MOF-5 (left) and interpenetrated MOF-5 (right). The Zn_4O_{13} tetrahedral clusters giving rise to the open framework structure are apparent. Note the pore size reduction wuth interpenetrated MOF.

These membranes have applications in optical coatings, catalysis, gas sensing and separation. The synthesis of MOF films has mirrored the synthesis of zeolitic films.[125–127,184,195] There are still problems however, and direct growth of zeolite-type materials on suitably functionalized supports is desirable, leading to more homogenous films and some control over crystal orientation within the film.[139,194,196] In the case of MOF films, an indirect approach of dispersing crystals onto a surface from a suspension of MOF crystals has been explored.[59,196] The problem however is that secure attachment of the MOF crystals to the surface still requires suitable functionalization in the form of self-assembled monolayers (SAMs).[76,197,198] However such surfaces are not transparent, limiting the use of MOF films in fluorescent/luminescent applications or photocatalysis.[184,199] Figure 77 shows the crystal structures of MOF-5 (left) and interpenetrated MOF-5 (right). The Zn_4O_{13} tetrahedral clusters giving rise to the open framework structure are apparent. Note the pore size re-

duction with interpenetrated MOF. The role of CVD with respect to microporous films has normally been to deliver and load the microporous films with metallic nanoparticles rather than to deposit a film which is essentially being used as a precursor.[200] By depositing zinc oxide nanoparticle films by CVD and subsequently converting them into MOF-5 films via a solvothermal procedure, MOF-5 films have been fabricated on glass substrates.[5,27,174,201] By dip-coating the ZnO films with a solution of H_2-bdc in DMF and suspending them inside an autoclave we were able to synthesise non-continuous films of cubic MOF-5 crystals that were well adhered to the underlying zinc oxide surface. The structural phase of MOF crystals produced and film coverage could be altered by submerging the zinc oxide nanoparticle films in the mother liquor, which yielded dense, continuous MOF/$Zn(OH)_2.0.5(H_2O)$ film.

6.2 EXPERIMENTAL

Zinc-2-ethyl hexanoate (20 ml) was added to acetone (80 ml) and/or toluene (80 ml). This mixture was stirred vigorously for 1 hour. The precursor solution was placed in a glass bubbler and an aerosol mist was created using a piezo-electric device. Zinc oxide depositions were carried out under nitrogen (99.99% from BOC). The metal precursor flow was kept at 0.6 L min-1. The substrate temperature was maintained at 550 °C and deposition time was 60 minutes. After the deposition the bubblers were closed and the substrates were cooled under a flow of nitrogen. At the end of the deposition the nitrogen flow through the aerosol was diverted and only nitrogen passed over the substrate. The glass substrate was allowed to cool to less than 100 °C before it was removed. Coated substrates were handled and stored in air. A schematic of the CVD set-up is shown in figure 78.

The cooled substrates were then coated with a 1.2 x 10^{-4} mol.cm^{-3} solution of H_2-bdc in DMF and transferred into a PTFE-lined stainless steel autoclave. Solvothermal reactions were performed at 100 °C for 24 hours. Products were then washed with DMF and stored in a vacuum desiccator. A schematic of the whole synthesis process is shown in figure 79.

X-ray diffraction (XRD) was used to analyse crystallinity of the samples with a Bruker D8 X-ray diffractometer with Cu$K\alpha_1$ and Cu$K\alpha_2$ radiation of wavelengths 1.54056 Å and 1.54439 Å respectively, emit-

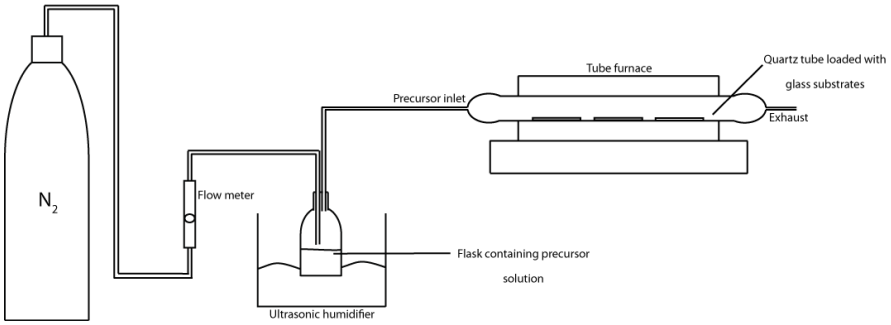

Figure 78: Schematic of AACVD apparatus used for deposition of zinc oxide films.

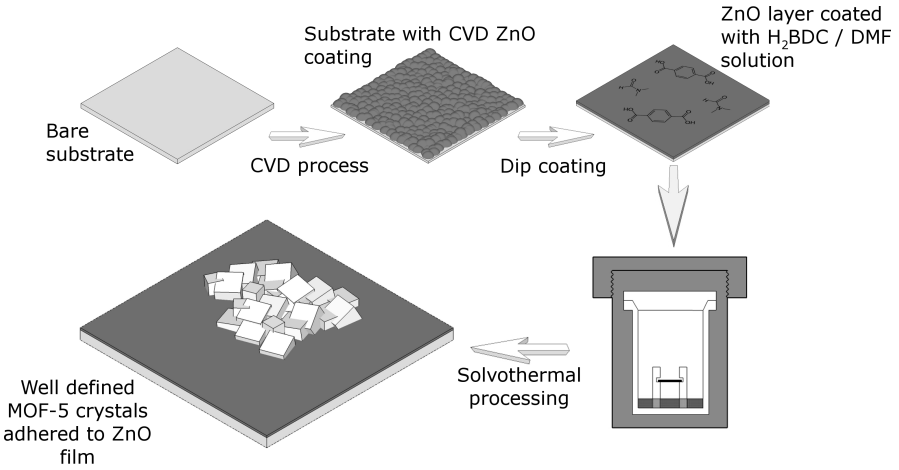

Figure 79: Schematic of the process of depositing ZnO films and their subsequent conversion into microporous MOF-5.

ted with an intensity ratio of 2:1, a voltage of 40 kV and current of 40 mA. The diffraction patterns were collected over an angular range of 6-38° 2ϑ. The Scherrer relation was used to determine the size of the zinc oxide crystallites deposited by CVD from the broadening of the Bragg peaks. The Scherrer relation was executed by running a corundum standard which exhibits no line broadening due to particle size. The data collected for the corundum standard was collected using identical scan conditions for those of the samples. The data for the samples and standard was then fitted to a Pseudo-Voigt peak shape and the instrumental broadening was removed using the Gaussian form of the Scherrer relation. Scanning Electron Microscopy (SEM) was performed to determine surface morphology and film thickness using a JEOL JSM-6301F Field Emission SEM at an accelerating voltage of 4-5 keV.

6.3 RESULTS AND DISCUSSION

Crystalline nano-zinc oxide films were deposited on glass substrates from zinc-2-ethyl hexanoate dissolved in acetone and toluene by aerosol assisted chemical vapour deposition. The crystalline zinc oxide films produced by CVD resulted in nano-sized spherical particles, ranging from 10-50 nm depending on the solvent used for deposition. Figure 80 shows SEM micrographs of the films synthesized from acetone resulted in particle size ~ 20 nm as shown from the SEM figures, in comparison to films synthesized from toluene, with particle size around 50 nm.

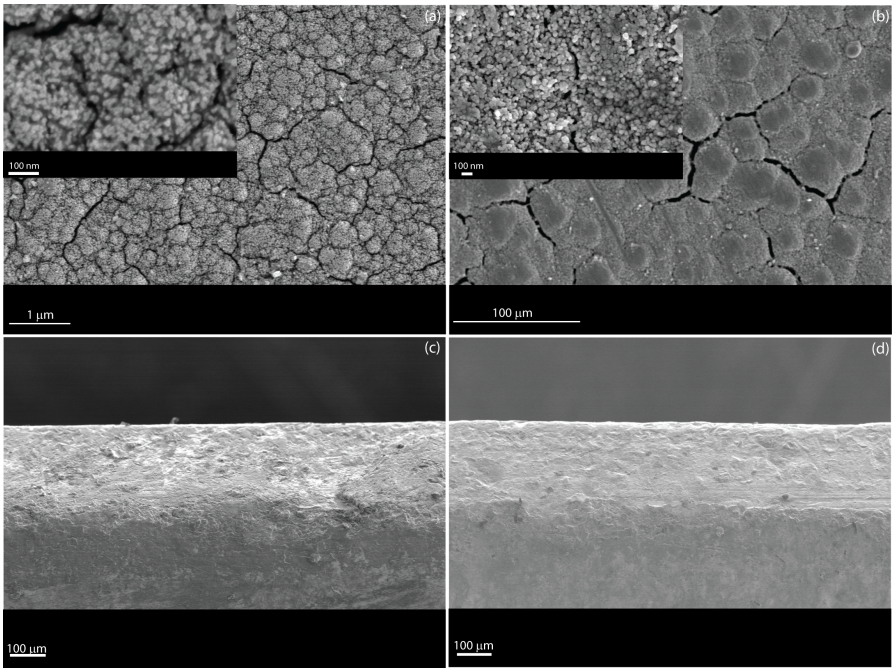

Figure 80: SEM micrographs of (a) zinc oxide film deposited from zinc-2-ethyl hexanoate in acetone (inset shows x140,000), (b) zinc oxide film deposited from zinc-2-ethyl hexanoate in toluene (inset shows x100,000), (c) Side-on SEM micrograph of zinc oxide film from acetone and (d) side-on SEM micrograph of zinc oxide film from toluene.

The smaller particle size of the films derived from acetone is possibly due to faster solvent evaporation as the aerosol enters the reaction chamber, in comparison to films derived from toluene. Figure 80(c) and (d) also shows the film thickness of the nano-zinc oxide films. Films derived from both acetone and toluene resulted in films ~ 160 µm thick. XRD was used to probe the crystallinity of the as-deposited CVD films. It is clear from figure 82 that the as-deposited

zinc oxide film was crystalline and the peaks could all be indexed to the zincite structure of zinc oxide. The XRD patterns also support the SEM micrographs, in which the particles appear to be nano-sized as there is significant peak broadening which can be attributed to the nano-scale nature of the crystallites. The Scherrer equation was used to determine the crystallite size and corroborate the particle size seen in figure 80.

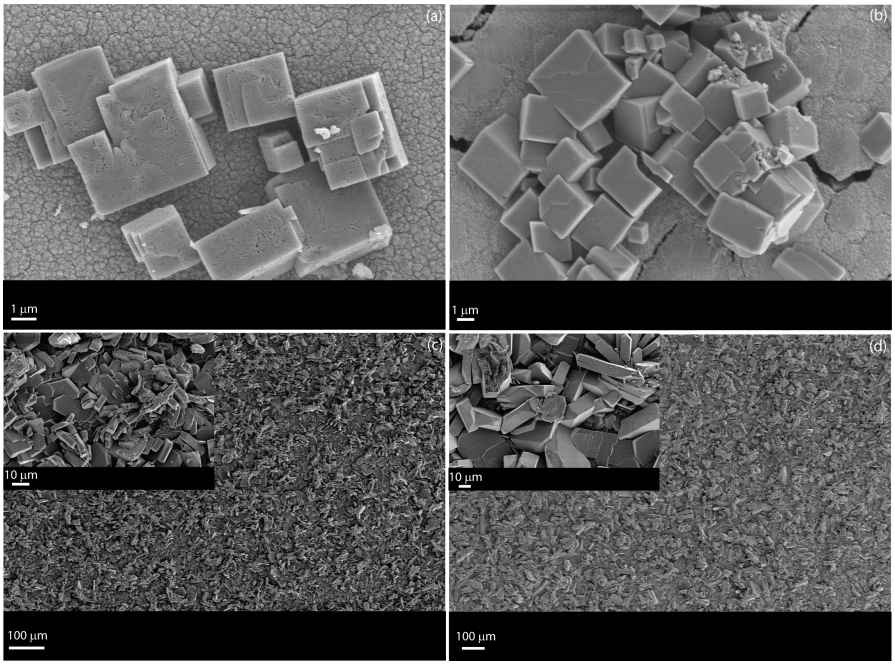

Figure 81: SEM micrographs of (a) dispersed MOF-5 crystallites that form from zinc oxide (deposited by AACVD from acetone) followed by dip coating with mother liquor and solvothermal work up, (b) dispersed MOF-5 crystallites that form from zinc oxide (deposited by AACVD from toluene) followed by dip coating with mother liquor and solvothermal work up, (c) interpenetrated (inset) MOF-5 film crystallites on zinc oxide (deposited by AACVD from acetone) by submerging in mother liquor under solvothermal conditions and (d) interpenetrated (inset) MOF-5 film crystallites on zinc oxide (deposited by AACVD from toluene) by submerging in mother liquor under solvothermal conditions.

The crystallite size of the ZnO particles was found to be 23 nm. This correlates to the particle size as determined by SEM analysis of the films. MOF-5 films were synthesized by solvothermal treatment of CVD grown crystalline nano-zinc oxide films on SiO_2, precoated (ca. 50 nm thick SiO_2 barrier layer) standard float glass (NSG, U.K.). Two methods of MOF film formation were developed. Dip coating of the ZnO films in the mother liquor resulted in dispersed crystals across the surface whereas submerging the ZnO films in the mother

liquor resulted in dense inter-grown films after solvothermal treatment. The films were white in color, passed the Scotch tape test and resisted scratching with various grades of pencil and brass but were removed by a steel scalpel. By dip coating the as-deposited zinc oxide films with a solution of H_2-bdc and DMF, the nano sized zinc oxide films could be converted into phase pure MOF-5 films. Figure 80(a) and (b) clearly shows cubic MOF-5 crystals formed from zinc oxide films. The resultant films were not dense and continuous and MOF-5 crystals are dispersed across the substrate. This is confirmed by the collected XRD data, which clearly shows the presence of phase pure MOF-5 in the dip-coated samples together with ZnO crystallites. The submerged samples show diffraction patterns consistent with the interpenetrated MOF-5 structure seen by Biemmi *et al.*[202] The intensity of the MOF-5 peak at ~ 6.5° is low in comparison to the simulated pattern as the solvent was not removed from the pores of the samples prior to X-ray analysis, this is consistent with the findings of Hafizovic *et al.*[190]

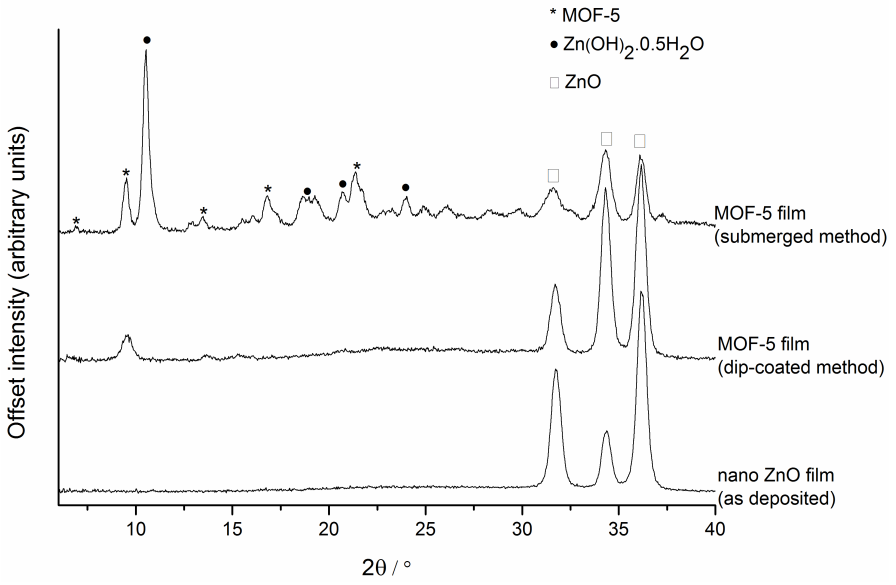

Figure 82: XRD patterns of as-deposited zinc oxide film (from acetone) on SiO_2 precoated standard float glass and conversion into phase pure MOF-5 film via dip coating and a mixed phase MOF via a submerged solvothermal method. Note that the zinc oxide peaks are still present after conversion into MOF. Peak positions related to MOF-5 and $Zn(OH)_2.0.5H_2O$ and ZnO underlayer are marked.

The underlying zinc oxide film can still be detected in all sample patterns as shown in figure 82. Figure 80(c) and (d) show dense, con-

tinuous and intergrown MOF films on soda lime glass substrates. The XRD patterns for films grown via the submerged method also show a $Zn(OH)_2.0.5H_2O$ phase. It is clear from the SEM micrographs of films grown via the submerged method (figure 80(c) and (d)) that the morphology of the crystals appears to be plate like and most likely a convolution of MOF and $Zn(OH)_2.0.5H_2O$ crystals.

6.4 CONCLUSIONS

Homogenous thick films of crystalline nano ZnO were deposited on glass substrates and subsequently converted into crystalline MOF-5. The methodology described in this chapter can enormously simplify the process of manufacturing MOF membranes by obviating the need for elaborate surface preparations that are currently required to immobilise MOF crystals on a surface. Modification of the solvothermal processing technique resulted in continuous films of interpenetrated MOF crystals rather than isolated clusters of the simpler MOF structure that was obtained with the vapour-phase transport method. This simplified method opens up the field of MOF film synthesis and allows for the field to grow in that thermal CVD can be replaced with plasma CVD, which permits deposition onto flexible substrates. Atomic layer deposition (ALD) can also be employed to deposit amorphous and crystalline oxide films to give excellent control over film thickness, which can then be converted to the desired MOF. Deposition onto conducting glass substrates could also allow for electrochemical applications of MOF films. This work provides another synthetic route to the synthesis of MOF films in addition to established routes such as surface functionalization with SAMs on gold surfaces and liquid phase epitaxy (LPE).

Chapter VII

CONCLUSIONS

7

CONCLUSIONS

7.1 SUMMARY OF RESULTS

Chapter 3 discussed the deposition of fluorine doped tin dioxide (FTO) films for the potential use as electrodes in PV devices and solar control coatings. Three CVD variants were compared. Collison-AACVD was shown to be a more effective and simple method for the deposition of fluorine doped tin dioxide films with excellent optical and electrical properties over films produced by APCVD, as well as films produced by ultrasonic-AACVD. This could be attributed to the fact that the droplets generated by this method are significantly smaller in diameter than those generated by an ultrasonic humidifier, resulting in shorter evaporation times, complete solute precipitation, and a size similar to the grains as seen by SEM. This work demonstrates a move towards tailoring functional properties of the films to specific applications, including transparent conducting materials for thin film photovoltaics, polymer devices and architectural glazing. Deposition temperatures of 450 °C for c-AACVD grown F:SnO_2 thin films were found to be optimum for use as low-emissivity coatings with a low visible light haze value (1.74%), a high charge carrier mobility (25 $cm^2/V.s$), high charge carrier density (5.7 x 10^{20} cm^{-3}), high transmittance across the visible (~ 80%) and a high reflectance in the IR (80% at 2500 nm). A deposition temperature of 500 °C was found to be optimum for the production of c-AACVD grown F:SnO_2 thin films for use as top electrodes in thin film photovoltaics giving a low sheet resistance (4 Ω/sq) and a surface texturing on the micrometer scale with a haze value of 8% for light scattering and trapping within thin film photovoltaic devices. It was also shown that AACVD and APCVD can be used to deposit highly conducting doped tin oxide films on high temperature resistant polymer coated steel. APCVD was developed to produce coatings with conductivities comparable to those of c-AACVD but at a fraction of the time as required by industry specifications of the layer properties, but reproducibility was an issue with APCVD derived films. AACVD derived films showed

sheet resistance values comparable to the APCVD derived films but the length of deposition was much longer.

Chapter 4 explored the synthesis of electrically conducting ZnO films and the prospect of incorporating cationic and anionic dopants into the ZnO structure to enhance opto-electronic properties. AACVD was shown to be an effective and simple method for the deposition of highly transparent and conductive zinc oxide, fluorine-doped zinc oxide and aluminium doped zinc oxide films. The unintentionally doped zinc oxide films discussed in this chapter displayed excellent optical and electrical properties comparable to coatings based on tin and indium oxides. These could be used as low-ε-coatings or electrodes in photovoltaics. Dopants could easily be incorporated into the system and this was shown by synthesizing fluorine doped zinc oxide and aluminium doped zinc oxide. Fluorine doped zinc oxide films displayed high transparency and excellent electrical characteristics. The surface morphology together with the opto-electronic properties makes this material ideal for PV applications requiring light trapping and scattering. Aluminium doped zinc oxide films also displayed high transparency with electrical properties suitable for PV applications requiring low haze and light scattering such as in DSSC. Control over the carrier mobility, charge-carrier density, IR reflectance, crystallinity and the surface morphology of the films have shown to be highly dependent upon dopant introduction using this technique.

The scope of the thesis took a new turn in chapter 5, concentrating on microporous metal oxide films, and moving away from TCO materials. Zeolite films were synthesised by developing a new combined chemical vapour deposition (CVD) and hydrothermal methods. A new method of of engineering dense zeolite films by combining the advantages of CVD processing and templated hydrothermal synthesis were presented in this chapter. The method developed can be readily used to produce zeolitic films containing metal ions in the framework sites, in such a way that these ions were accessible to reactants, i.e. presented the scope for catalysis. Furthermore, the films produced by this method are shown to be hydrophobic in nature by Ti and Fe K edge XANES measurements. The scalable nature of the CVD process means that this method could provide a solution to many of the challenges in producing zeolite films for large-scale applications, in particular in the field of electronics, gas-separation, catalysis and corrosion science.

Chapter 6 expanded on the methods described in chapter 5 and demonstrated the generality of the methods developed in chapter 6. The standard progression from zeolite film synthesis was metal-organic framework film synthesis. Homogenous thick films of crystalline nano ZnO were deposited on glass substrates and subsequently converted into crystalline MOF-5. This is the first time that an immobilised dense oxide phase as a film has been converted into a crystalline MOF material. Such methodology can enormously simplify the process of manufacturing MOF membranes by obviating the need for elaborate surface preparations that are currently required to immobilise MOF crystals on a surface. Modification of the solvothermal processing technique resulted in continuous films of interpenetrated MOF crystals rather than isolated clusters of the simpler MOF structure that was obtained with the vapour-phase transport method. This simplified method opens up the field of MOF film synthesis and allows for the field to grow in that thermal CVD can be replaced with plasma CVD, which permits deposition into flexible substrates. Atomic layer deposition (ALD) could also be employed to deposit amorphous and crystalline oxide films to give excellent control over film thickness, which can then be converted to the desired MOF. Deposition onto conducting glass substrates also allows for opto-electronic and electrochemical applications. This work provides another synthetic route to the synthesis of MOF films in addition to established routes such as surface functionalization with SAMs on gold surfaces and liquid phase epitaxy (LPE).

Chapter VIII

APPENDIX

BIBLIOGRAPHY

[1] Choy KL. Chemical vapour deposition of coatings. Progress in Materials Science. 2003;48(2):57–170. Doi: DOI: 10.1016/S0079-6425(01)00009-3. (Cited on pages 4, 5, 8, 9, 10, 15, 18, 79, 89, and 112.)

[2] Crick CR. CVD of copper and copper oxide thin films via the in situ reduction of copper(ii) nitrate—a route to conformal superhydrophobic coatings. Journal of Materials Chemistry. 2011;21(38):14712. Available from: http://xlink.rsc.org/?DOI=c1jm11955a. (Cited on page 5.)

[3] Kaufmann T, Fuchs G, Webert M, Frieske S, Gäckle M. MOCVD layer growth of ZnO using adducts of dimethyl- and diethylzinc. Crystal Research and Technology. 1989 Mar;24(3):269–274. Available from: http://doi.wiley.com/10.1002/crat.2170240306.

[4] Kodas T, Hampden-Smith M. The Chemistry of Metal CVD. VCH;. (Cited on pages 6, 10, 11, 12, and 18.)

[5] McCurdy RJ. Successful implementation methods of atmospheric CVD on a glass manufacturing line. Thin Solid Films. 1999 Aug;351(1–2):66–72. Available from: http://www.sciencedirect.com/science/article/pii/S0040609099001996. (Cited on pages 6, 129, and 151.)

[6] Rees WS. CVD of Non-Metals. 1st ed. VCH;. (Cited on pages 4 and 134.)

[7] Brinker CJ, Scherer GW. Sol-Gel Science. Elsevier;. (Cited on page 5.)

[8] Hench LL, West JK. The sol-gel process. Chemical Reviews. 1990 Jan;90(1):33–72. Available from: http://pubs.acs.org/doi/abs/10.1021/cr00099a003.

[9] Keita Kakiuchi TKHI Eiji Hosono, Fujihara S. Fabrication of mesoporous ZnO nanosheets from precursor templates grown

in aqueous solutions. Journal of Sol-Gel Science and Technology. 2006;39(1):63. (Cited on pages 5 and 55.)

[10] Kong YC, Yu DP, Zhang B, Fang W, Feng SQ. Ultraviolet-emitting ZnO nanowires synthesized by a physical vapor deposition approach. Applied Physics Letters. 2001;78(4):407. Available from: http://link.aip.org/link/APPLAB/v78/i4/p407/s1&Agg=doi. (Cited on page 5.)

[11] Lyu SC, Zhang Y, Lee CJ, Ruh H, Lee HJ. Low-Temperature Growth of ZnO Nanowire Array by a Simple Physical Vapor-Deposition Method. Chemistry of Materials. 2003 Aug;15(17):3294–3299. Available from: http://pubs.acs.org/doi/abs/10.1021/cm020465j. (Cited on page 5.)

[12] Kurdesau F, Khripunov G, da Cunha A, Kaelin M, Tiwari A. Comparative study of ITO layers deposited by DC and RF magnetron sputtering at room temperature. Journal of Non-Crystalline Solids. 2006 Jun;352(9-20):1466–1470. Available from: http://linkinghub.elsevier.com/retrieve/pii/S002230930600113X. (Cited on page 5.)

[13] Nanto H, Minami T, Shooji S, Takata S. Electrical and optical properties of zinc oxide thin films prepared by rf magnetron sputtering for transparent electrode applications. Journal of Applied Physics. 1984;55(4):1029. Available from: http://link.aip.org/link/JAPIAU/v55/i4/p1029/s1&Agg=doi. (Cited on page 43.)

[14] Tadatsugu M. Present status of transparent conducting oxide thin-film development for Indium-Tin-Oxide (ITO) substitutes. Thin Solid Films. 2008 Jul;516(17):5822–5828. Available from: http://www.sciencedirect.com/science/article/pii/S004060900701694X. (Cited on pages 5 and 111.)

[15] Crick CR, Parkin IP. Water droplet bouncing—a definition for superhydrophobic surfaces. Chemical Communications. 2011;47(44):12059. Available from: http://xlink.rsc.org/?DOI=c1cc14749h. (Cited on page 5.)

[16] Jones A, Hitchman M, Krumdieck S. Chemical Vapour Deposition. Jones A, Hitchman M, editors. RSC; 2009. (Cited on pages 5, 8, 9, 10, 14, 15, and 18.)

[17] Kodas T, Hampden-Smith M. Aerosol Processing of Materials. Wiley-VCH:New York; 1999. (Cited on pages 6, 10, 11, 12, 18, 19, and 80.)

[18] Hu YH, Zhang L. Amorphization of metal-organic framework MOF-5 at unusually low applied pressure. Physical Review B. 2010 May;81(17). Available from: http://link.aps.org/doi/10.1103/PhysRevB.81.174103. (Cited on page 7.)

[19] Jensen KF. Modeling and Analysis of Low Pressure CVD Reactors. Journal of The Electrochemical Society. 1983;130(9):1950. Available from: http://jes.ecsdl.org/cgi/doi/10.1149/1.2120129.

[20] Potts SE, Carmalt CJ, Blackman CS, Abou-Chahine F, Pugh D, Davies HO. Synthesis of Zirconium Guanidinate Complexes and the Formation of Zirconium Carbonitride via Low Pressure CVD. Organometallics. 2009 Mar;28(6):1838–1844. Available from: http://pubs.acs.org/doi/abs/10.1021/om801053y. (Cited on page 7.)

[21] Blackman CS, Correig X, Katko V, Mozalev A, Parkin IP, Alcubilla R, et al. Templated growth of tungsten oxide micro/-nanostructures using aerosol assisted chemical vapour deposition. Materials Letters. 2008;62:4582–4584. (Cited on pages 7 and 38.)

[22] Hickey A. Pharmaceutical inhalation aerosol technology. Dekker, M.; 2004. (Cited on pages 10, 11, 12, 18, and 19.)

[23] Knapp CE, Hyett G, Parkin IP, Carmalt CJ. Aerosol-Assisted Chemical Vapor Deposition of Transparent Conductive Gallium-Indium-Oxide Films. Chemistry of Materials. 2011 Apr;23(7):1719–1726. Available from: http://pubs.acs.org/doi/abs/10.1021/cm102292b. (Cited on page 111.)

[24] Mädler L, Kammler H, Mueller R, Pratsinis S. Controlled synthesis of nanostructured particles by flame spray pyrolysis. Journal of Aerosol Science. 2002 Feb;33(2):369–389. Available from: http://linkinghub.elsevier.com/retrieve/pii/S0021850201001598.

[25] Piccirillo C, Binions R, Parkin I. Synthesis and characterisation of W-doped VO2 by Aerosol Assisted Chemical Vapour Deposition. Thin Solid Films. 2009;516:1992–1997. (Cited on pages 38 and 39.)

[26] Viguie JC, Spitz J. Chemical Vapor Deposition at Low Temperatures. Journal of The Electrochemical Society. 1975;122(4):585–588.

[27] Waugh MR, Hyett G, Parkin IP. Zinc Oxide Thin Films Grown by Aerosol Assisted CVD. Chemical Vapor Deposition. 2008 Nov;14(11-12):366–372. Available from: http://doi.wiley.com/10.1002/cvde.200806718. (Cited on pages 7, 43, 112, and 151.)

[28] Palgrave R. Chemical Vapour Deposition of Nanoparticulate and Nanocomposite Thin Films. UCL; 2007. (Cited on pages 12, 13, 14, and 70.)

[29] Palgrave RG, Parkin IP. Aerosol Assisted Chemical Vapor Deposition Using Nanoparticle Precursors: A Route to Nanocomposite Thin Films. J Am Chem Soc. 2006;128(5):1587–1597. Available from: http://dx.doi.org/10.1021/ja055563v. (Cited on pages 19, 38, 79, and 129.)

[30] Ãgoston P, Albe K, Nieminen RM, Puska MJ. Intrinsic n-type behavior in transparent conducting oxides: A comparative hybrid-functional study of In2O3, SnO2, and ZnO. Physical Review Letters. 2009;103(24). Export Date: 21 April 2010 Source: Scopus Art. No.: 245501. (Cited on pages 22, 43, 78, and 111.)

[31] Edwards PP, Porch A, Jones MO, Morgan DV, Perks RM. Basic materials physics of transparent conducting oxides. Dalton Transactions. 2004;(19):2995. Available from: http://xlink.rsc.org/?DOI=b408864f. (Cited on page 22.)

[32] Adamopoulos G, Bashir A, Gillin WP, Georgakopoulos S, Shkunov M, Baklar MA, et al. Structural and Electrical Characterization of ZnO Films Grown by Spray Pyrolysis and Their Application in Thin-Film Transistors. Advanced Functional Materials. 2011;21(3):525–531. Available from: http://dx.doi.org/10.1002/adfm.201001089. (Cited on pages 22, 43, and 55.)

[33] Afify HH, Terra FS, Momtaz RS. Substrate temperature effects on the tin oxide films prepared by spray pyrolysis. Journal of Materials Science: Materials in Electronics. 1996;7(2):149–153. 10.1007/BF00225638. (Cited on pages 23 and 86.)

[34] Catlow CRA, Sokol AA, Walsh A. Microscopic origins of electron and hole stability in ZnO. Chemical Communications. 2011;47(12):3386. Available from: http://xlink.rsc.org/?DOI=c1cc10314h. (Cited on pages 43, 110, and 112.)

[35] Hutson A. Hall Effect Studies of Doped Zinc Oxide Single Crystals. Physical Review. 1957 Oct;108(2):222–230. Available from: http://link.aps.org/doi/10.1103/PhysRev.108.222. (Cited on pages 22, 34, 35, and 55.)

[36] Ginley DS, Bright C. Transparent Conducting Oxides. MRS Bulletin. 2011 Nov;25(08):15–18. Available from: http://www.journals.cambridge.org/abstract_S0883769400028876. (Cited on page 22.)

[37] Goldner RB, Haskal HM. Indium tin oxide-coated silicon as a selective absorber. Applied Optics. 1975 Oct;14(10):2328. Available from: http://www.opticsinfobase.org/abstract.cfm?URI=ao-14-10-2328.

[38] Minami T. New n-Type Transparent Conducting Oxides. MRS Bulletin. 2011 Jan;25(08):38–44. Available from: http://www.journals.cambridge.org/abstract_S0883769400027159. (Cited on page 22.)

[39] Ashcroft NW, Mermin ND. Solid State Physics. 1st ed. HRW;. (Cited on pages 22, 26, and 28.)

[40] Burns G. Solid State Physics. Academic Press, Inc.;. (Cited on pages 22, 26, 27, 28, and 29.)

[41] Kawazoe H, Yasukawa M, Hyodo H, Kurita M, Yanagi H, Hosono H. P-type electrical conduction in transparent thin films of CuAlO2. Nature. 1997 Oct;389(6654):939–942. Available from: http://dx.doi.org/10.1038/40087. (Cited on pages 22 and 23.)

[42] Beyer W, Hupkes J, Stiebig H. Transparent conducting oxide films for thin film silicon photovoltaics. Thin Solid Films.

2007;516(2-4):147–154. Doi: DOI: 10.1016/j.tsf.2007.08.110. (Cited on pages 22, 40, 41, and 43.)

[43] Mryasov O, Freeman A. Electronic band structure of indium tin oxide and criteria for transparent conducting behavior. Physical Review B. 2001 Dec;64(23). Available from: http://link.aps.org/doi/10.1103/PhysRevB.64.233111. (Cited on page 22.)

[44] Coutts TJ, Young DL, Li X. Characterization of Transparent Conducting Oxides. MRS Bulletin. 2011 Jan;25(08):58–65. Available from: http://www.journals.cambridge.org/abstract_S0883769400027184. (Cited on page 23.)

[45] Fortunato E, Ginley D, Hosono H, Paine DC. Transparent Conducting Oxides for Photovoltaics. MRS Bulletin. 2011 Jan;32(03):242–247. Available from: http://www.journals.cambridge.org/abstract_S088376940000693X.

[46] Freeman AJ, Poeppelmeier KR, Mason TO, Chang RPH, Marks TJ. Chemical and Thin-Film Strategies for New Transparent Conducting Oxides. MRS Bulletin. 2011 Jan;25(08):45–51. Available from: http://www.journals.cambridge.org/abstract_S0883769400027160.

[47] Islam MN, Ghosh T, Chopra K, Acharya H. XPS and X-ray diffraction studies of aluminum-doped zinc oxide transparent conducting films. Thin Solid Films. 1996 Jul;280(1-2):20–25. Available from: http://linkinghub.elsevier.com/retrieve/pii/0040609095082395. (Cited on page 23.)

[48] Bhachu DS, Waugh MR, Zeissler K, Branford WR, Parkin IP. Textured Fluorine-Doped Tin Dioxide Films formed by Chemical Vapour Deposition. Chemistry - A European Journal. 2011 Oct;17(41):11613–11621. Available from: http://doi.wiley.com/10.1002/chem.201100399. (Cited on pages 23, 41, 111, and 129.)

[49] Hu J, Gordon RG. Textured aluminum-doped zinc oxide thin films from atmospheric pressure chemical-vapor deposition. Journal of Applied Physics. 1992;71(2):880. Available from: http://link.aip.org/link/JAPIAU/v71/i2/p880/s1&Agg=doi. (Cited on page 112.)

[50] Liang H, Gordon RG. Atmospheric pressure chemical vapor deposition of transparent conducting films of fluorine doped zinc oxide and their application to amorphous silicon solar cells. Journal of Materials Science. 2007 Apr;42(15):6388–6399. Available from: http://www.springerlink.com/index/10.1007/s10853-006-1255-5.

[51] Mayer B. Highly conductive and transparent films of tin and fluorine doped indium oxide produced by APCVD. Thin Solid Films. 1992;221(1-2):166–182. Doi: DOI: 10.1016/0040-6090(92)90811-O. (Cited on page 23.)

[52] Remes Z, Vanecek M, Yates H, Evans P, Sheel D. Optical properties of SnO2:F films deposited by atmospheric pressure CVD. Thin Solid Films. 2009;517:6287–6289. (Cited on pages 23 and 79.)

[53] Sheel D, Yates H, Evans P, Dagkaldiran U, Gordijn A, Finger F, et al. Atmospheric pressure chemical vapour deposition of F doped SnO2 for optimum performance solar cells. Thin Solid Films. 2009;517:3061–3065. (Cited on page 79.)

[54] Yates H, Evans P, Sheel D, Heessels A, Ammerlaan J, Dagkaldiran ü, et al. Deposition of thin film SnO2:F onto aluminium foil for use in flexible tandem solar cells. Thin Solid Films. 2011 Sep;519(22):7731–7737. Available from: http://linkinghub.elsevier.com/retrieve/pii/S004060901101234X. (Cited on page 23.)

[55] Gratzel M. Dye-Sensitized solar cells. Jornal of Photochemistry and Photobiology. 2003;4:145–153. (Cited on pages 23, 40, 51, 78, and 111.)

[56] Gratzel M. Solar Energy Conversion by Dye-Sensitized Photovoltaic Cells. Inorganic Chemistry. 2005;44(20):6841–6851. (Cited on pages 23, 51, 78, and 111.)

[57] O'Regan B, Durrant J. Kinetic and Energetic Paradigms for Dye-Sensitized Solar Cells: Moving from the Ideal to the Real. Accounts of Chemical Research. 2009;42:1799–1808. (Cited on pages 52, 53, and 54.)

[58] O'Regan B, Grätzel M. A low-cost, high-efficiency solar cell based on dye-sensitized colloidal TiO2 films. Nature. 1991

Oct;353(6346):737–740. Available from: http://www.nature.com/doifinder/10.1038/353737a0. (Cited on pages 23, 40, 50, and 51.)

[59] Chen B, Wang X, Zhang Q, Xi X, Cai J, Qi H, et al. Synthesis and characterization of the interpenetrated MOF-5. Journal of Materials Chemistry. 2010;20(18):3758. Available from: http://xlink.rsc.org/?DOI=b922528e. (Cited on pages 23, 128, and 150.)

[60] Hara K, Arakawa H. Dye-sensitized Solar Cells. Luque A, Hegedus S, editors. John Wiley and Sons; 2003. (Cited on pages 23, 41, 45, 78, and 111.)

[61] Hoffmann R. Solids and Surfaces: Chemist's View of Bonding in Extended Structures. Wiley-VCH:New York;. (Cited on pages 24, 26, and 27.)

[62] Birkholz M. Thin Film Analysis by X-Ray Scattering. Wiley-VCH:Weinheim; 2006. (Cited on page 24.)

[63] Hartnagel HL, Dawar AL, Jain AK, Jagadish C. Semiconducting Transparent Thin Films. IOP Publishing Ltd; 1995. (Cited on pages 24, 29, 31, 36, 38, 39, 41, 78, 91, and 110.)

[64] Hamnett A. Solid State Chemistry. Cheetham A, Day P, editors. Oxford; 1988. (Cited on pages 26, 28, 30, 31, 34, and 66.)

[65] Rosenberg H. The Solid State. 3rd ed. Oxford Science Publications;.

[66] West AR. Basic Solid State Chemistry. 2nd ed. John Wiley & Sons Ltd;. (Cited on page 26.)

[67] Drude P. Zur Elektronentheorie der metalle. Annalen der Physik. 1900;306:566–613. (Cited on pages 27, 35, and 36.)

[68] Drude P. Zur Elektronentheorie der Metalle; II. Teil. Galvanomagnetische und thermomagnetische Effecte. Annalen der Physik. 1900;308(11):369–402. Available from: http://doi.wiley.com/10.1002/andp.19003081102. (Cited on pages 27 and 36.)

[69] Pauw Lvd. A method of measuring the resistivity and Hall coefficient on lamellae of arbitrary shape. Philips Technical Review. 1958;20:220–224. (Cited on pages 32, 34, and 114.)

[70] Orton JW, Powell MJ. The Hall effect in polycrystalline and powdered semiconductors. Reports on Progress in Physics. 1980 Nov;43(11):1263–1307. Available from: http://stacks.iop.org/0034-4885/43/i=11/a=001?key=crossref.2dcb10171a45e23e2547ed93360861b0. (Cited on pages 34 and 55.)

[71] Granqvist CG. Transparent conductors as solar energy materials: A panoramic review. Solar Energy Materials and Solar Cells. 2007;91(17):1529–1598. Doi: DOI: 10.1016/j.solmat.2007.04.031. (Cited on pages 35, 36, 89, 96, 111, and 124.)

[72] Pasquarelli RM, Ginley DS, O'Hayre R. Solution processing of transparent conductors: from flask to film. Chem Soc Rev. 2011;40(11):5406–5441. Available from: http://dx.doi.org/10.1039/C1CS15065K. (Cited on page 36.)

[73] Waugh MR. The Synthesis, Characterisation and Application of Transparent Conducting Thin Films. UCL; 2011. (Cited on pages 36 and 70.)

[74] Agashe C, Hupkes J, Schope G, Berginski M. Physical properties of highly oriented spray-deposited fluorine-doped tin dioxide films as transparent conductor. Solar Energy Materials and Solar Cells. 2009;93(8):1256–1262. Doi: DOI: 10.1016/j.solmat.2009.01.021. (Cited on pages 38, 40, and 86.)

[75] O'Brien S, Nolan MG, Çopuroglu M, Hamilton JA, Povey I, Pereira L, et al. Zinc oxide thin films: Characterization and potential applications. Thin Solid Films. 2010 Jun;518(16):4515–4519. Available from: http://linkinghub.elsevier.com/retrieve/pii/S0040609009020021. (Cited on page 112.)

[76] O'Keeffe M, Eddaoudi M, Li H, Reineke T, Yaghi O. Frameworks for Extended Solids: Geometrical Design Principles. Journal of Solid State Chemistry. 2000 Jun;152(1):3–20. Available from: http://linkinghub.elsevier.com/retrieve/pii/S0022459600987231. (Cited on pages 149 and 150.)

[77] Parkin I, Manning T. Intelligent thermochromic windows. Journal of Chemical Education. 2006;83:393–400.

[78] Saeli M, Piccirillo C, Parkin I, Ridley I, Binions R. Nano-composite thermochromic thin films and their application in energy-efficient glazing. Solar Energy Materials and Solar Cells. 2010;94:141–151. (Cited on pages 38, 39, and 79.)

[79] Eicker U. Solar Technologies for Buildings. John Wiley and Sons;. (Cited on page 40.)

[80] Smestad G. Testing of dye sensitized TiO2 solar cells II: Theoretical voltage output and photoluminescence efficiencies. Solar Energy Materials and Solar Cells. 1994;32(3):273–288. Doi: DOI: 10.1016/0927-0248(94)90264-X. (Cited on pages 41, 44, 45, 51, and 52.)

[81] Kim SS, Na SI, Jo J, Tae G, Kim DY. Efficient Polymer Solar Cells Fabricated by Simple Brush Painting. Advanced Materials. 2007 Dec;19(24):4410–4415. Available from: http://doi.wiley.com/10.1002/adma.200702040. (Cited on page 41.)

[82] Kim YG, Walker J, Samuelson LA, Kumar J. Efficient Light Harvesting Polymers for Nanocrystalline TiO 2 Photovoltaic Cells †. Nano Letters. 2003 Apr;3(4):523–525. Available from: http://pubs.acs.org/doi/abs/10.1021/nl0259535. (Cited on page 55.)

[83] Kitagawa S, Kitaura R, Noro Si. Functional Porous Coordination Polymers. Angewandte Chemie International Edition. 2004 Apr;43(18):2334–2375. Available from: http://doi.wiley.com/10.1002/anie.200300610. (Cited on page 41.)

[84] Cachet H. Films and powders of fluorine-doped tin oxide. In: Nakajima T, Groult H, editors. Fluorinated Materials for Energy Conversion. Elsevier Ltd.; 2005. p. 513–548. (Cited on pages 41, 42, 91, and 93.)

[85] Gerhardinger P, Strickler D. Fluorine Doped Tin Oxide Coatings - Over 50 Years and Going Strong. Key Engineering Materials. 2008;380:169–178. Available from: http://www.scientific.net/KEM.380.169. (Cited on page 41.)

[86] Lin CC, Chiang MC, Chen YW. Temperature dependence of Fluorine-doped tin oxide films produced by ultrasonic spray pyrolysis. Thin Solid Films. 2009;518(4):1241–1244. Doi: DOI: 10.1016/j.tsf.2009.05.064. (Cited on page 96.)

[87] Minami T. Transparent conducting oxide semiconductors for transparent electrodes. Semiconductor Science and Technology. 2005 Apr;20(4):S35–S44. Available from: http://stacks.iop.org/0268-1242/20/i=4/a=004?key=crossref.e6f7dab691bdff9f2777bb4a2c7d8694. (Cited on page 110.)

[88] Tin Markets for Photovoltaics. NanoMarkets. 2009;. (Cited on pages 41 and 79.)

[89] Gordon RG. Criteria for Choosing Transparent Conductors. MRS Bulletin. 2011 Jan;25(08):52–57. Available from: http://www.journals.cambridge.org/abstract_S0883769400027172. (Cited on pages 41 and 43.)

[90] van Mol A, Chae Y, McDaniel A, Allendorf M. Chemical vapor deposition of tin oxide: Fundamentals and applications. Thin Solid Films. 2006 Apr;502(1-2):72–78. Available from: http://linkinghub.elsevier.com/retrieve/pii/S0040609005011132. (Cited on page 41.)

[91] Belanger D, Dodelet JP, Lombos BA, Dickson JI. Thickness Dependence of Transport Properties of Doped Polycrystalline Tin Oxide Films. Journal of The Electrochemical Society. 1985;132(6):1398–1405. (Cited on pages 42, 86, and 87.)

[92] Berginski M, Hupkes J, Schulte M, Schope G, Stiebig H, Lech B, et al. The effect of front ZnO:Al surface texture and optical transparency on efficient light trapping in silicon thin-film solar cells. Journal of Applied Physics. 2007;101(7):074903.

[93] Martínez AI, Huerta L, León JMORd, Acosta D, Malik O, Aguilar M. Physicochemical characteristics of fluorine doped tin oxide films. Journal of Physics D: Applied Physics. 2006 Dec;39(23):5091–5096. Available from: http://stacks.iop.org/0022-3727/39/i=23/a=029?key=crossref.29c80d7e92a7017843737e408bdd0a2e. (Cited on pages 42, 55, and 88.)

[94] Karber C, Ãgoston P, Klein A. Surface and bulk properties of sputter deposited undoped and Sb-doped SnO_2 thin films. Sensors and Actuators, B: Chemical. 2009;139(2):665–672. Cited

By (since 1996): 2 Export Date: 21 April 2010 Source: Scopus. (Cited on page 42.)

[95] Hadipour A, de Boer B, Blom PWM. Organic Tandem and Multi-Junction Solar Cells. Advanced Functional Materials. 2008 Jan;18(2):169–181. Available from: http://doi.wiley.com/10.1002/adfm.200700517. (Cited on page 43.)

[96] Schmidt-Mende L, MacManus-Driscoll JL. ZnO – nanostructures, defects, and devices. Materials Today. 2007 May;10(5):40–48. Available from: http://linkinghub.elsevier.com/retrieve/pii/S1369702107700780. (Cited on pages 43 and 55.)

[97] Walters G, Parkin IP. Aerosol assisted chemical vapour deposition of ZnO films on glass with noble metal and p-type dopants; use of dopants to influence preferred orientation. Applied Surface Science. 2009;255(13-14):6555–6560. Doi: DOI: 10.1016/j.apsusc.2009.02.039. (Cited on page 43.)

[98] Hideo H. Recent progress in transparent oxide semiconductors: Materials and device application. Thin Solid Films. 2007 May;515(15):6000–6014. Available from: http://www.sciencedirect.com/science/article/pii/S0040609006015677. (Cited on pages 43 and 110.)

[99] Jenkinson DS, Adams DE, Wild A. Model estimates of CO2 emissions from soil in response to global warming. Nature. 1991 May;351(6324):304–306. Available from: http://www.nature.com/doifinder/10.1038/351304a0. (Cited on page 44.)

[100] Williams R. Becquerel Photovoltaic Effect in Binary Compounds. The Journal of Chemical Physics. 1960;32(5):1505. Available from: http://link.aip.org/link/JCPSA6/v32/i5/p1505/s1&Agg=doi. (Cited on pages 44 and 45.)

[101] Chapin DM, Fuller CS, Pearson GL. A New Silicon p-n Junction Photocell for Converting Solar Radiation into Electrical Power. Journal of Applied Physics. 1954;25(5):676–677. (Cited on page 45.)

[102] Gray JL. The physics of the solar cell. John Wiley & Sons Ltd; 2003. (Cited on pages 45, 46, 47, 48, and 49.)

[103] Miles RW, Hynes KM, Forbes I. Photovoltaic solar cells: An overview of state-of-the-art cell development and environmental issues. Progress in Crystal Growth and Characterization of Materials. 2005;51(1-3):1–42. Doi: DOI: 10.1016/j.pcrysgrow.2005.10.002. (Cited on pages 45 and 48.)

[104] Uhrich C, Schueppel R, Petrich A, Pfeiffer M, Leo K, Brier E, et al. Organic Thin-Film Photovoltaic Cells Based on Oligothiophenes with Reduced Bandgap. Advanced Functional Materials. 2007 Oct;17(15):2991–2999. Available from: http://doi.wiley.com/10.1002/adfm.200600917.

[105] Wilson B. Solar Cells;. (Cited on pages 45 and 49.)

[106] Tsubomura H, Matsumura M, Nomura Y, Amamiya T. Dye sensitised zinc oxide: aqueous electrolyte: platinum photocell. Nature. 1976 Jun;261(5559):402–403. Available from: http://www.nature.com/doifinder/10.1038/261402a0. (Cited on page 50.)

[107] Miettunen K, Halme J, Toivola M, Lund P. Initial Performance of Dye Solar Cells on Stainless Steel Substrates. The Journal of Physical Chemistry C. 2008;112(10):4011–4017. (Cited on pages 51, 52, and 54.)

[108] Cameron P, Peter L. Characterization of Titanium Dioxide Blocking Layers in Dye-Sensitized Nanocrystalline Solar Cells. Journal of Physical Chemistry B. 2003;107:14394–14400. (Cited on pages 51, 52, 53, and 54.)

[109] Chen CY, Wu SJ, Li JY, Wu CG, Chen JG, Ho KC. A New Route to Enhance the Light-Harvesting Capability of Ruthenium Complexes for Dye-Sensitized Solar Cells. Advanced Materials. 2007 Nov;19(22):3888–3891. Available from: http://doi.wiley.com/10.1002/adma.200701111.

[110] Toivola M, Ahlskog F, Lund P. Industrial sheet metals for nanocrystalline dye-sensitized solar cell structures. Solar Energy Materials and Solar Cells. 2006;90(17):2881–2893. Doi: DOI: 10.1016/j.solmat.2006.05.002. (Cited on pages 51 and 54.)

[111] Kakiuchi K, Saito M, Fujihara S. Fabrication of ZnO films consisting of densely accumulated mesoporous nanosheets and their dye-sensitized solar cell performance. Thin Solid Films.

2008;516(8):2026–2030. Doi: DOI: 10.1016/j.tsf.2007.07.136. (Cited on pages 52 and 55.)

[112] Peter L. Dye-sensitized nanocrystalline solar cells. Physical Chemistry Chemical Physics. 2007;9:2630. (Cited on pages 52, 53, and 54.)

[113] Arabatzis IM, Antonaraki S, Stergiopoulos T, Hiskia A, Papaconstantinou E, Bernard MC, et al. Preparation, characterization and photocatalytic activity of nanocrystalline thin film TiO2 catalysts towards 3,5-dichlorophenol degradation. Journal of Photochemistry and Photobiology A: Chemistry. 2002;149(1-3):237–245. Doi: DOI: 10.1016/S1010-6030(01)00645-1. (Cited on page 55.)

[114] Kang MG, Park NG, Ryu KS, Chang SH, Kim KJ. A 4.2% efficient flexible dye-sensitized TiO2 solar cells using stainless steel substrate. Solar Energy Materials and Solar Cells. 2006;90(5):574–581. Doi: DOI: 10.1016/j.solmat.2005.04.025.

[115] Lopez-Luke T, Wolcott A, Xu Lp, Chen S, Wen Z, Li J, et al. Nitrogen-Doped and CdSe Quantum-Dot-Sensitized Nanocrystalline TiO2 Films for Solar Energy Conversion Applications. The Journal of Physical Chemistry C. 2008;112(4):1282–1292.

[116] Yu-Jen S, Yuh-Lang L. Assembly of CdS quantum dots onto mesoscopic TiO2 films for quantum dot-sensitized solar cell applications. Nanotechnology. 2008;(4):045602. (Cited on page 55.)

[117] Hsu YF, Xi YY, Yip CT, Djurisic AB, Chan WK. Dye-sensitized solar cells using ZnO tetrapods. Journal of Applied Physics. 2008;103(8):083114–4. (Cited on page 55.)

[118] Keis K, Bauer C, Boschloo G, Hagfeldt A, Westermark K, Rensmo H, et al. Nanostructured ZnO electrodes for dye-sensitized solar cell applications. Journal of Photochemistry and Photobiology A: Chemistry. 2002;148(1-3):57–64. Doi: DOI: 10.1016/S1010-6030(02)00039-4.

[119] Yoshida T, Terada K, Schlettwein D, Oekermann T, Sugiura T, Minoura H. Electrochemical Self-Assembly of Nanoporous ZnO/Eosin Y Thin Films and Their Sensitized Photoelectrochemical Performance. Advanced Materials. 2000 Aug;12(16):1214–1217. (Cited on page 55.)

[120] Nazeeruddin MK, Kay A, Rodicio I, Humphry-Baker R, Mueller E, Liska P, et al. Conversion of light to electricity by cis-X2bis(2,2'-bipyridyl-4,4'-dicarboxylate)ruthenium(II) charge-transfer sensitizers (X = Cl-, Br-, I-, CN-, and SCN-) on nanocrystalline titanium dioxide electrodes. Journal of the American Chemical Society. 1993;115(14):6382–6390. (Cited on page 55.)

[121] Boudreau LC, Kuck JA, Tsapatsis M. Deposition of oriented zeolite A films in situ and secondary growth. Journal of Membrane Science. 1999;152(1):41–59. Copyright (C) 2011 American Chemical Society (ACS). All Rights Reserved. (Cited on pages 55, 58, and 128.)

[122] Cundy CS, Cox PA. The hydrothermal synthesis of zeolites: Precursors, intermediates and reaction mechanism. Microporous and Mesoporous Materials. 2005 Jul;82(1-2):1–78. Available from: http://linkinghub.elsevier.com/retrieve/pii/S1387181105000934. (Cited on pages 55, 56, and 64.)

[123] Julbe A. Zeolite Membranes - Synthesis, Characterisation and Application. In: Introduction to Zeolite Science and Practice. 3rd ed. Elsevier;. p. 181–219. (Cited on pages 58 and 59.)

[124] Sebastian V, Mallada R, Coronas J, Julbe A, Terpstra RA, Dirrix RW. Microwave-assisted hydrothermal rapid synthesis of capillary MFI-type zeolite–ceramic membranes for pervaporation application. Journal of Membrane Science. 2010 Jun;355(1-2):28–35. Available from: http://linkinghub.elsevier.com/retrieve/pii/S037673881000195X. (Cited on page 55.)

[125] Liu Y, Lew CM, Sun M, Cai R, Wang J, Kloster G, et al. On-Wafer Crystallization of Ultralow-? Pure Silica Zeolite Films. Angewandte Chemie International Edition. 2009;48(26):4777–4780. Available from: http://dx.doi.org/10.1002/anie.200900461. (Cited on pages 58, 128, 129, 135, and 150.)

[126] Liu Y, Sun M, Lew CM, Wang J, Yan Y. MEL-type Pure-Silica Zeolite Nanocrystals Prepared by an Evaporation-Assisted Two-Stage Synthesis Method as Ultra-Low-k Materials. Advanced Functional Materials. 2008 Jun;18(12):1732–1738. Available from: http://doi.wiley.com/10.1002/adfm.200701134. (Cited on page 129.)

[127] Snyder MA, Tsapatsis M. Hierarchical Nanomanufacturing: From Shaped Zeolite Nanoparticles to High-Performance Separation Membranes. Angewandte Chemie-International Edition. 2007;46(40):7560–7573. Available from: http://dx.doi.org/10.1002/chin.200749242. (Cited on pages 58, 128, and 150.)

[128] Tsapatsis M. Toward High-Throughput Zeolite Membranes. Science. 2011 Nov;334(6057):767 –768. Available from: http://www.sciencemag.org/content/334/6057/767.short. (Cited on pages 58 and 128.)

[129] Xu X, Bao Y, Song C, Yang W, Liu J, Lin L. Microwave-assisted hydrothermal synthesis of hydroxy-sodalite zeolite membrane. Microporous and Mesoporous Materials. 2004 Nov;75(3):173–181. Available from: http://linkinghub.elsevier.com/retrieve/pii/S1387181104002896. (Cited on pages 58 and 60.)

[130] Holmes SM, Markert C, Plaisted RJ, Forrest JO, Agger JR, Anderson MW, et al. A Novel Method for the Growth of Silicalite Membranes on Stainless Steel Supports. Chemistry of Materials. 1999 Nov;11(11):3329–3332. Available from: http://pubs.acs.org/doi/abs/10.1021/cm991087u. (Cited on page 58.)

[131] Kusakabe K. Morphology and gas permeance of ZSM-5-type zeolite membrane formed on a porous ?-alumina support tube. Journal of Membrane Science. 1996 Jul;116(1):39–46. Available from: http://linkinghub.elsevier.com/retrieve/pii/0376738896000105. (Cited on page 58.)

[132] Liu Q, Noble R, Falconer JL, Funke H. Organics/water separation by pervaporation with a zeolite membrane. Journal of Membrane Science. 1996 Aug;117(1-2):163–174. Available from: http://linkinghub.elsevier.com/retrieve/pii/0376738896000580.

[133] Morigami Y, Kondo M, Abe J, Kita H, Okamoto K. The first large-scale pervaporation plant using tubular-type module with zeolite NaA membrane. Separation and Purification Technology. 2001 Oct;25(1-3):251–260. Available from: http://linkinghub.elsevier.com/retrieve/pii/S1383586601001095.

[134] Vroon Z, Keizer K, Gilde M, Verweij H, Burggraaf A. Transport properties of alkanes through ceramic thin zeolite MFI membranes. Journal of Membrane Science. 1996 May;113(2):293–300. Available from: http://linkinghub.elsevier.com/retrieve/pii/037673889500128X.

[135] Yan Y, Davis ME, Gavalas GR. Preparation of highly selective zeolite ZSM-5 membranes by a post-synthetic coking treatment. Journal of Membrane Science. 1997 Jan;123(1):95–103. Available from: http://linkinghub.elsevier.com/retrieve/pii/S0376738896002062.

[136] Yuan W, Lin YS, Yang W. Molecular Sieving MFI-Type Zeolite Membranes for Pervaporation Separation of Xylene Isomers. Journal of the American Chemical Society. 2004 Apr;126(15):4776–4777. Available from: http://pubs.acs.org/doi/abs/10.1021/ja031653t. (Cited on page 58.)

[137] Chaikittisilp W, Davis ME, Okubo T. TPA + -Mediated Conversion of Silicon Wafer into Preferentially-Oriented MFI Zeolite Film under Steaming. Chemistry of Materials. 2007 Aug;19(17):4120–4122. Available from: http://pubs.acs.org/doi/abs/10.1021/cm071475t. (Cited on pages 58 and 137.)

[138] Davis ME. Ordered porous materials for emerging applications. Nature. 2002 Jun;417(6891):813–821. Available from: http://dx.doi.org/10.1038/nature00785. (Cited on pages 58 and 127.)

[139] Bein T. Synthesis and Applications of Molecular Sieve Layers and Membranes †. Chemistry of Materials. 1996 Jan;8(8):1636–1653. Available from: http://pubs.acs.org/doi/abs/10.1021/cm960148a. (Cited on pages 60, 128, and 150.)

[140] Caro J, Noack M. Zeolite membranes – Recent developments and progress. Microporous and Mesoporous Materials. 2008 Nov;115(3):215–233. Available from: http://www.sciencedirect.com/science/article/pii/S1387181108001406. (Cited on page 128.)

[141] Choi M, Na K, Kim J, Sakamoto Y, Terasaki O, Ryoo R. Stable single-unit-cell nanosheets of zeolite MFI as active and long-lived catalysts. Nature. 2009;461(7261):246–249. Avail-

able from: http://dx.doi.org/10.1038/nature08288. (Cited on page 128.)

[142] Eslava S, Seo JW, Kirschhock CE, Baklanov MR, Maex K, Martens JA. Comment on "MEL-type Pure-Silica Zeolite Nanocrystals Prepared by an Evaporation-Assisted Two-Stage Synthesis Method as Ultra-Low-k Materials". Advanced Functional Materials. 2010;20(15):2377–2379. Available from: http://dx.doi.org/10.1002/adfm.201000114. (Cited on page 129.)

[143] McLeary E, Jansen J, Kapteijn F. Zeolite based films, membranes and membrane reactors: Progress and prospects. Microporous and Mesoporous Materials. 2006 Mar;90(1–3):198–220. Available from: http://www.sciencedirect.com/science/article/pii/S1387181105005408. (Cited on page 128.)

[144] Sebastian V, Mallada R, Coronas J, Julbe A, Terpstra RA, Dirrix RW. Microwave-assisted hydrothermal rapid synthesis of capillary MFI-type zeolite–ceramic membranes for pervaporation application. Journal of Membrane Science. 2010 Jun;355(1-2):28–35. Available from: http://linkinghub.elsevier.com/retrieve/pii/S037673881000195X.

[145] Tosheva L, Valtchev VP. Nanozeolites: Synthesis, Crystallization Mechanism, and Applications. Chemistry of Materials. 2005;17(10):2494–2513. Copyright (C) 2011 American Chemical Society (ACS). All Rights Reserved. (Cited on page 150.)

[146] Yoo Y, Lai Z, Jeong HK. Fabrication of MOF-5 membranes using microwave-induced rapid seeding and solvothermal secondary growth. Microporous and Mesoporous Materials. 2009 Jul;123(1-3):100–106. Available from: http://linkinghub.elsevier.com/retrieve/pii/S1387181109001668. (Cited on page 60.)

[147] Barrer RM. Zeolites and their synthesis. Zeolites. 1981 Oct;1(3):130–140. Available from: http://linkinghub.elsevier.com/retrieve/pii/S0144244981800012. (Cited on page 64.)

[148] Rabenau A. The Role of Hydrothermal Synthesis in Preparative Chemistry. Angewandte Chemie International Edition in En-

glish. 1985 Dec;24(12):1026–1040. Available from: http://doi.wiley.com/10.1002/anie.198510261. (Cited on page 64.)

[149] Cockcroft JK, Barnes P. Powder Diffraction on the Web;. Available from: http://pd.chem.ucl.ac.uk/pd/welcome.htm. (Cited on pages 64, 65, 66, and 68.)

[150] Qazi SJS, Rennie AR, Cockcroft JK, Vickers M. Use of wide-angle X-ray diffraction to measure shape and size of dispersed colloidal particles. Journal of Colloid and Interface Science. 2009;338(1):105–110. Doi: DOI: 10.1016/j.jcis.2009.06.006. (Cited on pages 64 and 85.)

[151] Le Bail A, Duroy H, Fourquet J. Ab-initio structure determination of LiSbWO6 by X-ray powder diffraction. Materials Research Bulletin. 1988 Mar;23(3):447–452. Available from: http://linkinghub.elsevier.com/retrieve/pii/0025540888900190. (Cited on page 67.)

[152] Rietveld HM. Line profiles of neutron powder-diffraction peaks for structure refinement. Acta Crystallographica. 1967 Jan;22(1):151–152. Available from: http://scripts.iucr.org/cgi-bin/paper?S0365110X67000234. (Cited on page 67.)

[153] Rietveld HM. A profile refinement method for nuclear and magnetic structures. Journal of Applied Crystallography. 1969 Jun;2(2):65–71. Available from: http://scripts.iucr.org/cgi-bin/paper?S0021889869006558. (Cited on page 67.)

[154] Barrett CS, Massalski T. Structure of Metals. McGraw Hill; 1980. p. 204. (Cited on page 69.)

[155] Goldstein J, Newbury DE, Joy DC, Lyman CE, Echlin P, Llfshin E, et al. Scanning Electron Microscopy and X-ray Microanalysis. 3rd ed. Springer;. (Cited on page 70.)

[156] Newville M. Fundamentals of XAFS. University of Chicago; 2004. (Cited on pages 70, 71, 72, 73, and 75.)

[157] Hahner G. Near edge X-ray absorption fine structure spectroscopy as a tool to probe electronic and structural properties of thin organic films and liquids. Chemical Society Reviews. 2006;35(12):1244. Available from: http://xlink.rsc.org/?DOI=b509853j. (Cited on page 71.)

[158] Ravel B, Newville M. ATHENA , ARTEMIS , HEPHAESTUS : data analysis for X-ray absorption spectroscopy using IFEFFIT. Journal of Synchrotron Radiation. 2005 Jun;12(4):537–541. Available from: http://scripts.iucr.org/cgi-bin/paper?S0909049505012719. (Cited on pages 75, 115, and 132.)

[159] Sankar G, Bell RG, Thomas JM, Anderson MW, Wright PA, Rocha J. Determination of the Structure of Distorted TiO6 Units in the Titanosilicate ETS-10 by a Combination of X-ray Absorption Spectroscopy and Computer Modeling. J Phys Chem. 1996;100(2):449–452. Available from: http://dx.doi.org/10.1021/jp952205d. (Cited on pages 71, 138, and 139.)

[160] Fukano T, Motohiro T. Low-temperature growth of highly crystallized transparent conductive fluorine-doped tin oxide films by intermittent spray pyrolysis deposition. Solar Energy Materials and Solar Cells. 2004;82(4):567–575. Doi: DOI: 10.1016/j.solmat.2003.12.009. (Cited on page 79.)

[161] Palgrave R, Parkin I. Aerosol Assisted Chemical Vapor Deposition Using Nanoparticle Precursors: A Route to Nanocomposite Thin Films. Journal of the American Chemical Society. 2006;128:1587–1597. (Cited on pages 79 and 112.)

[162] Larson A, Von Dreele R. General Structure Analysis System (GSAS); 2000. (Cited on pages 85 and 114.)

[163] Toby BH. EXPGUI, a graphical user interface for GSAS. Journal of Applied Crystallography. 2001 Apr;34(2):210–213. Available from: http://scripts.iucr.org/cgi-bin/paper?S0021889801002242. (Cited on pages 85 and 114.)

[164] Subba Ramaiah K, Sundara Raja V. Structural and electrical properties of fluorine doped tin oxide films prepared by spray-pyrolysis technique. Applied Surface Science. 2006;253(3):1451–1458. Doi: DOI: 10.1016/j.apsusc.2006.02.019. (Cited on page 91.)

[165] Athwal IS, Bedi RK. Optical transmission of fluorine-doped tin oxide films. Solid-State Electronics. 1985;28(11):1165–1165. Doi: DOI: 10.1016/0038-1101(85)90197-2. (Cited on page 96.)

[166] Lee JH, Ko KH, Park BO. Electrical and optical properties of ZnO transparent conducting films by the sol–gel method.

Journal of Crystal Growth. 2003 Jan;247(1-2):119–125. Available from: http://linkinghub.elsevier.com/retrieve/pii/S0022024802019073. (Cited on page 110.)

[167] King PDC, Veal TD. Conductivity in transparent oxide semiconductors. Journal of Physics: Condensed Matter. 2011 Aug;23(33):334214. Available from: http://stacks.iop.org/0953-8984/23/i=33/a=334214?key=crossref.6b3e919e4c893ee67cfe47de718dd5f3. (Cited on page 110.)

[168] Godinho KG, Walsh A, Watson GW. Energetic and Electronic Structure Analysis of Intrinsic Defects in SnO 2. The Journal of Physical Chemistry C. 2009 Jan;113(1):439–448. Available from: http://pubs.acs.org/doi/abs/10.1021/jp807753t. (Cited on page 110.)

[169] Sato H, Minami T, Takata S, Yamada T. Transparent conducting p-type NiO thin films prepared by magnetron sputtering. Thin Solid Films. 1993 Dec;236(1-2):27–31. Available from: http://linkinghub.elsevier.com/retrieve/pii/0040609093906364. (Cited on page 111.)

[170] Moholkar AV, Pawar SM, Rajpure KY, Bhosale CH. Effect of concentration of SnCl4 on sprayed fluorine doped tin oxide thin films. Journal of Alloys and Compounds. 2008;455(1-2):440–446. Doi: DOI: 10.1016/j.jallcom.2007.01.160. (Cited on page 111.)

[171] Moholkar AV, Pawar SM, Rajpure KY, Bhosale CH, Kim JH. Effect of fluorine doping on highly transparent conductive spray deposited nanocrystalline tin oxide thin films. Applied Surface Science. 2009;255(23):9358–9364. Doi: DOI: 10.1016/j.apsusc.2009.07.035. (Cited on page 111.)

[172] Ghandhi SK, Field RJ, Shealy JR. Highly oriented zinc oxide films grown by the oxidation of diethylzinc. Applied Physics Letters. 1980;37(5):449. Available from: http://link.aip.org/link/APPLAB/v37/i5/p449/s1&Agg=doi. (Cited on page 112.)

[173] Hollingsworth N, Johnson AL, Kingsley A, Kociok-Ko?hn G, Molloy KC. Structural Study of the Reaction of Methylzinc Amino Alcoholates with Oxygen. Organometallics. 2010

Aug;29(15):3318–3326. Available from: http://pubs.acs.org/doi/abs/10.1021/om100449t. (Cited on page 115.)

[174] McNally CS, Turner DP, Kulak AN, Meldrum FC, Hyett G. The use of cationic surfactants to control the structure of zinc oxide films prepared by chemical vapour deposition. Chemical Communications. 2012;48(10):1490. Available from: http://xlink.rsc.org/?DOI=c2cc14468a. (Cited on pages 112 and 151.)

[175] Van de Walle CG. Hydrogen as a Cause of Doping in Zinc Oxide. Physical Review Letters. 2000 Jul;85(5):1012–1015. Available from: http://link.aps.org/doi/10.1103/PhysRevLett.85.1012. (Cited on page 112.)

[176] Oda S, Tokunaga H, Kitajima N, Hanna Ji, Shimizu I, Kokado H. Highly Oriented ZnO Films Prepared by MOCVD from Diethylzinc and Alcohols. Japanese Journal of Applied Physics. 1985 Dec;24(Part 1, No. 12):1607–1610. Available from: http://jjap.jsap.jp/link?JJAP/24/1607/. (Cited on page 112.)

[177] Dessy RE, Coe GR. The Structure of Organozinc Reagents. J Org Chem. 1963;28(12):3592–3593. Available from: http://dx.doi.org/10.1021/jo01047a529. (Cited on page 115.)

[178] Fujimura N, Nishihara T, Goto S, Xu J, Ito T. Control of preferred orientation for ZnOx films: control of self-texture. Journal of Crystal Growth. 1993 May;130(1-2):269–279. Available from: http://linkinghub.elsevier.com/retrieve/pii/002202489390861P. (Cited on page 116.)

[179] Sanchez-Juarez A. Properties of fluorine-doped ZnO deposited onto glass by spray pyrolysis. Solar Energy Materials and Solar Cells. 1998 Apr;52(3-4):301–311. Available from: http://linkinghub.elsevier.com/retrieve/pii/S0927024897002468. (Cited on page 117.)

[180] Liew LL, Sankar G, Handoko AD, Goh GK, Kohara S. Understanding the defect structure of solution grown zinc oxide. Journal of Solid State Chemistry. 2012 May;189:63–67. Available from: http://linkinghub.elsevier.com/retrieve/pii/S0022459612000254. (Cited on page 120.)

[181] Corma A. State of the art and future challenges of zeolites as catalysts. Journal of Catalysis. 2003 May;216(1–2):298–312. Available from: http://www.sciencedirect.com/science/article/pii/S002195170200132X. (Cited on page 127.)

[182] Lew CM, Cai R, Yan Y. Zeolite Thin Films: From Computer Chips to Space Stations. Acc Chem Res. 2010;43(2):210–219. Available from: http://dx.doi.org/10.1021/ar900146w. (Cited on page 128.)

[183] Pina M, Mallada R, Arruebo M, Urbiztondo M, Navascués N, de la Iglesia O, et al. Zeolite films and membranes. Emerging applications. Microporous and Mesoporous Materials. 2011 Oct;144(1–3):19–27. Available from: http://www.sciencedirect.com/science/article/pii/S1387181110004361. (Cited on page 128.)

[184] Valtchev V, Mintova S. Layer-by-layer preparation of zeolite coatings of nanosized crystals. Microporous and Mesoporous Materials. 2001 Mar;43(1):41–49. Available from: http://linkinghub.elsevier.com/retrieve/pii/S1387181100003450. (Cited on pages 128 and 150.)

[185] Pham TCT, Kim HS, Yoon KB. Growth of Uniformly Oriented Silica MFI and BEA Zeolite Films on Substrates. Science. 2011 Dec;334(6062):1533 –1538. Available from: http://www.sciencemag.org/content/334/6062/1533.abstract. (Cited on page 128.)

[186] Gurman SJ, Binsted N, Ross I. A rapid, exact, curved-wave theory for EXAFS calculations. II. The multiple-scattering contributions. Journal of Physics C: Solid State Physics. 1986 Apr;19(11):1845–1861. Available from: http://stacks.iop.org/0022-3719/19/i=11/a=021?key=crossref.61df7623771b0d76bad21793c96c350f. (Cited on page 132.)

[187] Johnson BF, Klunduk MC, Martin CM, Sankar G, Teate SJ, Meurig Thomas J. The preparation, molecular structure and catalytic relevance of Ti(OSiPh3)4 and Ti(OGePh3)4. Journal of Organometallic Chemistry. 2000 Feb;596(1–2):221–225. Available from: http://www.sciencedirect.com/science/article/pii/S0022328X99007445. (Cited on page 138.)

[188] Sankar G, Thomas JM, Catlow CRA, Barker CM, Gleeson D, Kaltsoyannis N. The Three-Dimensional Structure of the Titanium-Centered Active Site during Steady-State Catalytic Epoxidation of Alkenes. J Phys Chem B. 2001;105(38):9028–9030. Available from: http://dx.doi.org/10.1021/jp011979t. (Cited on pages 138 and 139.)

[189] Wong J, Messmer RP, Maylotte DH. K-edge absorption spectra of selected vanadium compounds. Physical Review B. 1984 Nov;30(10):5596–5610. Available from: http://link.aps.org/doi/10.1103/PhysRevB.30.5596. (Cited on page 141.)

[190] Hafizovic J, Bjørgen M, Olsbye U, Dietzel PDC, Bordiga S, Prestipino C, et al. The Inconsistency in Adsorption Properties and Powder XRD Data of MOF-5 Is Rationalized by Framework Interpenetration and the Presence of Organic and Inorganic Species in the Nanocavities. Journal of the American Chemical Society. 2007 Mar;129(12):3612–3620. Available from: http://pubs.acs.org/doi/abs/10.1021/ja0675447. (Cited on pages 142 and 155.)

[191] Zenonos C, Sankar G, Cora F, Lewis DW, Pankhurst QA, Catlow CRA, et al. On the nature of iron species in iron substituted aluminophosphates. Physical Chemistry Chemical Physics. 2002 Oct;4(21):5421–5429. (Cited on page 143.)

[192] Wilke M, Farges F, Petit PE, Brown GE, Martin F. Oxidation state and coordination of Fe in minerals: An Fe K-XANES spectroscopic study. American Mineralogist. Jun.;86(5-6):714 –730. Available from: http://ammin.geoscienceworld.org/content/86/5-6/714.abstract. (Cited on page 144.)

[193] Yaghi OM, O'Keeffe M, Ockwig NW, Chae HK, Eddaoudi M, Kim J. Reticular synthesis and the design of new materials. Nature. 2003 Jun;423(6941):705–714. Available from: http://www.nature.com/doifinder/10.1038/nature01650. (Cited on pages 149 and 150.)

[194] Shekhah O, Liu J, Fischer RA, Wöll C. MOF thin films: existing and future applications. Chemical Society Reviews. 2011;40(2):1081. Available from: http://xlink.rsc.org/?DOI=c0cs00147c. (Cited on page 150.)

[195] Rowsell JL, Yaghi OM. Metal–organic frameworks: a new class of porous materials. Microporous and Mesoporous Materials. 2004 Aug;73(1-2):3–14. Available from: http://linkinghub.elsevier.com/retrieve/pii/S1387181104001295. (Cited on page 150.)

[196] Feng PL, Perry IV JJ, Nikodemski S, Jacobs BW, Meek ST, Allendorf MD. Assessing the Purity of Metal-Organic Frameworks Using Photoluminescence: MOF-5, ZnO Quantum Dots, and Framework Decomposition. Journal of the American Chemical Society. 2010 Nov;132(44):15487–15489. Available from: http://pubs.acs.org/doi/abs/10.1021/ja1065625. (Cited on page 150.)

[197] Horcajada P, Serre C, Maurin G, Ramsahye NA, Balas F, Vallet-Regí M, et al. Flexible Porous Metal-Organic Frameworks for a Controlled Drug Delivery. Journal of the American Chemical Society. 2008 May;130(21):6774–6780. Available from: http://pubs.acs.org/doi/abs/10.1021/ja710973k. (Cited on page 150.)

[198] Serre C, Millange F, Surble S, Ferey G. A Route to the Synthesis of Trivalent Transition-Metal Porous Carboxylates with Trimeric Secondary Building Units. Angewandte Chemie. 2004;116(46):6445–6449. (Cited on page 150.)

[199] Zacher D, Shekhah O, Wöll C, Fischer RA. Thin films of metal–organic frameworks. Chemical Society Reviews. 2009;38(5):1418. Available from: http://xlink.rsc.org/?DOI=b805038b. (Cited on page 150.)

[200] Stephan Hermes, Denise Zacher, Arne Baunemann, Christof Woll, Roland A Fischer. Selective Growth and MOCVD Loading of Small Single Crystals of MOF-5 at Alumina and Silica Surfaces Modified with Organic Self-Assembled Monolayers. Chemistry of Materials. 2007;19(9):2168–2173. (Cited on page 151.)

[201] Hughes JT, Navrotsky A. MOF-5: Enthalpy of Formation and Energy Landscape of Porous Materials. Journal of the American Chemical Society. 2011 Jun;133(24):9184–9187. Available from: http://pubs.acs.org/doi/abs/10.1021/ja202132h. (Cited on page 151.)

[202] Biemmi E, Christian S, Stock N, Bein T. High-throughput screening of synthesis parameters in the formation of the metal-organic frameworks MOF-5 and HKUST-1. Microporous and Mesoporous Materials. 2009 Jan;117(1-2):111–117. Available from: http://linkinghub.elsevier.com/retrieve/pii/S138718110800303X. (Cited on page 155.)